

博士論文
(Doctoral Thesis)

Study on Optical Yagi-Uda Antennas
Utilizing Localized Surface Plasmon
Resonance of Metal Nanoparticles

〔金属ナノ粒子の局在表面プラズモン共鳴
を用いた光八木宇田アンテナの研究〕

小迫 照和
(Terukazu Kosako)

広島大学大学院先端物質科学研究科

〔Graduate School of Advanced Sciences of Matter
Hiroshima University〕

2016年2月
(February 2016)

目 次

(Table of Contents)

1. 主論文 (Main Thesis)

Study on Optical Yagi-Uda Antennas Utilizing

Localized Surface Plasmon Resonance of Metal Nanoparticles

(金属ナノ粒子の局在表面プラズモン共鳴を用いた光八木宇田アンテナの研究)

Terukazu Kosako (小迫 照和)

2. 公表論文 (Published papers)

(1) Design parameters for a nano-optical Yagi-Uda antenna.

Holger F Hofmann, Terukazu Kosako and Yutaka Kadoya.

New Journal of Physics, **9**, **217**, 1-12 (2007).

(2) Directional control of light by a nano-optical Yagi-Uda antenna.

Terukazu Kosako, Yutaka Kadoya and Holger F. Hofmann.

Nature Photonics, **4**, 312-315 (2010).

主 論 文
(Main Thesis)

Acknowledgments

I performed this work when I was in the doctor's course at the Graduate School of Advanced Sciences of Matter, Hiroshima University, Japan.

I am extremely grateful to Professor Yutaka Kadoya for providing me an opportunity to study as a doctor course student and for giving me fruitful guidance and timely encouragement to complete this research. I am sincerely grateful to Associate professor Holger F. Hofmann as well for giving me strong support in my investigation of theoretical models and the analysis of the experimental results. I am also deeply grateful to Assistant professor Jiro Kitagawa (currently Associate professor at Fukuoka Institute of Technology, Japan) for giving me kind pieces of advice and helping me to maintain the experimental equipments. I am also deeply grateful to Mr. Hiroshi Taniguchi (A technical staff in HU Technical Center at the time of this research) for helping me to develop the measurement set up.

I was not able to accomplish this work without numerous kinds of support from professors and researchers mentioned above.

I was financially supported by the USHIO Foundation during my master's course. The scholarship enabled me to make my endeavors to study at the doctor's course. I am sincerely grateful to Professor Takayuki Takahagi for recommending me to apply the scholarship.

Finally, I would like to express my gratitude to my family for their strong support.

Table of contents

1. INTRODUCTION	1
1.1. BACKGROUND: NANO-OPTICS AND PLASMONICS	1
1. 1. 1. Propagating surface plasmon	3
1. 1. 2. Localized surface plasmon (LSP)	5
1.2. OPTICAL ANTENNAS	9
1.3. PURPOSE OF THIS WORK	11
1.4. STRUCTURE OF THIS THESIS	13
2. LOCALIZED SURFACE PLASMON RESONANCE IN METAL NANOPARTICLES	14
2.1. OPTICAL RESPONSE OF A SINGLE NANOPARTICLE	14
2.1.1. Mie theory	14
2.1.2. Quasi static approximation	16
2.1.3. Ellipsoidal metal particle	18
2.1.4. Expression for the response of a point dipole including radiation damping	20
2.2. COUPLED DIPOLE MODEL FOR ONE-DIMENSIONAL NANOPARTICLE ARRAYS ..	24
2.3. DIELECTRIC CONSTANT OF GOLD	26
3. RESONANCE IN NANOPARTICLE ARRAY	27
3.1. DIPOLE MODEL PREDICTION	27
3.2. EXPERIMENTAL RESULTS	30
4. DESIGN OF NANO OPTICAL YAGI-UDA ANTENNA	33
4.1. BASICS OF YAGI-UDA ANTENNA DESIGN	33
4.1.1. Yagi-Uda antenna in radio frequency region	33
4.1.2. Optical Yagi-Uda antenna	35
4.2. DESIGN OF OPTICAL YAGI-UDA ANTENNA	38
4.2.1. Coupled dipole model	38
4.2.2. Two-element antenna	40
4.2.3. Three-element antenna	44
4.2.4. Five-element antenna	47
4.2.5. Effect of material losses on the directivity	51
4.3. SUMMARY	53

5. NANO-OPTICAL YAGI-UDA ANTENNA: EXPERIMENT	55
5.1. NANO PATTERN FABRICATION	55
5.2. DRIVING METHOD OF ANTENNA	57
5.3. MEASUREMENT SET-UP.....	59
5.3.1. Evaluation of resonant wavelength.....	59
5.3.2. Measurement of radiation pattern.....	59
5.4. DEMONSTRATION OF OPTICAL YAGI-UDA ANTENNA	62
5.4.1. Antenna design & layout	62
5.4.2. Resonant wavelength of each element	63
5.4.3. Directionality	66
5.4.4. Discussions	71
5.5. WORKING WAVELENGTH DEPENDENCE.....	77
5.5.1. Antenna design & layout	77
5.5.2. Resonant wavelength of each element	78
5.5.3. Directionality	81
5.6. SUMMARY	84
6. CONCLUSION	86
REFERENCES	89
APPENDIX I MATHEMATICA PROGRAM CODES	96
APPENDIX II BI-LAYER RESIST PROCESS AND LIFT-OFF PROCESS.....	105
APPENDIX III SAMPLE LAYOUT	106

1. Introduction

1.1. Background: nano-optics and plasmonics

Since 2000s, nano-optics (or nanophotonics) has become an active research area for understanding and applying optical phenomena on the scale near or beyond the diffraction limit of light [1-3]. Nano-optics is encouraged by the rapid progress of nanoscience and nanotechnology in the past a few decades, as well as motivated by the need for new technology in the field of nanofabrication, information devices, microscopy, and sensors. The plasmon, induced by coupling optical field with free electrons in metallic structures, is widely utilized for realizing the required functions. The significance of plasmonics can be recognized through outlining the historical development of nano-optics and the contribution of plasmonics in that field.

Since the invention of optical microscopes in 17th century [1, 4], scientists had advanced the spatial resolution. The optical theories developed in the 18th and 19th centuries had encouraged the advancement. However, it was eventually recognized that the diffraction limit of light restricts the resolution [5, 6]. In order to overcome the limitation, for instance, far-field radiation is modified in the confocal microscopy [7, 8] that has become one of the indispensable tools to observe the luminescent markers tagged to molecules in the field of biotechnology.

On the other hand, as other schemes, Synge first proposed a type of the near-field optics in 1928 [9, 10]. Figure 1.1 shows his concept that uses a tiny particle as a light source (probe), and raster-scans the sample in close distance from the particle. Thus the spatial resolution does not depend on the wavelength of light but on the size of the probe. Today, his idea is well verified in the development of SNOM/NSOM (scanning near-field optical microscopy) [10-17]. The development is based on the techniques to fabricate sub wavelength-sized probe, as well as on the invention of scanning tunneling microscopy in 1982 [18] that enables the distance to be regulated between the probe and the sample with high accuracy. In order to ensure the effective coupling between the probe and the sample surface, plasmonics is introduced. Success in the near-field optical microscopy makes it possible for the plasmonics to be one of the core technologies in the field of nano-optics.

Figure 1.2 describes the two fundamental modes of plasmon. They are roughly classified by the propagation characteristics; propagating surface plasmon polariton (SPP) which occurs at the metal dielectric interface, and localized surface plasmon (LSP) excited in metal nanostructure (e.g. nanoparticle). In the case of SPP, because of

the ohmic losses in the metal, the propagation length, at which the field decays to $1/e$, is limited to several tens of micrometers in optical regime. In the dielectric (air) side, the optical field decays on the scale comparable to the wavelength of light. On the other hand, the optical field of LSP in metal nanoparticle is confined in the vicinity of metal surface in the range comparable to the particle size. Thus with the particle of the size smaller than the wavelength of light, the optical field can be confined in the region much smaller than the diffraction limit. The fundamental physics of SPP and LSP have widely been investigated, and a wide range of applications has been demonstrated in the last decades. In the following, some applications of SPPs and LSPs are reviewed.

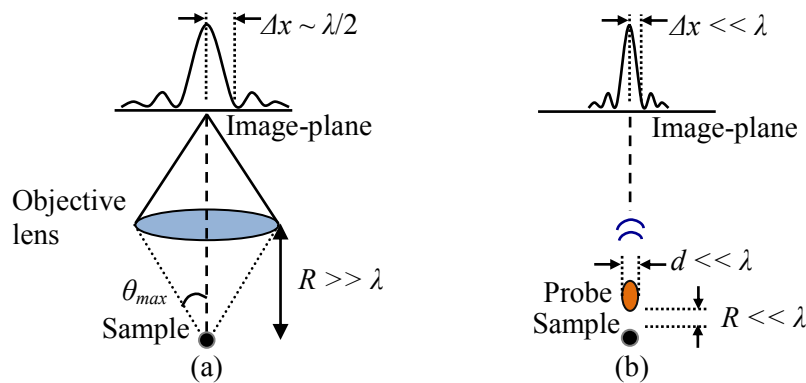


Fig. 1.1: Comparison of (a) conventional and (b) near-field optical microscopy [10]. (a) The diffraction limits the resolution Δx to be about a half wavelength of light. Objective lens is positioned in the far field. (b) The probe size d decides the resolution. The probe is positioned in the near field of the sample.

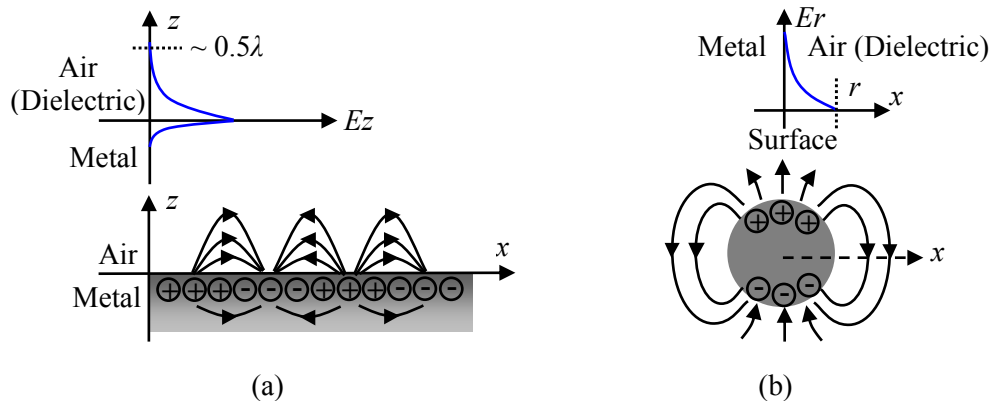


Fig. 1.2: Schematic view of electromagnetic distributions of two fundamental plasmon modes. (a) Surface plasmon polariton (SPP) at the dielectric (air) metal interface. The electric field in the dielectric (air) is confined in the range comparable to the wavelength λ of light. (b) Localized surface plasmon (LSP) in a metallic sphere. The electric field is confined in the range comparable to the radius r of the metallic sphere [1, 2].

1. 1. 1. Propagating surface plasmon

The SPPs was at first recognized in the study of electron energy loss spectroscopy of a thin metallic film. Apart from the bulk plasmon (longitudinal electron oscillations within the bulk), Ritchie theoretically predicted an additional loss induced on the metallic surface in 1957 [19]. Subsequently, Powell and Swan performed a substantive experiment with magnesium and aluminum in 1960 [20].

Figure 1.3 shows the dispersion of SPPs and the light lines. Excitation of SPPs (blue solid line) is possible only if the wavenumber of light increases beyond the limit (light line) in free-space. Therefore, phase-matching procedure is necessary to excite SPPs. The methods that utilize an attenuated total internal reflection were independently proposed by Otto [21] and Kretschmann [22] in 1968. Figure 1.4 illustrates their configuration. Because of its simple procedure, Kretschmann's configuration is commonly used. In the configuration, thin metal film is deposited on the prism surface. The evanescent wave, shown as red-solid line in Fig.1.3 (a), is induced by the incident light at the metal/prism interface. Since its dispersion lies between the (air) light line and the prism light line, the evanescent wave can excite the SPPs at the metal/air interface. Note that the metal film should be thin enough for the evanescent wave to be able to reach the metal-air interface. The theoretical model predicts that thin metal film of a few ten nanometers is enough to obtain SPPs [1]. It is also known that the field confinement normal to the surface becomes weaker for longer propagating length. This trade-off should be considered in the waveguide application. It should be mentioned that Takahara et al. [23] proposed a further confinement of the light field of SPP by one-dimensional optical waveguides.

Otto and Kretschmann's studies led to the development of an important application of SPP. The high sensitivity of SPP excitation condition to the variation of surrounding medium is applicable for sensors [24]. The variation is observed as the shift of resonant spectrum of SPPs. In 1980s, for instance, gas sensing [25] and bio-sensing applications [26] were demonstrated. Optical fiber based SPP sensors were also proposed to meet the need for compact device and remote sensing in the field-use [27, 28].

In the bio-sensing (chemical) applications, the surface of metal film is usually functionalized to react with the material that cannot bind directly to the bare metallic surface. Figure 1.5 shows the functionalization by self-assembled monolayer (SAM) film [29-35]. Since the thickness of SAM layer is typically a few nanometers, detection of the local dielectric change on nanoscale is promising. For example, in-situ measurement of protein binding was demonstrated [29, 30]. The other applications

include biotechnology [32], medical diagnostics [34], food safety [35], etc.

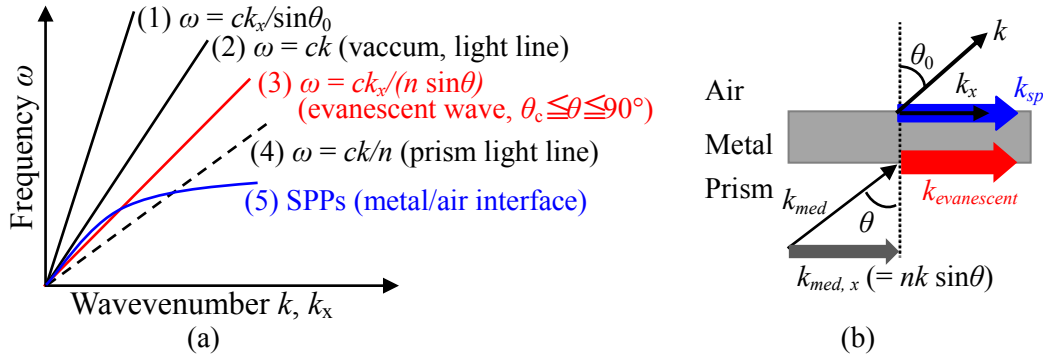


Fig. 1.3: (a) The dispersion relation of SPP and light lines for the case of three-layer system (air/metal/prism) [21, 22]. Light line is described by frequency ω , vaccum light speed c , and wavenumber k as $\omega = ck$. (1) light propagating in air, (2) light line, (3) evanescent wave at metal/prism interface, (4) light line in prism (refractive index $n > 1$), and (5) SPP at the metal/air interface. (b) Configuration considered for (a).

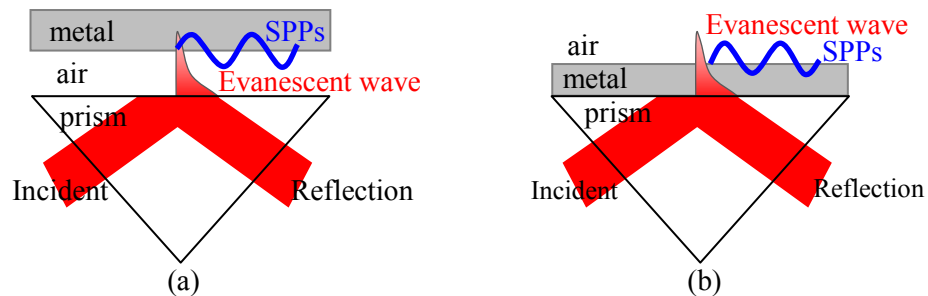


Fig. 1.4: Excitation of SPPs. (a) Otto configuration [21]. The metal and the prism is minutely separated. SPPs is excited at the metal/air interface by the evanescent wave occurred at air/prism interface. (b) Kretschmann's configuration [22]. Thin metal film is deposited on the prism surface. The evanescent wave generates the SPPs at the metal/air interface.

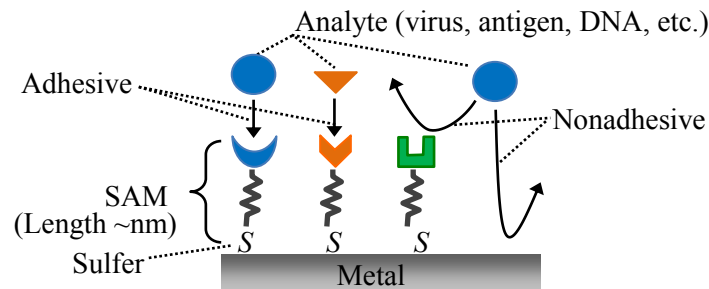


Fig. 1.5: Self-assembled monolayer (SAM) enables SPP or LSPR based sensors to detect the chemical reaction. Analytes bind only to a SAM having adhesive terminal.

1. 1. 2. Localized surface plasmon (LSP)

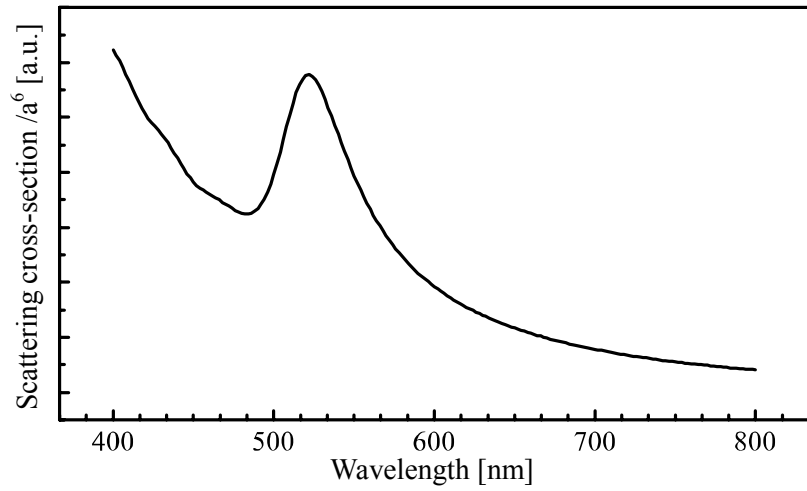
The excitation of LSP needs no phase-matching technique that is necessary for the case of SPPs. Incident light to a metallic nanoparticle generates a collective oscillation of free electrons in the nanoparticle, namely the excitation of LSP. In 1908, G. Mie established an exact solution, so-called “Mie theory”, describing the scattering and the absorption of light by a sphere [36]. This response can be approximated by an oscillating dipole, which is called quasi-static approximation [37], provided that the particle size is sufficiently smaller than the wavelength. With this approximation, the electromagnetic field at a distance r from the dipole is described by the linear equation of the terms $1/r^3$, $1/r^2$, and $1/r$ [4]. The term of $1/r^3$ corresponds to the optical near field.

The LSP induces resonant enhancement of the optical near field, called localized surface plasmon resonance (LSPR), provided that the frequency dependent dielectric constant of a metal $\varepsilon_{metal}(\omega)$ and the surrounding medium ε_{med} satisfy the relation $\text{Re}[\varepsilon_{metal}(\omega_{res})] = -2\varepsilon_{med}$. Here, ω_{res} is the resonant angular frequency. The resonant condition is $\omega_{res} = \omega_p/\sqrt{3}$ [37] for a nanoparticle of Drude metal of (bulk) plasma frequency ω_p located in air. Since the plasma frequencies of noble metals are around the optical frequency region [38], nano-sized metals exhibit different colors from those of the bulk. Surprisingly, this phenomenon had already been used in ancient times for staining glass. Here, for example, consider the glass staining by gold nanoparticles. Figure 1.6 plots the calculation results based on a quasi-static dipole model, described in chapter 2, for scattering and absorption cross-sections of a spherical gold particle in vacuum ($\varepsilon_{med} = 1$). The maximum scattering and absorption exists around 530 nm. Note that the LSPR wavelength does not depend on the radius of the sphere within the dipole approximation. The absorption spectrum indicates that the transmission of white light is red-colored, meanwhile the scattering spectrum shows that the reflection will be greenish. The ancient Roman Lycurgus cup (4th century A.D.) [39-41] containing gold nanoparticles is a well-known example that the transmitted light exhibits red color, meanwhile the reflected light shows green color.

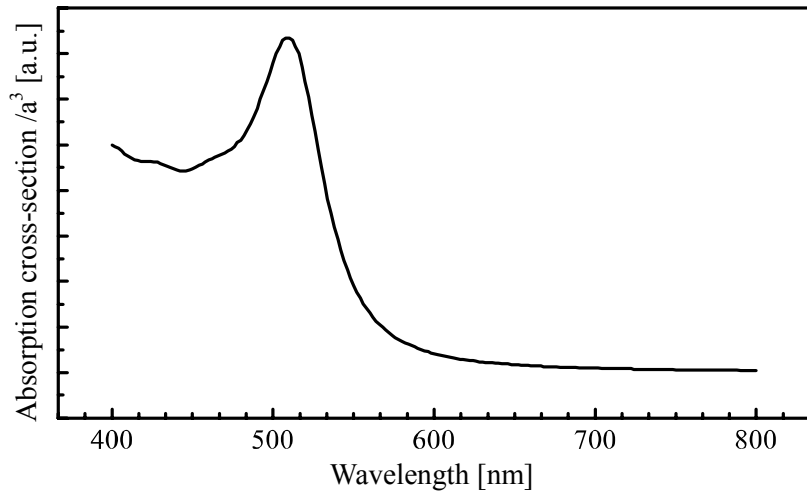
On the other hand, since nanoparticle size is small enough, its shape affects the restoring force to the electrons, which decide the resonance condition of LSPR. Indeed, the larger aspect ratio (= major/minor axis) of nanoparticle weakens the restoring force, which results in the lower frequency of the resonant condition [37].

Internal configuration of a nanoparticle also modifies the LSPR. For example, a core/shell nanoparticle, a dielectric nanoparticle coated with a thin metal layer, was proposed. The arbitrary control of the LSPR is realized by adjusting the ratio of shell

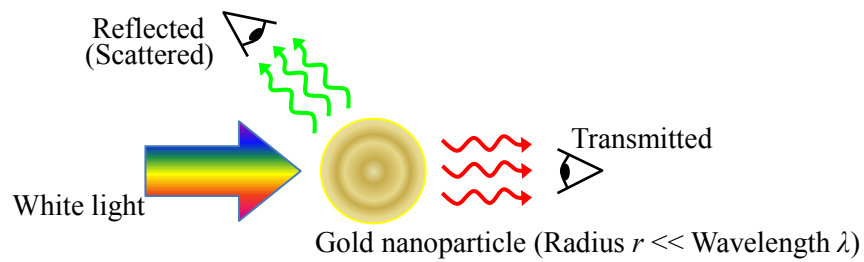
thickness to the particle radius [3, 37].



(a)



(b)



(c)

Fig. 1.6: Rendering a color with gold nanoparticle. The cross-sections of (a) scattering and (b) absorption of a spherical gold particle in vacuum ($\epsilon_{med} = 1$) are plotted as functions of wavelength. Here, a is the radius of the sphere and ϵ_{metal} of gold particle is given by a literature [38]. (c) Observed colors depending on the viewing angle for a white-light illumination. Transmitted light looks red, whereas reflected (scattered) light is greenish.

The significance of LSP in the field of nano-optics was recognized by the discovery of surface-enhanced Raman scattering (SERS) observed on a roughened metal surface in 1974 [42, 43]. Since Raman scattering [44] is an extremely weak effect, its cross-section is typically 14-15 orders of magnitude smaller than that of the fluorescence of dye molecules. However, the scattering as efficient as fluorescence was reported under the condition that the molecules are located in enhanced electric fields of LSP of a pair of metal particles, called hot-spots [45-47].

In a similar way, an acute metal probe positioned in the vicinity of the metal surface can enhance the Raman scattering. This procedure is called tip-enhanced Raman scattering (TERS) [14, 48-52]. Since only the near-field of the probe radiates the TERS signals, imaging of TERS distribution is possible by raster-scanning of the probe.

Similar to the case of SPPs, LSP can be applied to the sensors. Since the resonance condition of LSPR changes if the surrounding medium varies, the nanoparticles of noble metals exhibiting LSPR in optical regime are proposed for sensing application [31-33, 53-59]. The LSPR-based sensor detects the surrounding medium only in the region of confined field that is comparable to the size of nanoparticle. Using the functionalization of the particle surface with a SAM layer, described in Fig. 1.5, the detection of chemical bindings is enabled [31-33, 57].

On the other hand, the LSP of metal nanoparticles enables the fluorescence enhancement by a factor of 10-1000 with respect to the measurement without metallic structures [33]. In the field of medical diagnostics and biotechnology, for example, such an enhancement is important since it enables an efficient detection of single molecule [58], DNA hybridization [59], immunostaining [54], etc.

Since phase-matching technique is not necessary for exciting LSPR, just putting nanoparticles at an end face of optical fiber can construct an optical sensor [60-62]. Such sensors have potential use in in-situ observation. For example, K. Mitsui et al. [62] demonstrated an in-situ affinity measurement with high resolution of adsorption amount 10^{-12} g/mm².

The other application of LSPR is an efficient solar-cells [63-66]. The Si-based solar cells have a trade-off relation between the absorption layer thickness and the energy conversion efficiency. The efficiency of thin-film cells is low compared to that of the wafer-based cells. The electromagnetic enhancement effect of LSPR has been proposed as one of the solutions to enhance the efficiency.

As described above, adjusting its shape, size, and surrounding medium can modify the LSPR of a single metal nanoparticle. On the other hand, for the case of aggregated nanoparticles, such modification also occurs by the mutual electromagnetic interactions

between the particles [67-72]. Figure 1.7 shows the schematic view of the interactions for the two different cases of polarizations. The oscillating electrons in each particle are either weakened or enhanced by the charge distribution of neighboring particles, which will shift the spectral position of the plasmon resonance from that of the isolated particle. The modulation will affect the operation of LSPR-based sensors, since they observe the spectral shift of the LSPR. They usually consist of many particles to enhance the detection signal. In this regard, the more sensitive detection than in the case of random placement is promising by an adequate placement of nanoparticles for obtaining desired spectral position and strength of the LSPR [69-72].

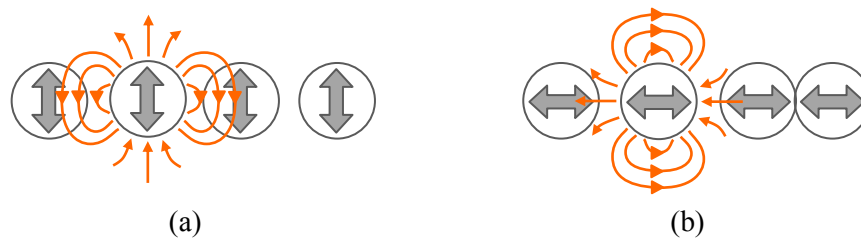


Fig. 1.7: Schematic view of near-field electromagnetic coupling between neighboring particles for the case of the polarization (a) perpendicular and (b) parallel to the array [3].

Inter-particle coupling is also utilized for an optical waveguide with the dimensions below the diffraction limit of light [73-77]. In the case of linear array of nanoparticle, the electromagnetic field is confined in almost one-dimension, and the propagation length is estimated to be longer than micrometer distance [77]. Other applications include random laser [78, 79], sub-wavelength imaging [80-82], and integrated optics [76, 83-85].

Recently, nanoparticles were proposed to be used as the elements to realize artificial material called metamaterial that does not exist in nature. For example, in 2000, Pendry proposed an application for negative-index materials, which can be used for perfect lens of which the imaging resolution is not restricted by the wavelength [86-90]. Metamaterials utilize resonantly excited structures composed of the elements of which the size is smaller than the operating wavelength. For example, a negative index about -0.3 was demonstrated at the wavelength of $1.5 \mu\text{m}$ by an array of metallic nanorods (width, 220 nm; length, 780 nm) [91].

1.2. Optical antennas

During the early years of the invention of near-field optical microscopy, the unique perspective was recognized that there are similarities between the near-field probe and radio frequency (RF) antennas designed to efficiently couple the far field radiation to the feed element [10, 11, 92, 93]. Therefore, the antenna design concepts have been tried to apply to the realization of a device that efficiently converts free-propagating optical radiation to nanoscale emitter, and vice versa [94]. This conceptual antenna is generally called “optical antenna”. Figure 1.8 illustrates the possible applications.

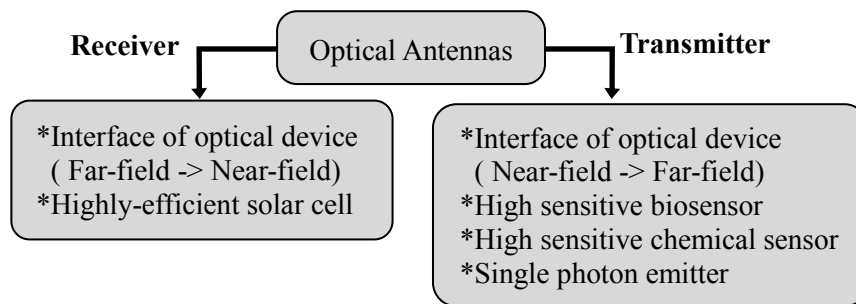


Fig. 1.8: Possible applications of optical antenna.

For instance, half wavelength antenna [95, 96] and bow-tie antenna [97-101] have been demonstrated in optical frequency regime. Grober, et al. [97] suggested that bow-tie antenna could be applied to a near-field optical probe with spatial resolution well below the diffraction limit of light. Schuck, et al. [100] showed the field enhancement $>10^3$ by bow-tie antenna at the wavelength of 830 nm. As more practical application, Farahani, et al. [101] fabricated a bow-tie antenna at the apex of atomic force microscopy tip, and demonstrated the enhancement of photoluminescence of a single quantum dot at the excitation wavelength of 532 nm. On the other hand, Mühlischlegel, et al. [95] demonstrated the strong field enhancement by a half-wave length type antenna with the full element length of 255 nm at the input wavelength of 830 nm. The element length was evidently shorter than one-half of the working wavelength of the antenna, which contradicted the standard design of RF antenna.

The so-called “Bull’s eye antenna”, which consists of grating structure with tiny aperture, was demonstrated to enhance the optical near field. At the wavelength of 840 nm, Ishi, et al. [102] reported the increase of photocurrent at the aperture of 300 nm diameters by several tenfold than that without the antenna.

On the other hand, RF antenna is well known to direct the radiation from radiation

source. Usually, the directivity is expressed by the half-power beamwidth (HPBW) defined as the angle between the half power points of the main emission lobe. Smaller HPBW corresponds to the more concentrated radiation. Usually, an infinitesimally small dipole antenna can represent the nanoscale optical emitter, and their HPBW is estimated to be 90 degrees, indicating, for example, that a detector measures only a fraction of the radiation [92]. Consequently, the exposure time is long to observe the weak fluorescent signal of a single molecule. Intuitively, however, directing the fluorescent radiation to the detector will be possible by procedure similar to the RF antenna, which will contribute to the efficient detection of living cells in the studies of DNA, and protein molecules [45, 58, 103-112]. The efficient antibody test with a few samples will lead to a shorter inspection time, and to the decrease of a burden on patients. The faster detection also contributes to warding off the spread of disease.

Application of optical antennas to the optical information processing on nanoscale was also proposed. Owing to the ability of speedier calculation without heat generation that occurs in metal wire used in CPU, the application is attracting attention [113-117]. For example, a single nanoscale emitter for quantum computing, interface devices between near field and propagating light, wireless optical communication between antenna elements by developing a face-to-face connection, and optical data storage for both writing and reading the data, etc. are expected [92].

Encouraged by these attractive applications, rapid progress has been made in the realization of directional control of light with optical antennas. For instance, in 2007, Taminiau, et al. [118, 119] demonstrated the directional control of light ($\lambda = 514$ nm) by $\lambda/4$ antenna at the apex of the probe of SNOM/NSOM. The antenna design showed a qualitative similarity to that of the RF antennas, but the element length was reduced than in the case of the RF antenna. The effect of plasmon causes the difference, which is similar to the result of the half-wave length type antenna described above [95].

Obvious fact that the plasmon effect in the antenna elements should be considered in the realization of optical antennas suggests that the adoption of antenna theory to optical frequencies is not straightforward. However, as seen above, applying the concept of RF antenna to the optical wave will contribute to the realization of novel nanoscale optical devices.

1.3. Purpose of this work

According to the RF antenna technology, directivity of a dipole antenna can be increased by an appropriate arrangement of dipoles that interact with the radiation source. The RF Yagi-Uda antenna is known to achieve the high directivity by a linear array of properly tuned antenna elements. Figure 1.9 shows a typical geometry. The antenna is driven only by a feed element, and the radiation from the feed drives the other passive elements. Due to its simple structure and design, RF Yagi-Uda antennas have been used worldwide for home TV, radio communication, and radar, etc [120, 121].

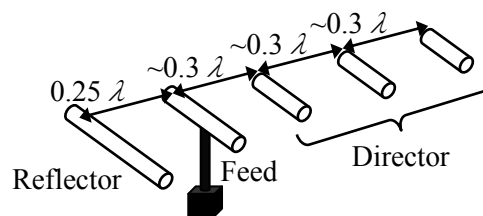


Fig. 1.9: Typical geometry of a five-element RF Yagi-Uda antenna.

What has inspired this work is the idea that the concept of the RF Yagi-Uda antennas might be applied to the optical antennas. According to the scaling law, the element size and its spacing would be around a fraction of the wavelength. This indicates the use of metal nanoparticles as the antenna elements. Undoubtedly, LSPR should be considered in the design, and precise arrangement of nanoparticles on nanoscale is necessary. This implies the difficulty of design, fabrication, and directivity measurement.

However, there are attractive applications that make the effort worth challenging. Since the Yagi-Uda antenna is driven only through the feed, it is very advantageous for the directional control of single nano emitters. For example, it will contribute to the efficient detection of fluorescent molecule by putting the molecule at the feed position. Additionally, if the reciprocity of RF antenna is applicable, wireless communication between two optical Yagi-Uda antennas arranged face-to-face is expected.

The purpose of this work is the clarification of the design and the realization of directional control of light by an optical Yagi-Uda antenna [122, 123] consisting of metal nanoparticles. Around the same time of this work, J. Li, et al. [124, 125] has independently proposed the design of optical Yagi-Uda antenna but with different elements. They considered core-shell nanoparticles, which are much more difficult to realize than our proposal using simple metal nanoparticles, though the material loss

could be a significant issue in our case. This work will validate that utilizing the interaction between nanoparticles and adjusting carefully the shape of the nanoparticle to the detuning are able to attain a similar function to that of RF Yagi-Uda antennas. The result may encourage the development of further applications of RF technology to the optical frequency regime.

1.4. Structure of this thesis

Figure 1.10 shows the contents of this thesis. Chapter 1 has described the background and the purpose of this work. Chapter 2 will describe the dipole model of a single metal nanoparticle, and the coupled dipole model that expresses the interaction between nanoparticles. Based on this theoretical model, Chapter 3 will estimate how the interparticle action affects the characteristics of the plasmon resonance. Chapter 4 will explain in detail the design of a nano optical Yagi-Uda antenna by the coupled dipole model. The effect of material losses on the performance of the antenna will be considered. The behavior of reflector and director on the directivity of the antenna will be clarified. On the basis of the antenna design obtained in Chapter 4, Chapter 5 will describe the experimental validation that the nano optical Yagi-Uda antenna is able to give high directivity to the optical emission in almost the same way as an RF Yagi-Uda antenna does. The antenna is fabricated on a glass substrate by adopting the electron beam lithography and lift-off process. The detail of the fabrication process will also be described. The emission pattern from the optical antennas is measured by a set-up specially designed for this work, based on the measurement systems for RF antennas [126]. Chapter 6 will summarize the important findings and conclusions of this work.

Chapter 1 Introduction
•Background & Purpose
Chapter 2 Theoretical Model
•Single particle (dipole model)
•Coupled dipole model
Chapter 3 Interparticle Interaction
•Example of coupled dipole model
Chapter 4 Design of Antenna
•Comparison between Radio frequency and Optical frequency
•Design method
Chapter 5 Experimental Result
•Measurement set-up
•Directivity
Chapter 6 Conclusion
•Research findings
•Further studies & Promising development

Fig. 1.10: Contents of this thesis.

2. Localized surface plasmon resonance in metal nanoparticles

In this work, a simple theory for describing the optical response of a nanoparticle array to the external input is developed to design an optical Yagi-Uda antenna using the interaction between nanoparticles [122]. In the development of the theory, both the optical response of a single nanoparticle (Section 2.1) and that of a finite linear array of nanoparticles (Section 2.2) are considered.

2.1. Optical response of a single nanoparticle

The theory of the optical response of nanoparticles small enough compared with the wavelength of the incident light is summarized in this section [37].

2.1.1. Mie theory

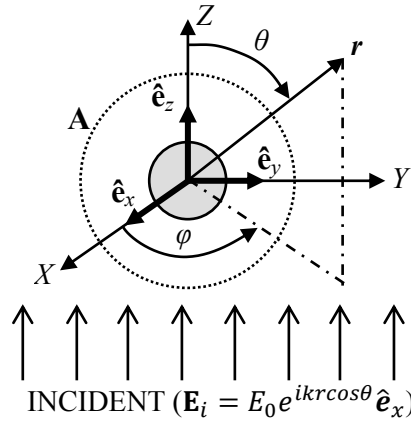


Fig.2.1: Scattering of a spherical particle.

In 1908, G. Mie established an exact solution for the optical response of a spherical nanoparticle [36]. Figure 2.1 shows the schematic illustration of scattering a plane wave by a spherical particle of radius a , refractive index N_1 , surrounded by a uniform medium of refractive index N_m . The orthonormal basis vectors $\hat{\mathbf{e}}_x$, $\hat{\mathbf{e}}_y$, $\hat{\mathbf{e}}_z$ are in the directions of the positive X , Y , and Z axes in the Cartesian coordinate system. The Z -axis is the propagation direction of the incident light which is assumed to be a plane x -polarized wave written in spherical polar coordinates as $\mathbf{E}_i = E_0 e^{ikrcos\theta} \hat{\mathbf{e}}_x$. The scattering

cross-section C_{sca} of the spherical particle is given by Eq. (2.1).

$$C_{sca} = \frac{W_{sca}}{I_i} = \frac{2\pi}{k^2} \sum_{n=1}^{\infty} (2n+1) (|a_n|^2 + |b_n|^2) \quad (2.1)$$

Here, W_{sca} is the energy fraction passing through the surface A of an imaginary sphere centered at the particle, I_i is the flux density of the incident light, $k=2\pi N_m/\lambda$ is the wavenumber of the incident light of wavelength λ . The mode of scattering is designated by n , for example, $n=1$, dipole; $n=2$, quadrupole. Under the condition that the permeability of the particle is the same as that of the surrounding medium, scattering coefficients a_n and b_n are given by Eq. (2.2) and Eq. (2.3), respectively.

$$a_n = \frac{m[\Psi_n(mx)][\Psi'_n(x)] - [\Psi_n(x)][\Psi'_n(mx)]}{m[\Psi_n(mx)][\xi'_n(x)] - [\xi_n(x)][\Psi'_n(mx)]} \quad (2.2)$$

$$b_n = \frac{[\Psi_n(mx)][\Psi'_n(x)] - m[\Psi_n(x)][\Psi'_n(mx)]}{[\Psi_n(mx)][\xi'_n(x)] - m[\xi_n(x)][\Psi'_n(mx)]} \quad (2.3)$$

$$x = ka = \frac{2\pi N_m a}{\lambda}, \quad m = \frac{N_1}{N_m} \quad (2.4)$$

Here, Ψ_n and ξ_n are Riccati-Bessel functions expressed as Eq. (2.5) that is given by Eq. (2.6) ~ Eq. (2.8). Equation (2.6) is the spherical Hankel function, Eq. (2.7) and Eq. (2.8) are the spherical Bessel functions.

$$\psi_n(\rho) = \rho j_n(\rho), \quad \xi_n(\rho) = \rho h_n^{(1)}(\rho) \quad (2.5)$$

$$h_n^{(1)}(\rho) = j_n(\rho) + iy_n(\rho) \quad (2.6)$$

$$j_n(\rho) = \frac{\rho^n}{1 \cdot 3 \cdot 5 \cdots (2n+1)} \left[1 - \frac{\frac{1}{2}\rho^2}{1!(2n+3)} + \frac{\left(\frac{1}{2}\rho^2\right)^2}{2!(2n+3)(2n+5)} - \cdots \right] \quad (2.7)$$

$$y_n(\rho) = -\frac{1 \cdot 3 \cdot 5 \cdots (2n-1)}{\rho^{n+1}} \left[1 - \frac{\frac{1}{2}\rho^2}{1!(1-2n)} + \frac{\left(\frac{1}{2}\rho^2\right)^2}{2!(1-2n)(3-2n)} - \cdots \right] \quad (2.8)$$

The resonance of the scattering occurs when the real part of the denominator of Eq. (2.2) or Eq. (2.3) is zero, and the scattering cross-section C_{sca} becomes resonantly large. The resonance condition depends on the refractive index of the surrounding medium N_m , the particle radius a , and the wavelength of the incident light λ .

2.1.2. Quasi static approximation

In this section, the quasi static approximation is considered which is valid under the condition that the particle radius a is sufficiently smaller than the incident wavelength λ ; ($a \ll \lambda$) [37]. When only the first few terms of a_n and b_n in Eq. (2.2) and Eq. (2.3) are considered, the approximate expression up to the term of x^6 is obtained as follows.

$$\begin{aligned} a_1 &= -\frac{i2x^3}{3} \frac{m^2 - 1}{m^2 + 2} - \frac{i2x^5}{5} \frac{(m^2 - 2)(m^2 - 1)}{(m^2 + 2)^2} + \frac{4x^6}{9} \left(\frac{m^2 - 1}{m^2 + 2} \right)^2 + O(x^7), \\ b_1 &= -\frac{ix^5}{45} (m^2 - 1) + O(x^7), \\ a_2 &= -\frac{ix^5}{15} \frac{(m^2 - 1)}{2m^2 + 3} + O(x^7), \\ b_2 &= O(x^7) \end{aligned} \quad (2.9)$$

When $a \ll \lambda$, the size-parameter x defined in Eq. (2.4) is in the range of $x \ll 1$. With this assumption, a_1 can be further simplified as Eq. (2.10).

$$a_1 \approx -\frac{i2x^3}{3} \frac{m^2 - 1}{m^2 + 2}, \quad |b_2|, |a_2|, |b_1| \ll |a_1| \quad (2.10)$$

By substituting Eq. (2.10) and Eq. (2.4) in Eq. (2.1), the approximate expression of the scattering cross-section C_{sca} of the spherical particles is given as Eq. (2.11).

$$C_{sca} \approx \frac{8}{3} \pi k^4 a^6 \left| \frac{\varepsilon_1 - \varepsilon_m}{\varepsilon_1 + 2\varepsilon_m} \right|^2 \quad (2.11)$$

Here, $\varepsilon_1 = N_1^2$ is the dielectric constant of the particle, and $\varepsilon_m = N_m^2$ is that of the surrounding medium. The quantity $(\varepsilon_1 - \varepsilon_m)/(\varepsilon_1 + 2\varepsilon_m)$ suggests a connection to the problem of a sphere embedded in a uniform static electric field [37].

The following is the consideration of a homogeneous, isotropic dielectric particle of the radius a placed in the uniform static electric field \mathbf{E}_0 with the surrounding medium uniform. Figure 2.2 shows the calculation model. The orthonormal basis vector $\hat{\mathbf{e}}_z$ is in the direction of the positive Z , the center of the particle being set at $Z=0$. The dielectric constant of the particle is ϵ_1 , and that of the surrounding medium is ϵ_m .

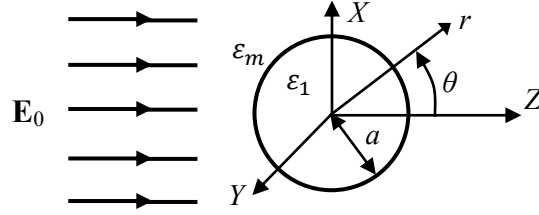


Fig. 2.2: Sphere in a uniform electrostatic field.

The polarizability α of the particle is given as Eq. (2.12), since the polarization induced in the particle placed in an electrostatic field is equivalent to a dipole with the dipole moment $\epsilon_m \alpha \mathbf{E}_0$ at $Z=0$.

$$\alpha = 4\pi a^3 \frac{\epsilon_1 - \epsilon_m}{\epsilon_1 + 2\epsilon_m} \quad (2.12)$$

Let us assume the same dipole in the case that the incident field is an x -polarized plane wave $E_0 \exp(ikz - i\omega t)$. Then the dipole moment $\mathbf{p} = \epsilon_m \alpha E_0 \exp(-i\omega t) \hat{\mathbf{e}}_x$ is induced at $Z=0$ oscillating with the frequency of the incident field. The scattering cross-section C_{sca} is given as follows.

$$C_{sca} = \frac{k^4}{6\pi} |\alpha|^2 \quad (2.13)$$

By substituting Eq. (2.12) into Eq. (2.13), Eq. (2.14) is obtained.

$$C_{sca} = \frac{8}{3} \pi k^4 a^6 \left| \frac{\epsilon_1 - \epsilon_m}{\epsilon_1 + 2\epsilon_m} \right|^2 \quad (2.14)$$

Equation (2.14) is the same as Eq. (2.11) that is obtained from the exact theory in the limit of $ka \ll 1$. In general, the approximation Eq. (2.11) is called quasi static approximation.

2.1.3. Ellipsoidal metal particle

Although the actual shape of the nanoparticles fabricated in this work is like a disk or a rectangular block, a nanoparticle is assumed to be ellipsoid in the theoretical model, because there is no approximation theory for irregularly shaped particles except for the ellipsoid [37]. Figure 2.3 shows the ellipsoidal model. Semiminor axes a , b , and c ($a \geq b \geq c$) are parallel to the x , y , and z axes defined in Cartesian coordinate system, in which the center of ellipsoid is set as the center of the system. In order to obtain the polarizability of ellipsoid with rotational symmetries, the traditional approach to the solution of the Poisson equation has been adopted. For an ellipsoid of volume $V(=4\pi abc/3)$ and dielectric constant ε_p embedded in a homogeneous medium of dielectric constant ε_m , the approximation of the polarizability α_j in the field parallel to one of its principal axes j ($=x, y, z$) is given by Eq. (2.15).

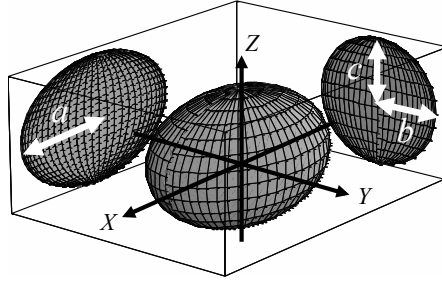


Fig. 2.3: Ellipsoidal model. The relations between the semiminor axes are $a \geq b \geq c$.

$$\alpha_j = V \frac{\varepsilon_p - \varepsilon_m}{\varepsilon_m + N_j(\varepsilon_p - \varepsilon_m)}, \quad (j = x, y, z) \quad (2.15)$$

$$N_j = \frac{abc}{2} \int_0^\infty \frac{1}{(j^2 + q)} \frac{1}{\sqrt{(q+a^2)(q+b^2)(q+c^2)}} dq, \quad (j = x, y, z) \quad (2.16)$$

$$N_x + N_y + N_z = 1 \quad (2.17)$$

Here N_j is the shape-dependent depolarization factor. For example, to an electric field parallel to the x -axis, N_x can be adjusted by varying the aspect ratio between the length a along x and the perpendicular width b and c of the ellipsoid. The analytical expression of N_j is already available for the sphere ($a=b=c$), the oblate spheroid ($a=b>c$), and the prolate spheroid ($a>b=c$) [37, 127]. In this work, since the width and the thickness of

nanoparticles are designed to be equal, the shape of nanoparticles is assumed to be a prolate spheroid for which the analytical expression of N_x , N_y , and N_z is given by Eq. (2.18)~Eq. (2.20). The aspect ratio dependence of N_x is shown in Fig.2.4.

$$N_x = \frac{1}{m^2-1} \left\{ \frac{m}{2\sqrt{m^2-1}} \times \ln \left(\frac{m+\sqrt{m^2-1}}{m-\sqrt{m^2-1}} \right) - 1 \right\} \quad (2.18)$$

$$N_y = N_z = \frac{1}{2} (1 - N_x) \quad (2.19)$$

$$m = \frac{a}{b} = \frac{a}{c} \quad (2.20)$$

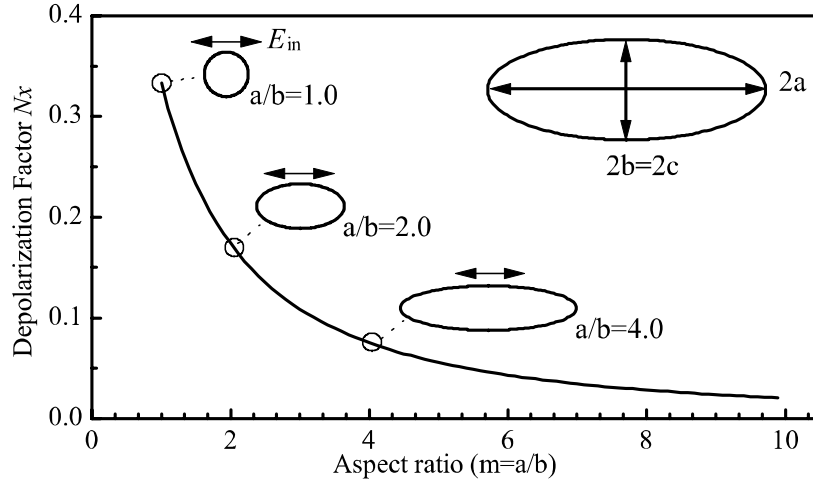


Fig. 2.4: Dependence of the shape-dependent depolarization factor N_x on the aspect ratio of a prolate spheroid for which the analytical expression is given by Eq. (2.18)~Eq. (2.20) [37, 127]. The relations between the semiminor axes are $a > b = c$. Arrows next to each shape show the direction of the incident electric field.

2.1.4. Expression for the response of a point dipole including radiation damping

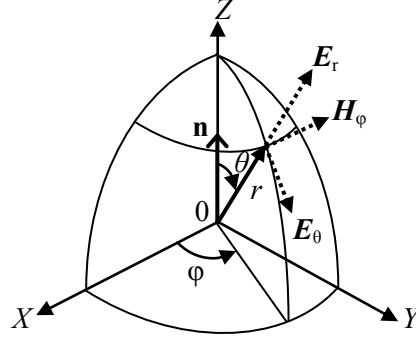


Fig. 2.5: Polar coordinates for dipole field.

In this section, a point dipole placed at the origin in the polar coordinates is considered to describe the nanoparticle's optical response to the incident field. Figure 2.5 shows the calculation model. The point dipole, which oscillates in the direction of the unit vector \mathbf{n} , is given by Eq. (2.21) [4]. Here $\delta(r)$ is the Dirac delta function.

$$\mathbf{p}(r, t) = p(t)\delta(r)\mathbf{n} \quad (2.21)$$

As for an oscillating dipole emitting into a homogeneous medium of dielectric constant ϵ_m , the electromagnetic field is determined by Hertz's solution. At a point $\mathbf{r}(|\mathbf{r}|=r)$ from the oscillating dipole \mathbf{p} with $\mathbf{n}=\hat{\mathbf{e}}_z$, the electromagnetic field at time t is given as follows.

$$\mathbf{E}(r, \theta, \varphi, t) = \frac{1}{4\pi\epsilon_m} \left\{ \left(\frac{2[p]}{r^3} + \frac{2[\dot{p}]}{vr^2} \right) \cos \theta \hat{\mathbf{e}}_r + \left(\frac{[p]}{r^3} + \frac{[\dot{p}]}{vr^2} + \frac{[\ddot{p}]}{v^2r} \right) \sin \theta \hat{\mathbf{e}}_\theta \right\} \quad (2.22)$$

$$\mathbf{H}(r, \theta, \varphi, t) = \frac{1}{4\pi} \left(\frac{[\dot{p}]}{r^2} + \frac{[\ddot{p}]}{vr} \right) \sin \theta \hat{\mathbf{e}}_\varphi \quad (2.23)$$

Here, the square bracket '[]' denotes the retarded-value, and in $[p] = p(\mathbf{r}, t-r/v)$, v is the phase velocity. When $p(t) = d\exp(-i\omega t)$, $[p(t)] = d\exp\{-i\omega(t-r/v)\}$ is obtained. Therefore Eq. (2.24) and Eq. (2.25) are obtained.

$$\begin{aligned} \mathbf{E}(r, \theta, \varphi) = \frac{d}{4\pi\epsilon_m} \left\{ \left(\frac{2}{r^3} - i\omega \frac{2}{vr^2} \right) \cos\theta \hat{\mathbf{e}}_r \right. \\ \left. + \left(\frac{1}{r^3} - i\omega \frac{1}{vr^2} - \frac{\omega^2}{v^2 r} \right) \sin\theta \hat{\mathbf{e}}_\theta \right\} \exp\left(i\omega \frac{r}{v}\right) \end{aligned} \quad (2.24)$$

$$\mathbf{H}(r, \theta, \varphi) = \frac{1}{4\pi} \left(-i \frac{\omega}{r^2} - \frac{\omega^2}{vr} \right) \sin\theta \hat{\mathbf{e}}_\varphi \exp\left(i\omega \frac{r}{v}\right) \quad (2.25)$$

In the far-field, the terms proportional to $1/r$ in Eq. (2.22) and Eq. (2.23) are dominant. Therefore, the pointing vector is given by Eq. (2.26) using Eq. (2.22) and Eq. (2.23).

$$\mathbf{E}(r, t) \times \mathbf{H}(r, t) = \frac{1}{16\pi^2 \epsilon_m v^3 r^2} [\ddot{p}]^2 \sin^2\theta \hat{\mathbf{e}}_r \quad (2.26)$$

The total radiation intensity per the unit time P_{rad} is given as Eq. (2.27) by integrating Eq. (2.26) on the sphere with the radius r .

$$\begin{aligned} P_{rad} &= \int_0^{2\pi} \int_0^\pi \left(\frac{1}{16\pi^2 \epsilon_m v^3 r^2} [\ddot{p}]^2 \sin^2\theta \right) r^2 \sin\theta \, d\varphi d\theta \\ &= \frac{1}{6\pi \epsilon_m v^3} [\ddot{p}]^2 \end{aligned} \quad (2.27)$$

Therefore the energy lost by the dipole radiation in the time between t_1 and t_2 is given as follows.

$$\begin{aligned} W_{rad} &= \int_{t_2}^{t_1} \frac{1}{6\pi \epsilon_m v^3} [\ddot{p}]^2 dt \\ &= \frac{1}{6\pi \epsilon_m v^3} \left| \left[\frac{\partial p}{\partial t} \frac{\partial^3 p}{\partial t^3} \right]_{t_1}^{t_2} - \int_{t_1}^{t_2} \frac{\partial p}{\partial t} \frac{\partial^3 p}{\partial t^3} dt \right| \end{aligned} \quad (2.28)$$

By choosing the time t_1 and the time t_2 so that the first term of the right-hand side of Eq. (2.28) becomes zero, Eq. (2.29) is obtained.

$$W_{rad} = \frac{1}{6\pi \epsilon_m v^3} \left| \int_{t_1}^{t_2} \frac{\partial p}{\partial t} \frac{\partial^3 p}{\partial t^3} dt \right| \quad (2.29)$$

On the other hand, the energy loss is caused by the action of the electromagnetic radiation, that is to say, the electric field E_{reac} generated by the electromagnetic radiation of a dipole may affect the dipole itself. Then W_{rad} can be equated to the amount of the work done by the electric field E_{reac} on the dipole,

$$\int_{t_1}^{t_2} E_{reac} \frac{\partial p}{\partial t} dt \quad (2.30)$$

By comparing Eq. (2.29) with Eq. (2.30), Eq. (2.31) is obtained.

$$E_{reac} = i \frac{4\pi^2}{3\epsilon_m \lambda^3} d \quad (2.31)$$

Here $\lambda(=2\pi\nu/\omega)$ expresses the wavelength in the medium. In the linear response, the dipole moment d induced by the incident field E_{in} is expressed as follows.

$$d = \epsilon_m \alpha E_{in} \quad (2.32)$$

Here α is the polarizability. By rewriting Eq. (2.32), the expression for d including the reaction field E_{reac} is obtained as follows.

$$d = \epsilon_m \alpha (E_{in} + E_{reac}) = \epsilon_m \alpha \left(E_{in} + i \frac{4\pi^2}{3\epsilon_m \lambda^3} d \right) \quad (2.33)$$

Then Eq. (2.34) is obtained for the dipole in terms of the incident field E_{in} .

$$d = \epsilon_m \frac{\alpha}{1 - i\alpha \frac{4\pi^2}{3\lambda^3}} E_{in} \quad (2.34)$$

In the case when the polarizability is expressed in terms of the shape-dependent depolarization factor, α is described as Eq. (2.15), or simply as Eq. (2.35).

$$\alpha = \frac{1}{N + \frac{\epsilon_m}{\epsilon_p - \epsilon_m}} V \quad (2.35)$$

By substituting Eq. (2.35) into Eq. (2.34), the dipole moment d induced by the incident field E_{in} , including the effect of the radiation loss, is given as follows.

$$d = \varepsilon_m \frac{\left(\frac{\varepsilon_p}{\varepsilon_m} - 1\right)V}{1 + N\left(\frac{\varepsilon_p}{\varepsilon_m} - 1\right) - i\left(\frac{\varepsilon_p}{\varepsilon_m} - 1\right)\frac{4\pi^2 V}{3\lambda^3}} E_{in} \quad (2.36)$$

Equation (2.36) can be simplified, as follows.

$$d = i \frac{3\varepsilon_m \lambda^3}{4\pi^2} \frac{E_{in}}{1 + \gamma - i\delta} \quad (2.37)$$

$$\gamma = \frac{1}{R} \frac{\text{Im}(\varepsilon_r)}{|\varepsilon_r - 1|^2} \quad (2.38)$$

$$\delta = -\frac{1}{R} \left(N + \frac{\text{Re}(\varepsilon_r - 1)}{|\varepsilon_r - 1|^2} \right) \quad (2.39)$$

$$R = \frac{4\pi^2 V}{3\lambda^3} \quad (2.40)$$

Here, γ expresses the material loss and δ does the detuning relative to the radiation loss. The parameter $\varepsilon_r (= \varepsilon_p / \varepsilon_m)$ is the ratio of the complex dielectric constant of the nanoparticle ε_p to the permittivity of the surrounding medium ε_m . The relation between the detuning δ and the depolarization factor N is given by Eq. (2.39). Once the volume V is fixed, δ can be determined by varying N , which can be estimated by the aspect ratio of the nanoparticles as shown in Section 2.1.3. For example, a gold nanoparticle with the resonant wavelength $\lambda_0 = 660$ nm ($\delta = 0$) in vacuum, its width $2b$, thickness $2c$, and length $2a$ are estimated to be $2b = 2c = 52.7$ nm and $2a = 125$ nm, corresponding to 0.29λ inside a glass ($\lambda = 435$ nm, $\varepsilon_m = 2.3$).

2.2. Coupled dipole model for one-dimensional nanoparticle arrays

As shown in the previous sections, a small metal nanoparticle can be assumed to be a dipole. Therefore, it is realistic to describe a finite linear array of nanoparticles by an interacting dipole chain [122]. In order to consider the interactions in a nanoparticle array, a coupled dipole model is developed on the basis of the dipole model described in Section 2.1.4. By substituting $X=(2\pi r)/\lambda$, $\omega=\nu k$, $\hat{\mathbf{e}}_\theta = -\hat{\mathbf{e}}_z$, $\theta=\pi/2$, and the wavenumber $k=2\pi/\lambda$ in the Eq. (2.24), the electric field E_z parallel to the dipole radiated from an infinitesimally small oscillating dipole d at a distance of r perpendicular to the orientation can be given as Eq. (2.41).

$$E_z(X) = i \frac{3}{2} \frac{4\pi^2 d}{3\epsilon_m \lambda^3} \frac{1}{X^3} (i + X - iX^2) \exp(iX) \quad (2.41)$$

Here, λ is the emitting wavelength in a homogeneous medium of the dielectric constant ϵ_m . By substituting Eq. (2.37) into Eq. (2.41), the following equations are obtained as the description of the radiation from the oscillating dipole induced by the incident field E_{in} .

$$E_z(X) = E_{rad} A(X) \quad (2.42)$$

$$E_{rad} = \frac{E_{in}}{1+\gamma-i\delta} \quad (2.43)$$

$$A(x) = -\frac{3}{2} \frac{1}{X^3} (i + X - iX^2) \exp(iX) \quad (2.44)$$

Based on these equations, the responses of a finite linear array of dipoles are considered. Figure 2.6 shows an example of the calculation model consisting of five particles. The incident field E_{in} simultaneously drives the particles. Each nanoparticle reradiates the field E_{rad} . Each element is driven by the sum of the incident field and the field radiated from other elements, as described by Eq. (2.45). They form a system of N linear equations, where N is the number of nanoparticles [122].

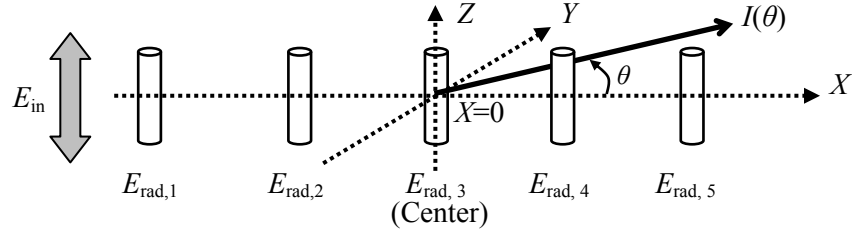


Fig. 2.6: Example of a one-dimensional array consisting of five particles. Particles are aligned in the X -direction, and the incident field E_{in} is polarized parallel to the Z -axis.

$$E_{rad,n} = \frac{1}{1+\gamma_n-i\delta_n} (E_{in} + \sum_{m \neq n} A(|X_n - X_m|) E_{rad,m}) \quad (2.45)$$

By solving the equations Eq. (2.45) for all the elements consistently, the ratio between the radiation $E_{rad,n}$ and the incident field E_{in} is obtained.

2.3. Dielectric constant of gold

In this work, gold is used as the antenna element. In the theory and the finite difference time domain (FDTD) simulations, the dielectric constants of gold are expressed as the sum of the Drude and the Lorentz functions, with the parameters obtained by fitting the experimental values of the bulk gold reported by Johnson and Christy [38]. The fitting equation is shown in Appendix I. The fitting of the real part requires high accuracy, since it corresponds to the resonant wavelength as described in Sec. 1.1.2.

Figure 2.7 shows the fitting result. The solid square marks (\blacklozenge , \blacktriangle) and the open square marks (\diamond , \triangle) show the reported experimental values and the approximation, respectively. In this work, the wavelength range of 400 nm ~ 900 nm is used.

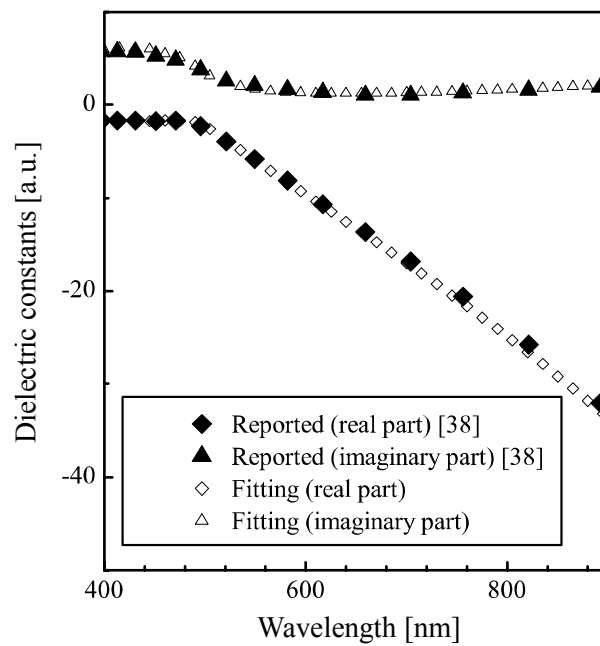


Fig. 2.7: Fitting the measured dielectric constants of gold given by Johnson & Christy [38]. Solid (\blacklozenge) and open (\diamond) marks show the reported values and fitting results for the real part, respectively. Solid (\blacktriangle) and open (\triangle) marks show the reported values and the fitting results for the imaginary part, respectively.

3. Resonance in nanoparticle array

The interaction between the metal nanoparticles, which can be described by the coupled dipole model given in the previous chapter, is a key factor for operating the optical Yagi-Uda antenna. The interaction-induced modification of localized surface plasmon resonance (LSPR) in the metal nanoparticles is also expected to be useful for sensitive plasmon sensors [67-72]. On the other hand, the effect makes it difficult to evaluate the resonance wavelength of metal nano-patterns by a spectroscopic measurement done with an array of the nano-patterns applied to enhance the detection signal. Therefore, it is important to estimate how the interaction affects the characteristics of the plasmon resonance. In this chapter, the dependence of the effect on the distance between the particles arranged in a linear array is evaluated both theoretically and experimentally.

3.1. Dipole model prediction

The calculation model is the same as that shown in Fig. 2.6. Under the condition that the infinitesimal dipoles are equally spaced, the effect of interaction between particles on the resonant wavelength (frequency) of the LSPR is considered. Each element is driven by the incident field $E_{in}=1$ and the field radiated from the other elements. According to Eq. (2.45), they form a system of N linear equations, where N is the number of nanoparticles.

$$E_{rad,n} = \frac{1}{1+\gamma_n-i\delta_n} \left(1 + \sum_{m \neq n} A(|X_n - X_m|) E_{rad,m}\right) \quad (3.1)$$

The $E_{rad,n}$ is obtained by the method described in Section 2.2. The emission intensity detected at the Y -direction, as is determined in Fig. 2.6 is given as the superposition of the radiation from all elements, as given by Eq. (3.2). Here θ is the angle between the array axis and the emission direction in the X - Y plane determined in Fig. 2.6.

$$I(\theta) = \left| \sum_n E_{rad,n} \exp(-iX_n \cos(\theta)) \right|^2 \quad (3.2)$$

Figure 3.1 shows an example of the dependence of the radiation spectrum emitted in the direction of $\theta=90^\circ$ on the interparticle distance X in the case of five particles. In the

calculation, material losses γ_n was assumed to be 1.0. The LSPR spectrum is given as a function of the particle's detuning δ , which is normalized by the radiation damping Γ_0 . With regard to the frequency of the incident field ω and the resonant frequency of the single particle ω_0 , δ is expressed as $\delta=(\omega-\omega_0)/\Gamma_0$.

In Fig. 3.1, the peak in the radiation intensity is red-shifted for the interparticle distance of $X=6.0$, and blue-shifted for $X=3$ and $X=1.5$ from the LSPR of the single particle ($\delta=0$). Since the material losses γ in Eq. (2.43) and the radiation damping Γ_0 were set to be $\Gamma_0 = \gamma = 1$ in the calculation, the detuning shift of “1” corresponds to 25% of the full-width at half maximum (FWHM) =4 of the single particle.

The dependence of the detuning value, at which the radiation spectrum takes its peak, on the interparticle distance was calculated for various numbers of the particles. Figure 3.2(a) shows the results. As in Eq. (2.45), the distance is given in units of $\lambda/(2\pi)$. In the range of $X < \sim 6.2(r \sim \lambda)$, the resonance blue-shifts with the decrease of X . For $X > 6.2$, the resonance shifts with the period of $X \sim 6.2(r \sim \lambda)$. But the amount of the resonance shift becomes small with the increase of X . The X dependence of the peak shift becomes large with the increase of the number of particles. In the case of seven particles at $X \sim 2.0$, the amount of the blue-shift corresponds to 25% of the FWHM of a single particle. The dependence of the FWHM of the resonance peak on the interparticle distance is also evaluated and shown in Fig. 3.2(b).

Figure 3.2(a) will be used to know the distance suited for the evaluation of the resonant wavelength of nanoparticles. In the experiments shown in Sec. 5.4.2, the interparticle distance was chosen in the range of $8 < X < 12$, since the amount of blue-shift in that range is less than 6.25%(=0.25/4) of the FWHM of the single particle.

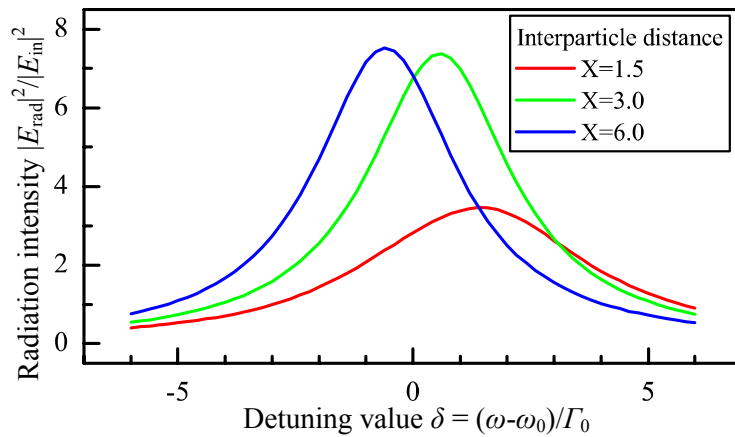
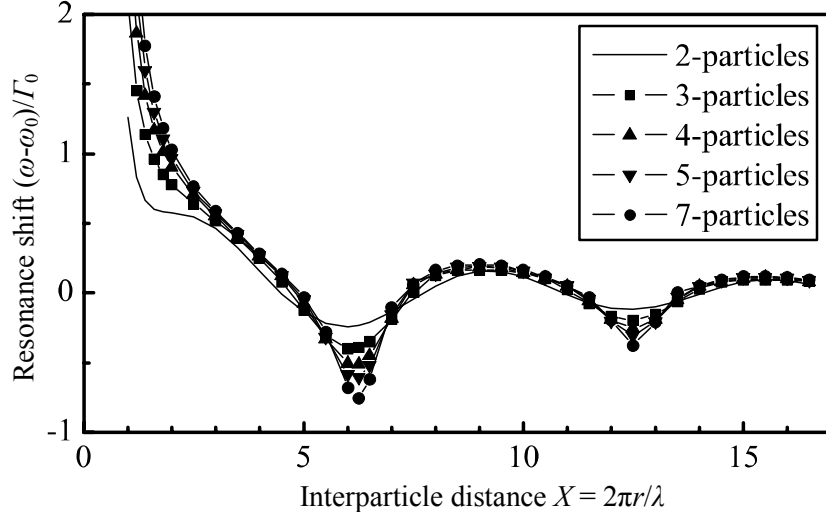
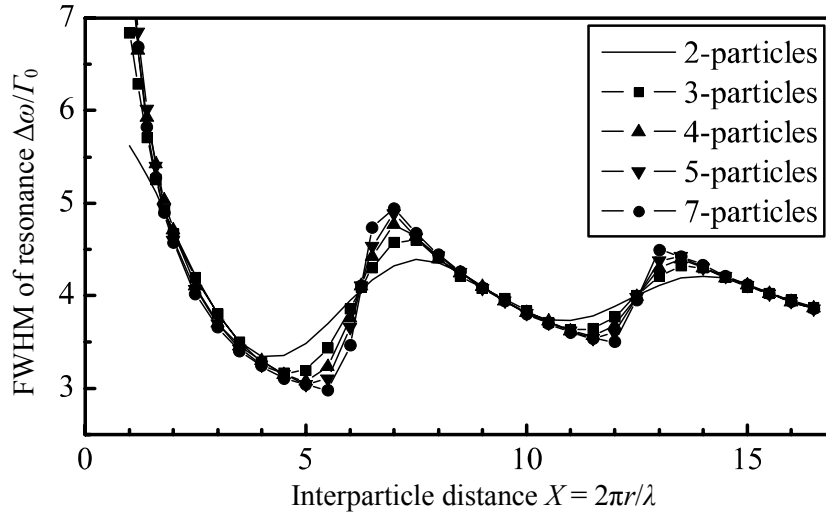


Fig. 3.1: Dependence of the radiation spectrum on the distance between the particles X for a linear array of five particles ($\gamma_n=1.0$, $\Gamma_0=1.0$, $E_{in}=1$, $\theta=90^\circ$).



(a)



(b)

Fig. 3.2: Dependence of the resonance characteristics on the interparticle distance X for a linear array with various numbers of the particles, solid line; two particles, mark (■); three particles, (▲); four particles, (▼); five particles, and (●); seven particles. The dipole parameters are $\gamma_n=1.0$, $\Gamma_0=1.0$, $E_{in}=1.0$, and $\theta=90^\circ$.

3.2. Experimental results

Transmission spectra of gold nanoparticle arrays were measured and compared with the prediction shown in Section 3.1. Figure 3.3 shows the schematic diagram of the samples. The arrays consisting of 50-nm-thick gold nanoparticles were fabricated lithographically on a glass substrate with the area of $60\ \mu\text{m} \times 60\ \mu\text{m}$ squares. The incident field E_{in} was polarized parallel to the Y -direction as shown in Fig. 3.3 (a). The distance dy was fixed to be 800 nm to suppress the interaction in the Y -direction while dx was varied from 300 nm to 675 nm with a step of 25 nm. The nanoparticles were embedded in a sputter-deposited SiOx ($n \sim 1.44$) to suppress the effects of refractive index discontinuity on the interaction between nanoparticles [123]. Figure 3.4 shows a top-view SEM image and a top-view microscope image of the fabricated samples. The size of the nanoparticles is measured to be ~ 50 nm in width and ~ 100 nm in length.

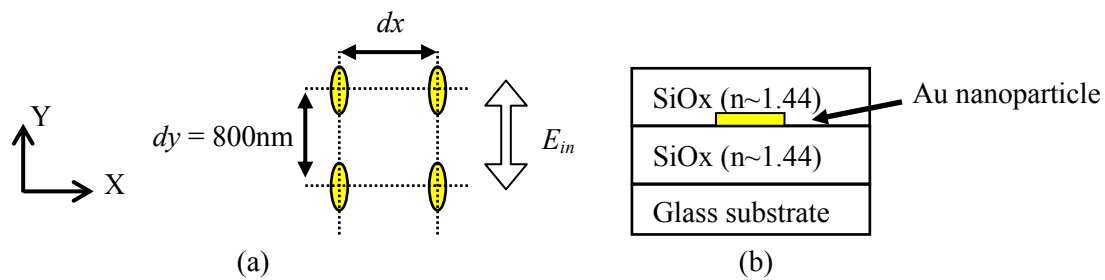


Fig. 3.3: Schematic diagram of the sample. (a) Top view of the sample. The pitch in the Y -direction was fixed to be $dy=800$ nm for all the samples. Incident field E_{in} was polarized parallel to the Y -direction. (b) Side view of the sample. Gold nanoparticles were embedded in a sputter-deposited 100-nm-thick SiOx ($n \sim 1.44$).

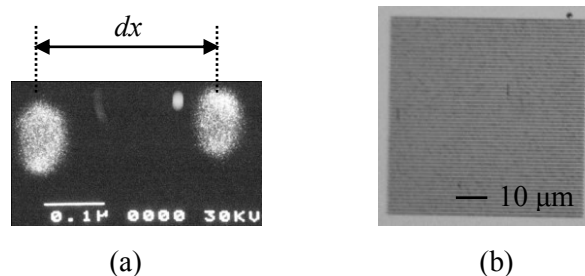


Fig. 3.4: (a) Top-view SEM image and (b) Top-view microscope image of the gold nanoparticle array fabricated in an area of $60\ \mu\text{m} \times 60\ \mu\text{m}$ with various $dx(=300\sim 675\ \text{nm})$.

Figure 3.5 shows the transmission spectra of various interparticle distance dx . The resonant wavelength (dip wavelength of each spectrum) for $dx=650$ nm and $dx=675$ nm were not estimated, because two peaks were observed in both cases. Figure 3.6 shows the dependence of the resonant wavelength on the distance parameter $X=2\pi dx/\lambda_{\text{med}}$. Here, λ_{med} is the resonance wavelength of a single nanoparticle in the medium estimated as follows. In the prediction shown in Fig. 3.2(a), the maximum red-shift is obtained when $dx(=r)$ is around $dx=\lambda_{\text{med}}$. On the other hand, the maximum red-shift is observed at around $dx=600$ nm in Fig. 3.5. Accordingly, the λ_{med} was assumed to be $\lambda_{\text{med}}=600$ nm. With the increase of X in Fig. 3.6, the resonant wavelength red-shifts in the range of $\sim 3 < X < \sim 6$ ($=300\text{nm} < dx < 600\text{nm}$). This phenomenon is consistent with the prediction based on the coupled dipole model shown in Fig. 3.2(a). The linewidth was not measured, because the shape of the transmission spectra becomes broad, asymmetric, and two peaks appear for $X > 6$ ($dx=600$ nm).

As described in the Section 3.1, the range of $8 < X < 12$ is the proper interparticle distance for the evaluation of the LSPR of each particle from the spectroscopic measurement of the array. When λ_{med} is 600 nm, the range corresponds to $764\text{nm} < dx(=\lambda_{\text{med}}X/2\pi) < 1146\text{nm}$. Based on these evaluations, the nanopattern spacing was set to be $dx=800\text{nm}$ in the resonant wavelength measurement of nanopattern shown in Sec. 5.4.2.

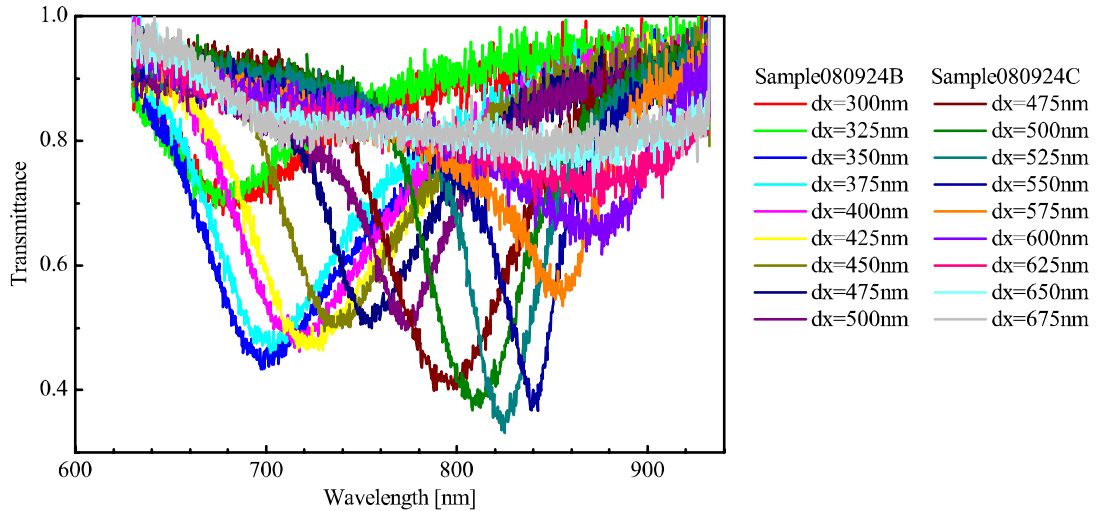


Fig. 3.5: Dependence of the transmission spectra of gold nanoparticle array, embedded in a sputter-deposited 100-nm-thick SiO_x ($n \sim 1.44$), on the distance between nanoparticles. The substrates of Sample-080924B and Sample-080924C were different from each other.

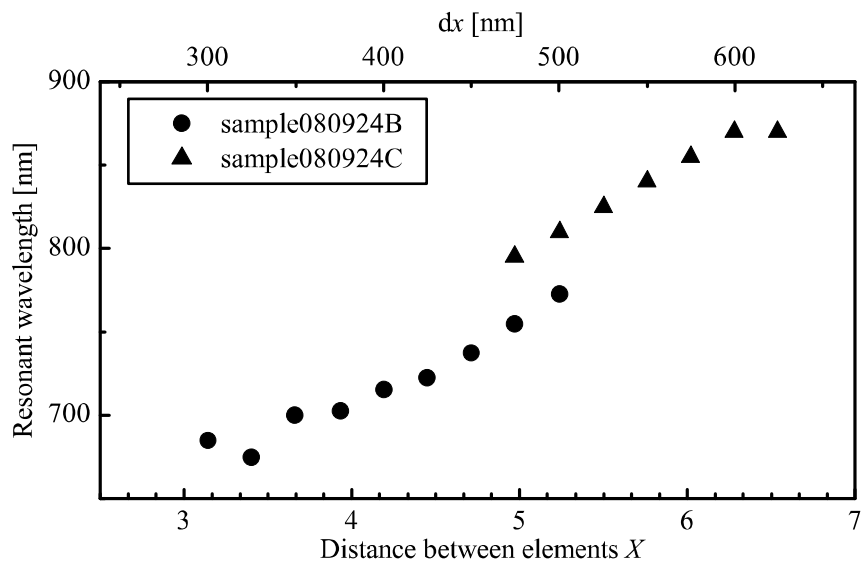


Fig. 3.6: Dependence of the resonant wavelength on the distance parameter $X(=2\pi dx/\lambda_{\text{med}})$ between gold nanoparticles measured by Fig. 3.5. Here, resonant wavelength λ_{med} of single nanoparticle in medium is estimated to be $\lambda_{\text{med}}=600\text{nm}$.

4. Design of nano optical Yagi-Uda antenna

The design of a nano optical Yagi-Uda antenna composed of a finite linear array of nanoparticles will be considered in this chapter. In Section 4.1, the basics of the Yagi-Uda antenna design will be summarized. Then in Section 4.2, the design of the nano optical Yagi-Uda antennas will be described in detail. The design makes use of the coupled dipole model described in Section 2.2. First, 2-element antennas consisting of a feed element and either a reflector or a director will be investigated to confirm the validity of the design concept that both the detuning and the spacing control the function of the passive element. Based on the understanding of the characteristics of the passive element, 3-element and 5-element antennas are designed to realize a desired directivity. Finally, the effect of the material losses on the directivity will be discussed.

4.1. Basics of Yagi-Uda antenna design

4.1.1. Yagi-Uda antenna in radio frequency region

Since the invention by Dr. Yagi and Dr. Uda in 1926, Yagi-Uda antennas have widely been used in the radio frequency (RF) bands [120]. Especially, in the range from VHF (30-300 MHz) to UHF (300-3000 MHz), they have been used worldwide as the antenna receiving the terrestrial broadcasting of television programs. Yagi-Uda antennas are composed of feed, reflector, and director elements made of metal bars as illustrated in Fig. 4.1. Feeding or extracting energy is performed only through the feed element. In the radiation mode, the electromagnetic field emitted from the feed element induces currents in the passive elements, which re-radiate the electromagnetic fields inducing a current in the other element. Such an electromagnetic coupling between the elements decides the oscillating currents in each element and the radiation from them.

The radiation from the multi-element antenna is the superposition of the radiations from each element. Therefore the radiation pattern (directivity) of the antenna depends on both the relative phase and the relative intensity of the radiation from each element. The relative phase and intensity are controlled by the detuning of each element and the spacing between the elements. Figure 4.2 qualitatively shows the impedance $Z = R + jX$ of a linear wire antenna of length L in air for the time dependence $\exp(-j\omega t)$. Note that the sign in the time dependence used here is opposite to the convention in electric engineering. The resonance occurs when L is slightly shorter than half the wavelength

$\lambda/2$. In the case of L longer/shorter than the resonance length, the reactance X is negative/positive corresponding to inductive/capacitive response, while the phase of the induced current is delayed/advanced with respect to the driving voltage. In RF range, the elements cannot be considered to be infinitesimal. It is therefore practically impossible to derive an analytical expression describing the radiation field of the elements. As a result, the optimization of the RF Yagi-Uda antenna has been performed based on the experiments or the numerical simulations. Table 4.1 shows the typical design of Yagi-Uda antenna [120, 121]. Since the dimensions of the antenna are scalable with wavelength in wave phenomena, the design parameters are expressed in terms of the working wavelength of the antenna.

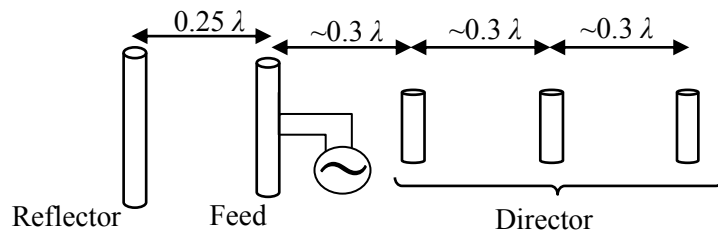


Fig. 4.1: Typical geometry of five-element RF Yagi-Uda antennas. Only the feed element is driven, and directional emission is obtained by the superposition of the electromagnetic field radiated from all the elements.

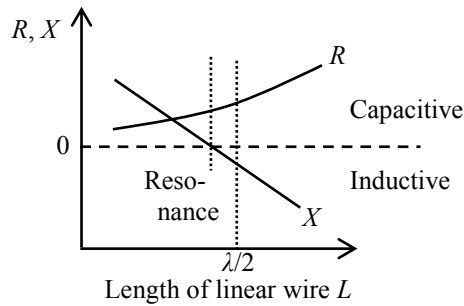


Fig. 4.2: Dependence of the impedance $Z=R+jX$ of a linear wire antenna on its length L .

Table 4.1: Typical design of RF Yagi-Uda antenna for the working wavelength of λ [120].

Element-name	Feed	Director	Reflector
Element-length	$0.45\lambda \sim 0.49\lambda$	$0.4\lambda \sim 0.45\lambda$	$\geq 0.5\lambda$
Current-Phase	Resonant	Capacitive	Inductive
Spacing			$\sim 0.25\lambda$
Typical element number	1	6 ~ 12	1

The feed element is resonantly driven at the working wavelength of λ with its length set to be $0.45\lambda \sim 0.49\lambda$.

The director enhances and sharpens the radiation from the feed element in the director side when the length is $0.4\lambda \sim 0.45\lambda$, which makes the impedance capacitive, i.e. the phase of the current is advanced from the induced electric field. Typically, the element spacing is set to be $0.3\lambda \sim 0.4\lambda$. Although increasing the number of directors can enhance the directivity, the effect becomes small for larger number mostly due to the finite losses in the metal bars. Typically, the number of directors is chosen to be $6 \sim 12$ [120, 121].

The reflector reflects the radiation from the feed when the element length is set to be $\sim 0.5\lambda$, which makes the impedance inductive, i.e. the phase of the current is delayed from that of the induced electric field. The optimum reflector-feed distance is $\sim 0.25\lambda$ [120, 121]. The increase of the number of reflectors has little effect on the gain, because the reflection efficiency of one reflector is sufficiently high.

4.1.2. Optical Yagi-Uda antenna

Since the properties of metals in optical regime are significantly different from those in RF range [38], the wavelength-scaled design of Yagi-Uda antenna is inappropriate, particularly in the control of detuning of each element. In addition, the ohmic loss in metals in optical regime is not negligibly small, which will suppress the interaction between antenna elements. However, once appropriate antenna elements having the same functions as those in RF Yagi-Uda antennas are found, Yagi-Uda antennas can be constructed even in optical regime. That is because the wave propagation phenomena are scalable. In particular, if the elements are dipolar type, the spatial arrangement of the elements can be similar to that of RF Yagi-Uda antennas, since, as mentioned above, the elements of RF Yagi-Uda antennas are designed around the half wavelength resonance of metal bars at which the current (or charge) distribution along the wire is dipolar.

Therefore, it is important to find a dipolar type element with controllable resonance and ohmic loss of acceptable level. As a candidate for such element, metal-dielectric core-shell nanoparticle was proposed by Li et al. [124]. However, the metal-dielectric core-shell structure is not easy to be fabricated and to be arranged spatially with precise control of the resonance condition and position.

In this work, metal nanoparticles showing localized surface plasmon resonance (LSPR) are utilized as the antenna elements. Metal nano patterns can be fabricated and

spatially arranged fairly easily by using electron beam lithography technique. In this section, it is described how the LSPR in metal nanoparticles can be controlled for the antenna elements, with a consideration on the effect of the material loss [122].

The dipolar response of a metal nanoparticle to the incident field $E_{in}exp(-i\omega t)$ is described in Section 2.1.4 as follows.

$$d = i \frac{3 \varepsilon_{med} \lambda^3}{4\pi^2} \frac{E_{in}}{1+\gamma_{mat}-i\delta} \quad (4.1)$$

$$\delta = -\frac{1}{R} \left(N + \frac{\text{Re}(\varepsilon_r-1)}{|\varepsilon_r-1|^2} \right) \quad (4.2)$$

$$\gamma_{mat} = \frac{1}{R} \frac{\text{Im}(\varepsilon_r)}{|\varepsilon_r-1|^2} \quad (4.3)$$

$$R = \frac{4\pi^2 V}{3\lambda^3} \quad (4.4)$$

(a) Detuning

Equation (4.1) and (4.2) indicate that the function of the element can be controlled by adjusting the depolarization factor N as follows. Since the equivalent current is $I \sim -i\omega d \sim E_{in}/(1+\gamma_{mat}-i\delta)$, the element is inductive (capacitive) for $\delta > 0$ ($\delta < 0$). Table 4.2 shows the relation between the depolarization factor N and the function of the elements. Since $\text{Re}(\varepsilon_r-1)$ is negative in the wavelength range considered here, the dipole is inductively (capacitively) detuned when N is smaller (larger) than $|\text{Re}(\varepsilon_r-1)|/|\varepsilon_r-1|^2$. In the case of ellipsoidal nanoparticles, N is adjusted by controlling the aspect ratio of the nanoparticles as described in Section 2.1.4. With the width in the minor axis fixed, a metal rod, whose major axis is longer/shorter than the resonance having smaller/larger N serves as the reflector/director, eventually in the same manner as in RF Yagi-Uda antennas.

Table 4.2: Relation between the shape and the characteristics of LSP-based antenna elements.

		Detuning parameter δ	Characteristics (Function)	Resonant wavelength of the element
Depolarization Factor N	$< \frac{ \text{Re}(\varepsilon_r - 1) }{ \varepsilon_r - 1 ^2}$	> 0	Inductive (Reflector)	$> \lambda_{in}$
	$= \frac{ \text{Re}(\varepsilon_r - 1) }{ \varepsilon_r - 1 ^2}$	$= 0$	Resonance (Feed)	$= \lambda_{in}$
	$> \frac{ \text{Re}(\varepsilon_r - 1) }{ \varepsilon_r - 1 ^2}$	< 0	Capacitive (Director)	$< \lambda_{in}$

(b) Material losses

Equation (4.3) gives the practical idea of estimating the size of an ellipsoidal nanoparticle to be used as antenna element by relating the material losses γ_{mat} to the length of an ellipsoid, which determines the volume V with its aspect ratio (=major-axis/minor-axis). Figure 4.3 shows the dependence of γ_{mat} on the length of an ellipsoidal gold nanorod with a fixed aspect ratio of 2.76 at its resonant wavelength of 705 nm in vacuum, which was calculated using corresponding depolarization factor $N=0.12$ given by Eq. (2.18). In the calculation, the dielectric constant of gold was taken from the literature [38]. Considering that the minimum width (=minor-axis) of the nanoparticle realizable in this work is 50 nm, Fig. 4.3 suggests that a non-negligible loss of $\gamma_{\text{mat}} = 0.28$ is predicted for the length of 138 nm (=50nm x 2.76), corresponding to 0.3λ inside a glass ($\lambda=465$ nm, $n=1.516$). It is therefore inappropriate to exclude the effects of the material losses on the performance of the antenna when the constituent gold nanoparticles are smaller than the working wavelength. However, the loss value is still reasonably low to construct a Yagi-Uda antenna as shown in Section 4.2.5.

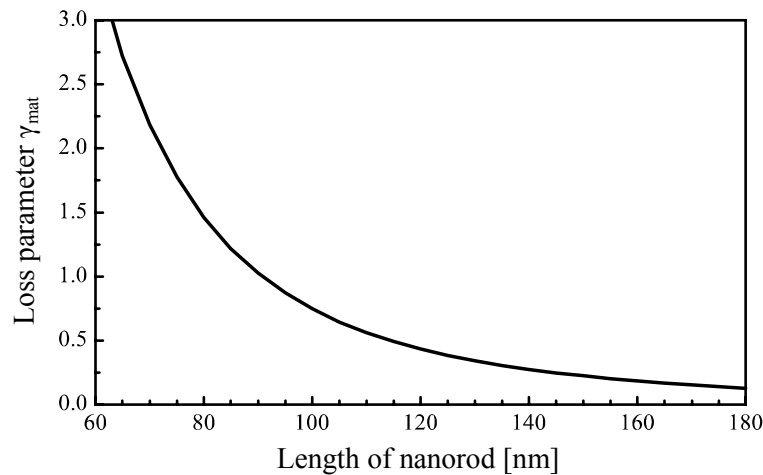


Fig. 4.3: Dependence of the loss parameter γ_{mat} at its resonant wavelength of 705 nm on the length when an ellipsoidal gold nanorod has an aspect ratio of 2.76 [122].

4.2. Design of optical Yagi-Uda antenna

4.2.1. Coupled dipole model

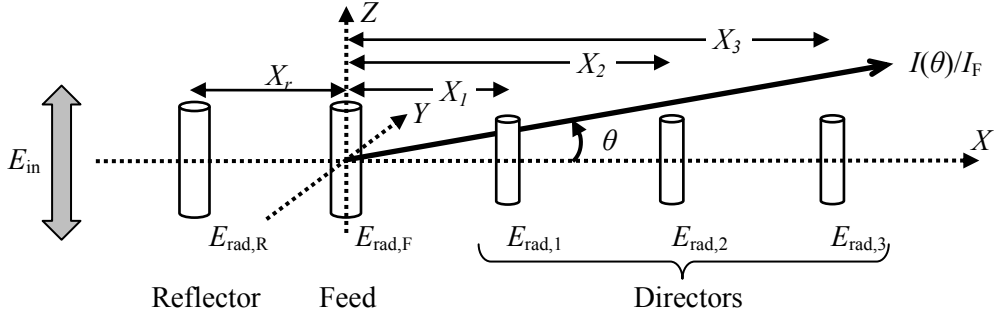


Fig. 4.4: Typical 5-element Yagi-Uda antenna array.

The radiation of a nano-optical Yagi-Uda antenna is the superposition of the radiation from each element as in the case of RF Yagi-Uda antennas. In this work, the phase and the intensity of each element is controlled by adjusting the detuning of the nanoparticle's LSPR and the distance between the elements. The nanoparticle can be assumed as an infinitesimal dipole as shown in Section 2.1.4. It is therefore realistic to describe a nano-optical Yagi-Uda antenna as an interacting dipole chain.

A nano-optical Yagi-Uda antenna is designed on the basis of the coupled dipole model described in Section 2.2 [122]. Figure 4.4 shows the calculation model of a Yagi-Uda antenna which consists of a feed element placed at $X=0$, a reflector at $X_r < 0$, and equally spaced directors at $X_n > 0$. Incident field E_{in} is polarized parallel to the Z -axis. In order to have an enough interaction between the elements to obtain a desired directivity, antenna elements should be placed at distances comparable with the wavelength λ of the emitted radiation. Therefore the description of the interaction should include the electric field of near- and far-field components. In the X - Y plane, the Z -component of the radiation field E_Z at a distance r from the center of an infinitesimally small oscillating dipole is given by Eq. (4.5) ~ Eq. (4.8) as shown in Section 2.2.

$$E_z(X) = E_{rad} A(X) \quad (4.5)$$

$$A(X) = -\frac{3}{2} \frac{1}{X^3} (i + X - iX^2) e^{iX} \quad (4.6)$$

$$E_{rad} = \frac{E_{in}}{1+\gamma_{mat}-i\delta} \quad (4.7)$$

$$X = \frac{2\pi r}{\lambda} \quad (4.8)$$

Here, the parameters γ_{mat} and δ in Eq. (4.7) are defined in Eq. (4.2) and Eq. (4.3).

Following the working principle of an RF Yagi-Uda antenna, it is assumed that the incident field E_{in} is injected only into the resonantly driven feed at the wavelength λ . Additionally, the feed is assumed to be unaffected by other elements. Therefore the amplitude E_{rad} of the field emitted from the feed element is given by $E_F = E_{in}/(1+\gamma_{mat})$. On the other hand, each passive element is driven by the radiation from all the other elements. As a result, the radiation field of the n -th passive element $E_{rad,n}$ is given by Eq. (4.9).

$$E_{rad,n} = \frac{1}{1+\gamma_{mat,n}-i\delta_n} \{A(|X_n|)E_F + \sum_{m \neq n} A(|X_n - X_m|)E_{rad,m}\} \quad (4.9)$$

Hence, $E_{rad,n}$ is determined by solving the simultaneous equations for all the elements except for the feed.

Following the traditional way of the radio frequency study [120], directivity of an antenna is described in terms of the emission intensity of the antenna normalized by the I_F of the feed element, as given by Eq. (4.10).

$$\frac{I(\theta)}{I_F} = \left(\left| 1 + \sum_n \frac{E_{rad,n}}{E_F} \exp(-iX_n \cos(\theta)) \right| \right)^2 \quad (4.10)$$

Here θ is the angle between the antenna axis and the emission direction in the X - Y plane determined in Fig. 4.4. In the following consideration, at first, material losses γ_{mat} are not included to simplify the investigation. Later, the effect of material losses on the emission pattern of an antenna is considered.

4.2.2. Two-element antenna

Two-element antennas consisting of a feed element and a passive element is considered in this section to investigate how the functionality of the passive element depends on its detuning and the distance from the feed.

(a) Dependence of the functionality on the detuning of passive element

Figure 4.5(a) shows the calculation model. The passive element is placed at $X = -1.5$, corresponding to $r = \lambda/4$ for the working wavelength λ . The detuning of the feed δ_F is fixed to be 0. Figure 4.5(b) shows the dependence of the radiation pattern on detuning δ_P of the passive element. Figure 4.6 shows the effect of varied δ_P on the forward emission intensity $I(0)/I_F$, the backward emission intensity $I(\pi)/I_F$, and the half-power beam width (HPBW) $\theta_{1/2}$ that gives the angle between the two directions in which the radiation intensity is one-half value of the maximum.

In the range of $\delta_P > -1.0$, the passive element works as reflector, since the forward radiation ($X > 0$) is enhanced while the backward radiation is suppressed. Additionally, $\theta_{1/2}$ increases with the increase of δ_P . The maximum forward radiation is obtained with the backward radiation suppressed at $\delta_P \sim 0.3$, which corresponds to the inductive detuning ($\delta_P > 0$) as shown in Table 4.2. In this range, the forward emission is broad. In fact, $\theta_{1/2}$ is larger than 130° for $\delta_P > 0$.

In contrast, in the range of $\delta_P < -1.0$, the passive element works as director, since the backward radiation intensity $I(\pi)/I_F$ is greater than that of the forward radiation $I(0)/I_F$. However, the ratio $I(\pi)/I(0)$ can not be as large as $I(0)/I(\pi)$ obtained in the case of reflector. Director is used for sharpening the radiation. Indeed, in the range of $-2.0 < \delta_P < -1.0$, HPBW in the direction of $\theta = \pi$ is in the range of $100^\circ < \theta_{1/2} < 130^\circ$, which is narrower than that of reflector.

The function change of the passive element is considered in terms of the phase of the radiation from the passive element as shown in Fig. 4.7. The forward emission is enforced at $\delta_P \sim 1$, since the phase of $E_{rad,P}$ is shifted by -90° from the feed (advanced) which is compensated by the phase delay due to the distance of $\lambda/4$ to the feed position, resulting in the constructive interference at $\theta = 0$. In contrast, the backward emission is suppressed because the distance of $\lambda/4$ is added to the $\theta = \pi$ direction. The maximum $|E_{rad,P}|$ is obtained around $\delta_P \sim 0$. On the other hand, the passive element works as director at $\delta_P < -1$, in which the phase of $E_{rad,P}$ takes the value of $90^\circ \sim 180^\circ$. However, $|E_{rad,P}|$ becomes smaller when the phase gets close to 90° , resulting in the small ratio of $I(\pi)/I(0)$ as mentioned above.

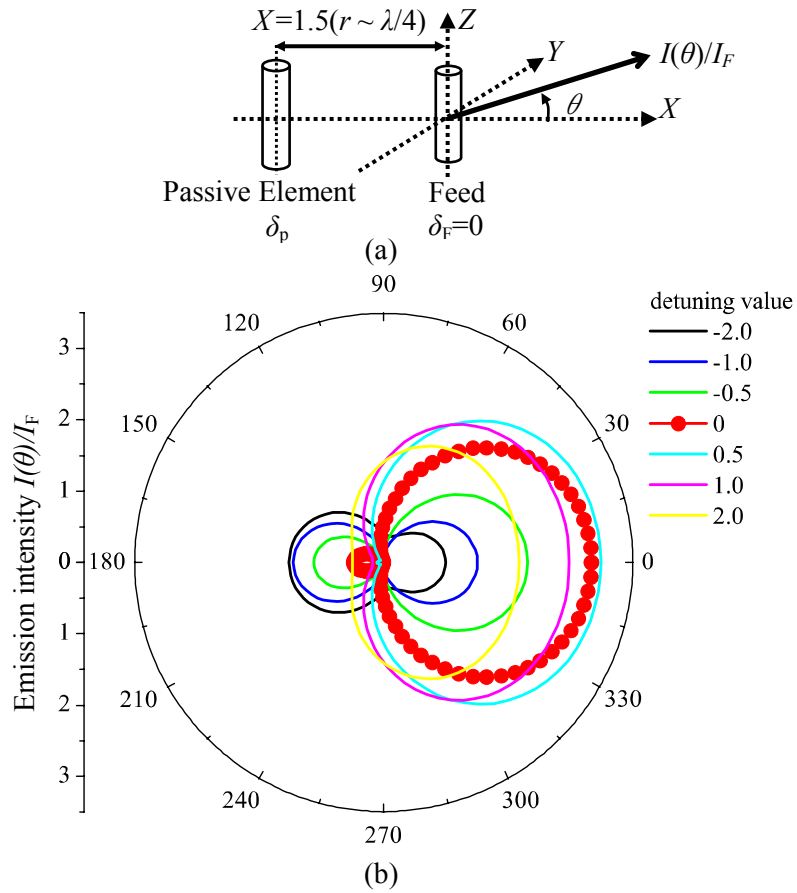


Fig. 4.5: Dependence of the radiation pattern on the passive element detuning δ_p . (a) Calculation model, (b) Radiation pattern in the X - Y plane.

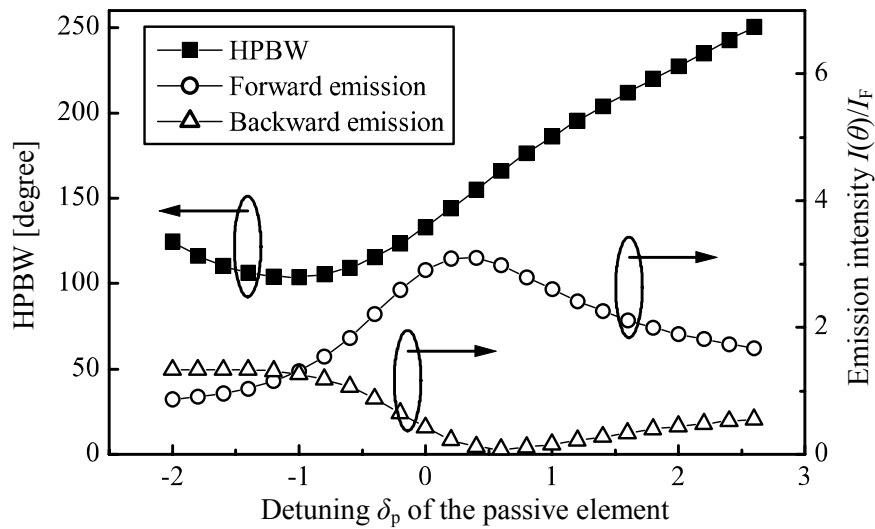


Fig. 4.6: Dependence of the 2-element antenna radiation on the passive element detuning δ_p . The solid squares(■) show the HPBW. The open circles(○) and the open triangles(△) show the emission intensity in the forward $I(0)/I_F$ and backward $I(\pi)/I_F$ directions, respectively.

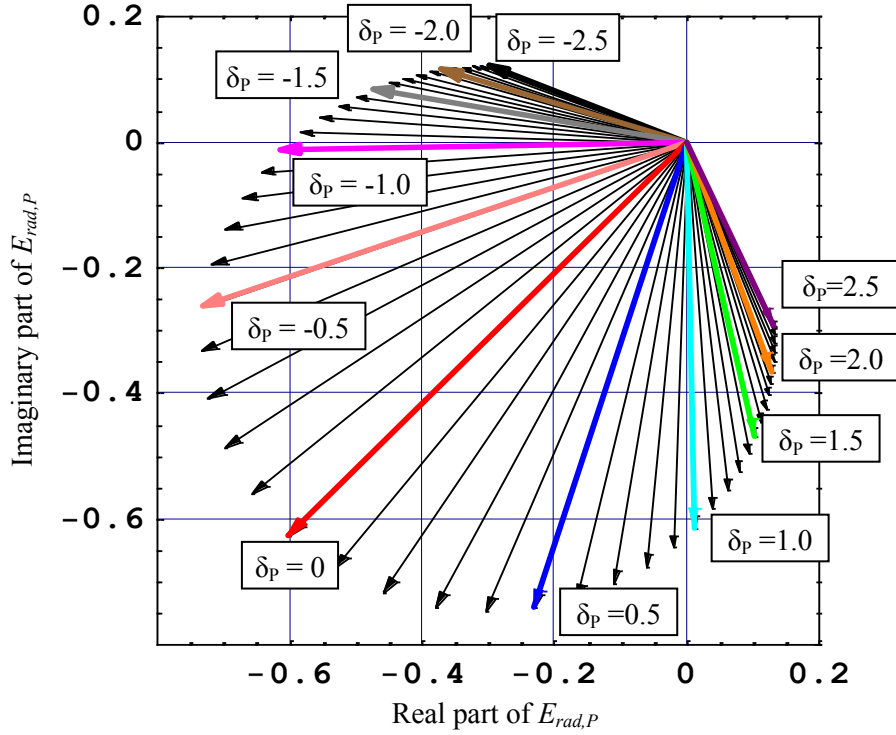


Fig. 4.7: Dependence of the radiation from the passive element on the passive element detuning δ_p . The amplitude and the phase are relative to those of the feed element.

(b) Dependence of reflector characteristics on the element distance

Figure 4.8(a) shows the calculation model of the antenna which consists of a feed placed at $X=0$ and a reflector at $X_r < 0$. The feed is the same as that shown in Fig. 4.5(a) and the reflector detuning δ_r is fixed to be zero to obtain the maximum radiation from the reflector, as shown in the previous section. Figure 4.8(b) shows the dependence of the antenna emission in the X - Y plane on the feed-reflector distance X_r . Figure 4.9 summarizes the effect of varying X_r on the forward radiation intensity $I(0)/I_F$, the backward radiation intensity $I(\pi)/I_F$, and the HPBW of radiation. In the range of $X_r < 1.0$, where the near field term $(1/X^3)$ in Eq. (4.6) is dominant, both $I(0)/I_F$ and $I(\pi)/I_F$ drastically increase with the decrease of X_r . However, the HPBW becomes broader than 150° . In contrast, the narrow HPBW less than 150° is obtained in the range of $1.0 < X_r < 2.0$, in which $I(0)/I_F$ increases gradually with the decrease of X_r , while $I(\pi)/I_F$ is suppressed. The minimum HPBW of 130° is obtained at $X_r = 1.4$. The distance corresponds to $r \sim 0.22\lambda$ which is almost the same as the optimum distance in RF Yagi-Uda antennas shown in Table 4.1. Additionally, the side lobes ($\theta = 90^\circ, 270^\circ$) are well suppressed as shown in Fig. 4.8(b).

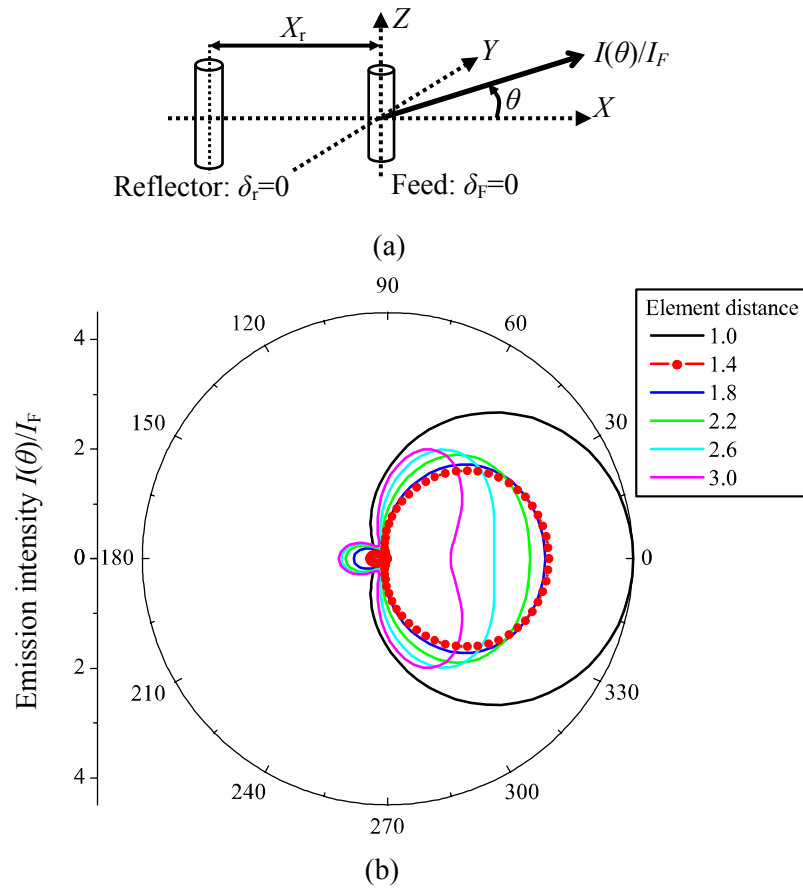


Fig. 4.8: Dependence of the antenna emission in the X - Y plane on the feed-reflector distance X_r . (a) Calculation model, (b) radiation pattern in the X - Y plane.

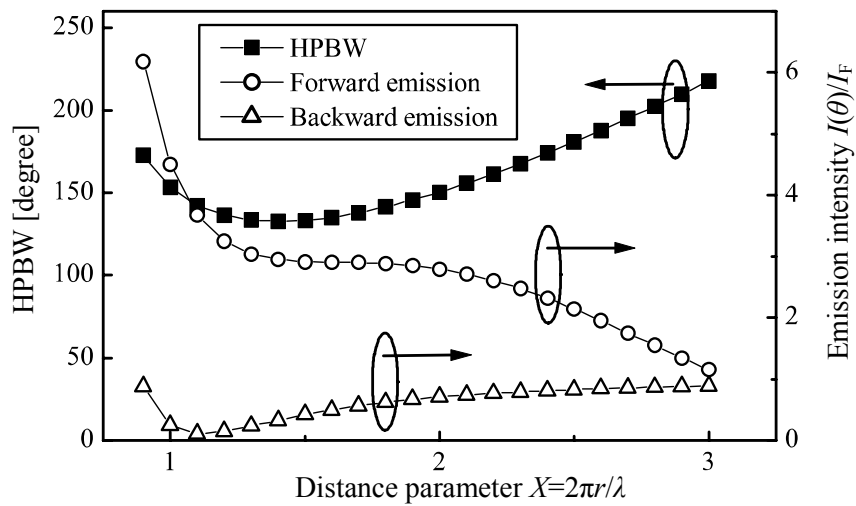


Fig. 4.9: Dependence of the antenna emission on the feed-reflector distance X_r . The solid squares(■), the open circles(○), and the open triangles(△) correspond to the HPBW, the forward emission intensity $I(0)/I_F$, and the backward emission intensity $I(\pi)/I_F$, respectively.

4.2.3. Three-element antenna

Figure 4.10 shows the calculation model of 3-element antennas. The dependence of the antenna emission on the director detuning and the director-feed distance is investigated. Following the results of the previous section, the reflector detuning δ_r is fixed to be zero and the feed-reflector distance is fixed to be $X_r=1.4$ to obtain the narrow radiation.

(a) Dependence on director detuning

The dependence of the antenna emission in the X - Y plane on the director detuning δ_d is considered. The feed-director distance is set to be $X_d=2.0(r\sim 0.3\lambda)$, following the typical design used in RF Yagi-Uda antennas shown in Table 4.1. Figure 4.11 shows the dependence of the radiation pattern on the director detuning δ_d . Figure 4.12 summarizes the effect of varying δ_d on the HPBW, and the forward $I(0)/I_F$ and the backward $I(\pi)/I_F$ radiation intensity. The HPBW is not plotted in the range of $\delta_d > 0.6$, since the side lobes (radiation to the direction of 90° and 270°) become bigger than the main lobe as shown in Fig. 4.11. In the range of $\delta_d < 0.4$ and $\delta_d > 0.8$, the forward radiation is stronger than the backward radiation, which is a desired characteristic. However, the range $\delta_d > 0.8$ is not useful since intense side lobes appear as seen in Fig. 4.11. This can be understood by looking back at Fig. 4.6 which indicates that the passive element acts as reflector in the range of $\delta_d > -1.0$. In such a case, since the feed is sandwiched between two reflectors, it is intuitively obvious that the forward and the backward radiation are suppressed and that the side lobes ($\theta=90^\circ, 270^\circ$) are enhanced.

In contrast, strong forward radiation is obtained while both the backward radiation and the side lobes are suppressed in the range of $\delta_d < -1.0$, in which the passive element acts as director as shown in Fig. 4.6. In this range, the HPBW decreases with the increase of δ_d . As a result, when δ_d is around $\delta_d = -1.0$, the directivity becomes better than in the case of a 2-element antenna shown in Fig. 4.6, since the narrow HPBW less than $\sim 90^\circ$ is obtained and side lobes are well suppressed.

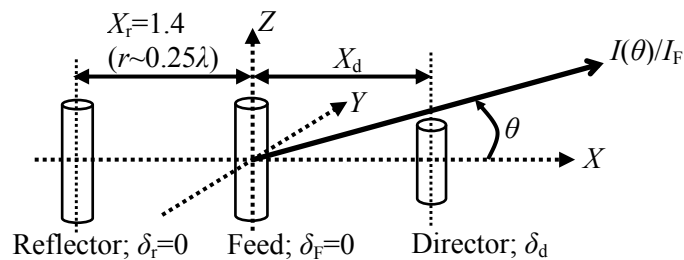


Fig. 4.10: Calculation model of 3-element antenna.

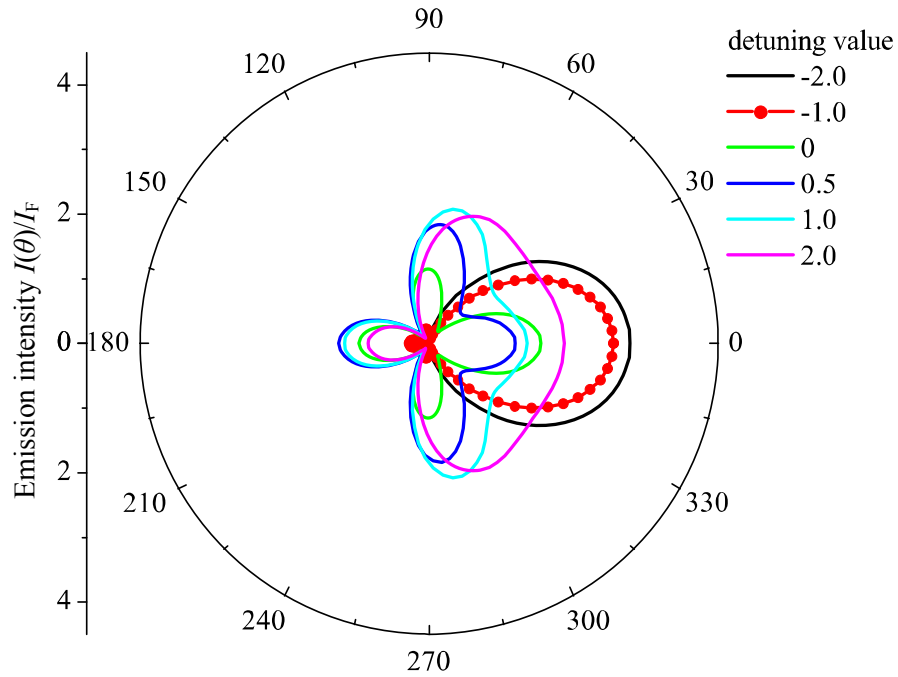


Fig. 4.11: Dependence of antenna radiation in the X - Y plane on the director detuning δ_d .

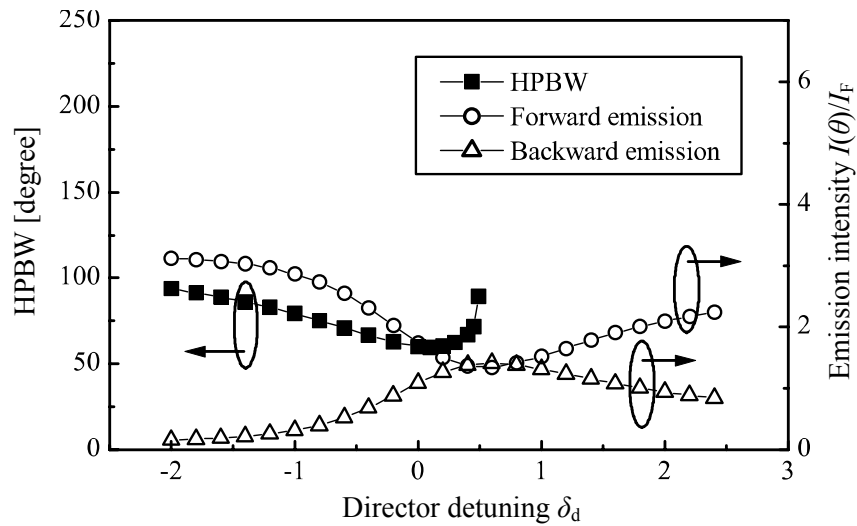


Fig. 4.12: Dependence of 3-element antenna radiation on the director detuning δ_d . The solid squares(■), the open circles(○), and the open triangles(△) correspond to the HPBW, the forward emission intensity $I(0)/I_F$, and the backward emission intensity $I(\pi)/I_F$, respectively.

(b) Dependence on Feed-Director distance

The dependence of the antenna emission in the X - Y plane on the feed-director distance X_d is considered. Following the results of the previous section, the director detuning is fixed to be $\delta_d = -1.0$. Figure 4.13 shows the dependence of the emission pattern on the feed-director distance X_d . Figure 4.14 summarizes the effects of varying X_d on the HPBW, and the forward $I(0)/I_F$ and backward $I(\pi)/I_F$ emission intensity.

In the range of $X_d < 1.4$, the forward emission and the HPBW decrease with the decrease of X_d , while the backward radiation is suppressed.

In the range of $1.4 < X_d < 4.0$, the HPBW is almost constant with $\theta_{1/2} \sim 80^\circ$, while the ratio $I(0)/I(\pi)$ increases with the increase of X_d . However, in the range of $X_d > 2.0$, the backward radiation becomes large. In addition, the side-lobes become larger gradually with the increase of X_d as shown in Fig. 4.13. As a result, the antenna shows a good directivity at $X_d \sim 2.0$, where $I(0)/I(\pi)$ is large while the side lobes are suppressed. Note that the distance of $X_d = 2.0$ ($r \sim 0.3\lambda$) is almost the same as the optimum director spacing for RF Yagi-Uda antennas shown in Table 4.1.

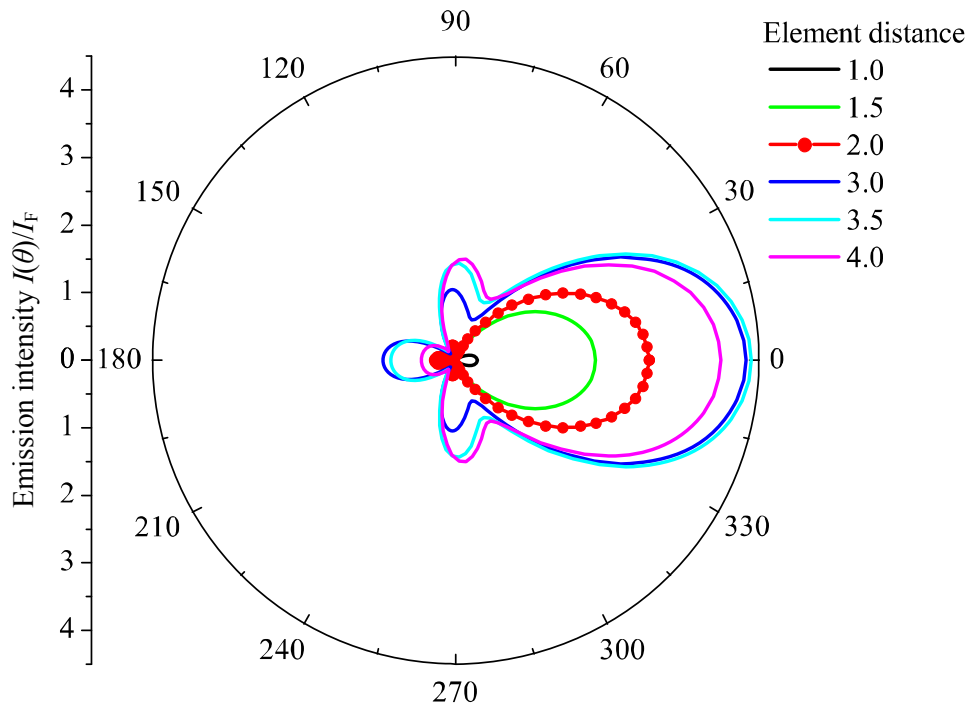


Fig. 4.13: Dependence of 3-element antenna emission in the X - Y plane on the feed-director distance X_d .

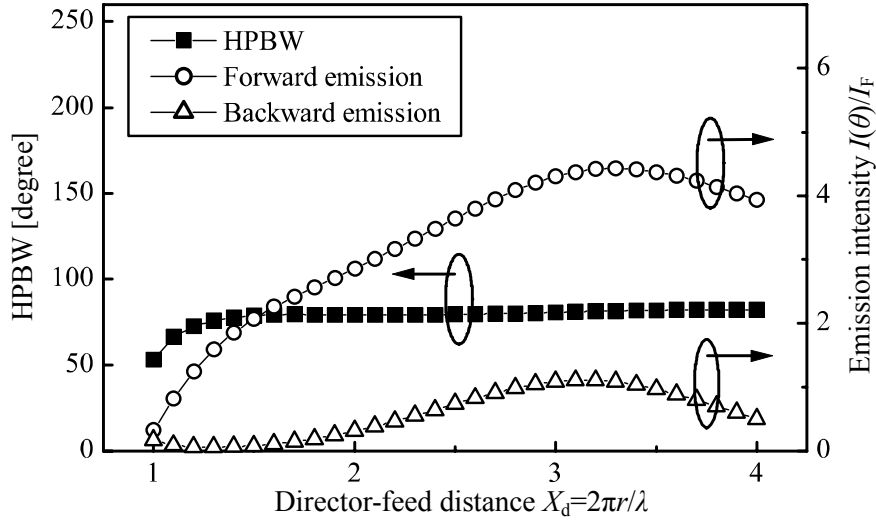


Fig. 4.14: Dependence of 3-element antenna emission on the feed-director distance X_d . Solid squares(■) show the HPBW, and open circles(○) and open triangles(△) show the intensity of the forward emission $I(0)/I_F$ and the backward emission $I(\pi)/I_F$, respectively.

4.2.4. Five-element antenna

On the basis of the results described in the previous sections, the design parameters of a five-element nano-optical Yagi-Uda antenna are investigated. Figure 4.15 shows the calculation model of the antenna consisting of a reflector at $X_r < 0$, a feed at $X=0$, and equally spaced three directors at $X_n > 0$. The director spacing is X_d . All directors are equally detuned at δ_d . The dependence of the antenna emission on δ_d and X_d is considered, with the feed-reflector distance X_r , the feed detuning δ_F , and the reflector detuning δ_r fixed to be $X_r=1.4$, $\delta_F=0$, and $\delta_r=0$, respectively to obtain the narrow radiation, as shown in Fig. 4.9.

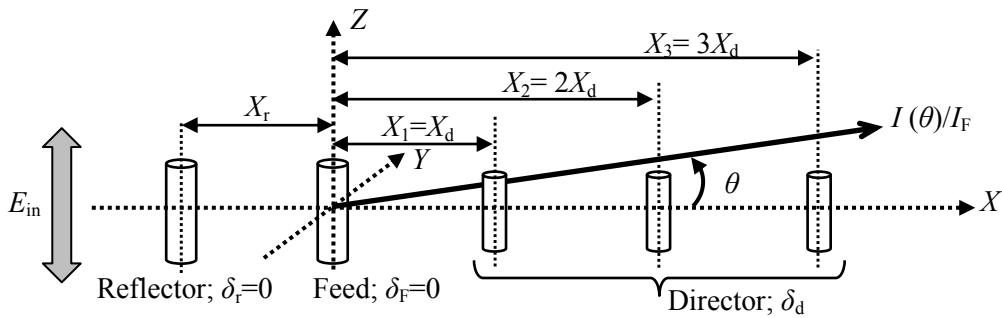


Fig. 4.15: Calculation model of 5-element Yagi-Uda antenna consisting of a reflector, a feed, and three equally spaced directors.

(a) Dependence on director spacing

Figure 4.16 shows the dependence of the antenna radiation on the director spacing X_d . On the basis of the result obtained in Section 4.2.3 (a), the director detuning δ_d is fixed to be $\delta_d = -1.0$. Figure 4.17 summarizes the effects of varying X_d on the forward emission intensity $I(0)/I_F$, the backward emission intensity $I(\pi)/I_F$, and the HPBW. Although the forward radiation is strong in the range of $X_d > 1.5$, the backward radiation becomes strong when X_d is in the range of $2.1 < X_d < 4.0$ with its maximum at $X_d \sim 3.0$. Additionally, the side-lobes are large in the range of $X_d > 3.0$, as shown in Fig. 4.16.

As a result, a good directivity of the antenna is obtained in the range of $1.5 < X_d < 2.0$, where a strong forward radiation is realized with a small HPBW of $\theta_{1/2} \sim 50^\circ$, while both the backward radiation and the side-lobes are suppressed. Note that the HPBW is smaller than that in the case of 3-element antenna shown in Section 4.2.3. This result suggests that increasing the number of directors leads to the enhancement of directivity, which is qualitatively the same phenomenon as in RF Yagi-Uda antennas [120]. The maximum $I(0)/I_F$ is obtained at $X_d \sim 1.8$, where $I(0)/I_F$ sensitively depends on X_d . Therefore the required accuracy of the director placement is higher than that of the 3-element antenna shown in Fig. 4.14.

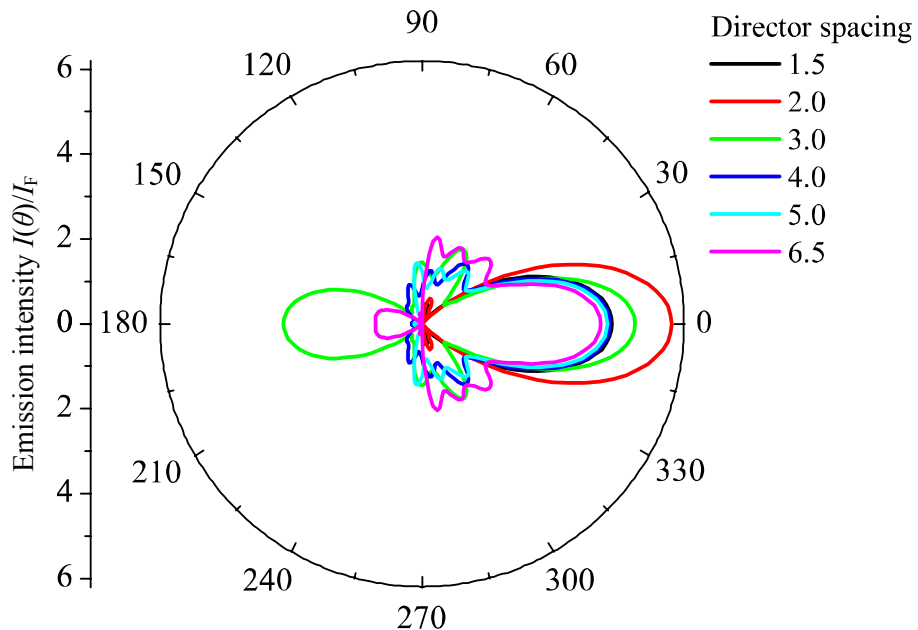


Fig. 4.16: Dependence of 5-element antenna radiation in the X - Y plane on the director spacing X_d .

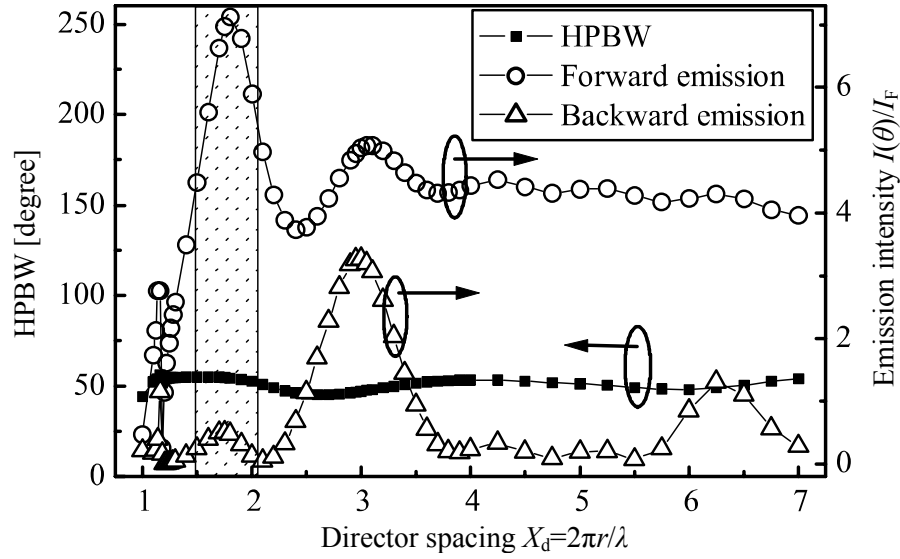


Fig. 4.17: Dependence of 5-element antenna emission in the X - Y plane on the director spacing X_d . Open circles(\circ), open triangles(Δ), and solid squares(\blacksquare) show the forward emission intensity $I(0)/I_F$, the backward emission intensity $I(\pi)/I_F$, and the HPBW, respectively. The forward radiation is strong while the backward radiation and side lobes are suppressed in the shadow area.

(b) Dependence on director detuning

Following the results of the previous section, the director spacing is fixed to be $X_d=2.0$ to obtain the strong forward emission with the backward radiation suppressed. Figure 4.18 shows the dependence of the radiation pattern on the director detuning δ_d . Figure 4.19 summarizes the effect of varying δ_d on the HPBW, the emission intensity in the directions of the forward $I(0)/I_F$ and the backward $I(\pi)/I_F$.

In the range of $\delta_d < -1.2$, the forward radiation increases with the increase of δ_d . The backward radiation is suppressed. The HPBW gradually decreases with the increase of δ_d . The maximum $I(0)/I_F$ is obtained at $\delta_d = -1.2$ with the HPBW of $\sim 60^\circ$. On the other hand, the minimum backward radiation is obtained around $\delta_d = -0.9$ where the forward radiation is still strong.

As a result, a best directivity is obtained in the range of $-1.2 < \delta_d < -0.9$, since the forward radiation is strong, and both the backward radiation and the side-lobes are well suppressed as shown in Fig. 4.18. However, the forward radiation steeply decreases with the increase of δ_d in the range of $\delta_d > -1.2$, which suggests that more precise detuning control than that in 3-element antenna is necessary to obtain strong forward radiation. Therefore, in experiment, it may be better not to choose δ_d close to -0.9 .

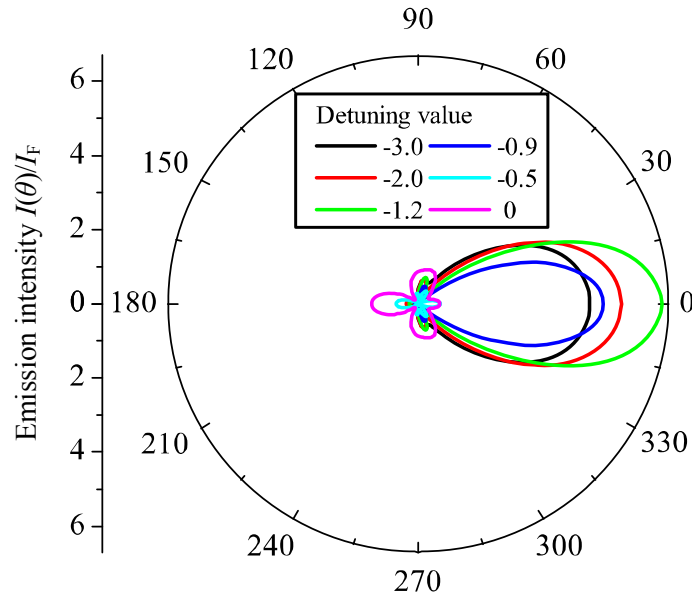


Fig. 4.18: Dependence of 5-element antenna radiation in the X - Y plane on the director detuning δ_d .

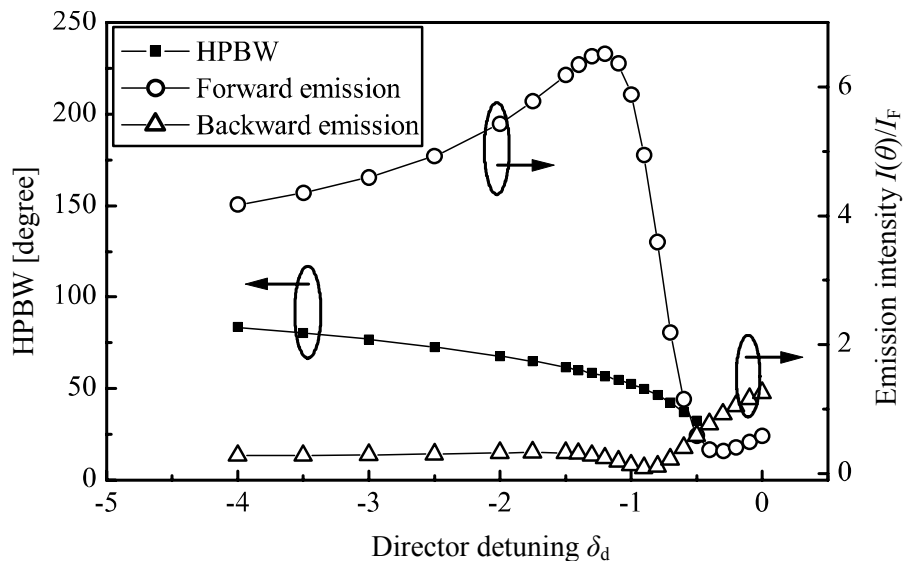


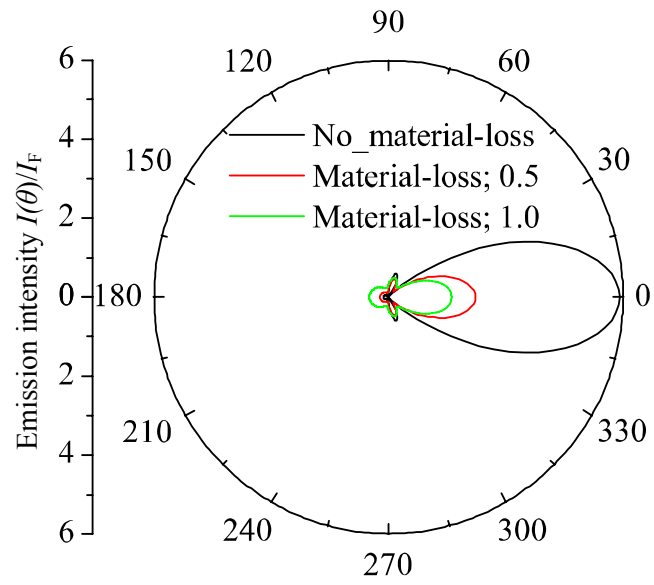
Fig. 4.19: Dependence of 5-element antenna emission in the X - Y plane on the director detuning δ_d . Open circles show the forward emission intensity $I(0)/I_F$, open triangles show the backward emission intensity $I(\pi)/I_F$, and solid dots show the HPBW.

4.2.5. Effect of material losses on the directivity

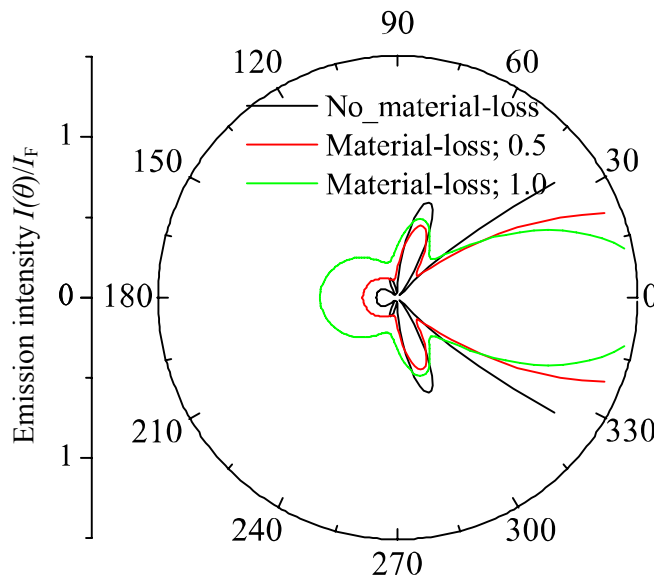
The effect of material losses on the 5-element antenna emission is considered, since the losses are not negligible in the optical response of metals as mentioned in Section 4.1.2(b). The calculation model is the same as that shown in Fig. 4.15. Following the previous results, director spacing X_d and director detuning δ_d is fixed to be $X_d=2.0$ and $\delta_d=-1.0$ to obtain the strong forward emission. In addition, the reflector detuning δ_r is fixed to be zero and the feed-reflector distance is fixed to be $X_r=1.4$ to suppress the backward radiation. The material losses γ_{mat} of all antenna elements are assumed to be the same. The radiation losses, $\gamma_{\text{mat}}=1.0$ may be a kind of limit to realize Yagi-Uda antennas relying on the coupling between the elements.

Figure 4.20 shows the effect of the material losses γ_{mat} on the antenna emission. The black line shows the results without the loss. Obviously, the radiation becomes weak owing to the presence of the material loss. In particular, the directionality $I(0)/I_F$ decreases to $\sim 1/3$ even when $\gamma_{\text{mat}}=0.5$, indicating that the interaction between elements becomes weaker than in the case without γ_{mat} . The effect of weakened interaction on the directivity can also be seen as the shallower depth of the dip ($\theta \sim \pm 45^\circ, \pm 100^\circ$). All these results come from the decrease of the radiation from each element due to the material losses.

However, the emission pattern still shows such a good directivity that the forward radiation is stronger than the backward radiation, and that the emission pattern is narrow. Therefore, it is concluded that the Yagi-Uda antenna can be constructed in optical regime as long as the material loss γ_{mat} is smaller than 1.



(a)



(b)

Fig. 4.20: Effect of the material losses on the 5-element antenna emission. (a) Overall view, (b) close-up. The black line shows the result without material losses, and the red and the green lines show the results including material losses of $\gamma_{\text{mat}}=0.5$ and $\gamma_{\text{mat}}=1.0$, respectively. The other antenna parameters are $X_r=1.4$, $\delta_r=0$, $X_d=2.0$, and $\delta_d=-1.0$.

4.3. Summary

On the basis of the coupled dipole model described in Section 2.2, a nano optical Yagi-Uda antenna has been designed in this section, utilizing the localized surface plasmon resonance in metal nanoparticles.

(a) Function and design of each element

Investigation of a two-element antenna which consists of a feed element and a passive element has confirmed the validity of the idea that the element detuning and the element distance can control the function of the passive element. Adjusting the depolarization factor N , which depends on the shape, can control the element detuning. The dipole is inductively/capacitively detuned when N is smaller/larger than $|\text{Re}(\epsilon_r - 1)|/|\epsilon_r - 1|^2$.

The reflector should be inductively driven to reflect the radiation from the feed and to suppress the backward radiation. To do so, the resonant wavelength of the reflector should be longer than that of the feed element. As a result, the aspect ratio (=major axis/minor axis) of the reflector is higher than that of the feed. The reflection has been found to be sufficiently strong within a fairly wide range of the detuning ($-1.0 < \delta_r$). A relatively narrow radiation is obtained when the feed-reflector spacing is around $r \sim 0.22\lambda$ ($X \sim 1.4$), though the dependence of the antenna radiation on the spacing is weak.

On the other hand, the director should be capacitively driven by the radiation field from the feed to sharpen the emission of the Yagi-Uda antenna. To do so, the resonant wavelength of the director should be shorter than that of the feed. As a result, the aspect ratio of director should be lower than that of the feed.

(b) Required accuracy of director placement and detuning

Since multiple directors are required to enhance the forward emission of the Yagi-Uda antenna, the antenna characteristics become sensitive to the director parameter. Indeed, the 3-element and 5-element Yagi-Uda antennas show the strong forward emission with both the backward radiation and the sidelobes well suppressed for the director spacing of $X_d = 2.0$ and $X_d = 1.8$, respectively. In addition, the forward emission of the 5-element antenna depends more strongly on X_d than that of the 3-element antenna does. This result suggests that the director should carefully be placed in the 5-element antenna. Fortunately, however, the use of electron-beam lithography can perform the fairly precise positioning of the antenna element.

The forward radiation also depends on the director detuning δ_d in the antennas with larger number of directors. In particular, the forward radiation decreases steeply when $\delta_d > -1$ in the case of 5-element antenna. Contrary to the case of controlling the element position, precise control of detuning is not an easy task since the shape of the nanoparticle determines the detuning. Precise control of the shape in nanoscale is difficult. Therefore, practically, the detuning parameter δ_d should be chosen not to be too close to $\delta_d = -1$ where the function of the antenna element drastically changes. Accordingly, in the case of 5-element antenna, director detuning in the range of $-2 < \delta_d < -1$ may be an appropriate choice.

As a consequence, for example, appropriate directivity ($I(0)/I_F = 6.52$, $I(\pi)/I_F = 0.24$, HPBW = 56.7°) has been obtained for element parameters of reflector ($\delta_r = 0$, $X_r = 1.4$), feed ($\delta_f = 0$), and director ($\delta_d = -1.2$, $X_d = 2.0$). The emission pattern is shown as a green line in Fig. 4.18.

(c) Effect of material losses

It has been confirmed that even if the material losses are comparable to the radiation losses, the 5-element Yagi-Uda antenna shows directivity. However, due to the material losses, the radiation from the antenna element decreases. As a result, the forward radiation decreases to about one third of that without the material losses. Additionally, the depth of the dips in the emission pattern becomes shallower than that without the material losses. Therefore, the material losses should be smaller than the radiation losses as much as possible to realize a good Yagi-Uda antenna with strong directivity.

Although the material losses of silver are less than those of gold, gold has been chosen as the antenna elements in this work. That is because silver is so easily oxidized that it is more difficult to handle.

The proper size of gold nanoparticles to be used as antenna elements has been estimated by relating the material losses to the aspect ratio of the nanoparticles. As a result, the gold nanoparticles with the length longer than 50 nm, with the fixed width and the thickness of 50 nm have been found to have the material losses less than 0.5 relative to the radiation loss.

5. Nano-optical Yagi-Uda antenna: Experiment

The realizability of directional control of light by a nano-optical Yagi-Uda antenna consisting of gold nanoparticles was experimentally examined as follows [123]. On the basis of the design obtained in Chapter 4, antennas were fabricated by means of electron beam lithography (EBL) and gold lift-off process. First, the radiation pattern of the single element antennas was measured to confirm the validity of driving method of the antenna and the adequacy of the measurement set-up. Second, the radiation pattern of a 2-element antenna consisting of a feed and a reflector/director was measured to confirm the idea that the element detuning can control the function of the passive element. After that, the radiation pattern of a 5-element Yagi-Uda antenna was measured to demonstrate the directional control of light.

5.1. Nano pattern fabrication

Table 5.1 shows the main specifications of the EBL equipment used in this work. The realizable minimum width of the exposed patterns is around 50 nm. The typical exposure conditions of the EBL used in this work were a beam current of 40 pA and dose of 250-390 $\mu\text{C}/\text{cm}^2$.

Figure 5.1 shows the sample fabrication process. The details are given in Appendix II. The antennas were fabricated on a glass substrate ($n=1.51$). To put the antenna in a uniform medium for ensuring the interaction between the elements, the antenna was sandwiched between sputter-deposited SiO_x films of refractive index $n\sim 1.44$. To obtain fine resist patterns with reverse-tapered cross-section, which is appropriate for the subsequent lift-off process, the bi-layer resist process was applied in this work [128, 129]. The upper and lower layer of the bi-layer resist was ZEP-520A7 (Zeon Corporation) and PMMA (950PMMA-A2, MicroChem Corp.), respectively. Additionally, a conductive layer (ESPACER 300Z Showa Denko K.K.) was spin-coated on the ZEP-520A7 layer to avoid the charge-up during the electron beam exposure.

After the exposure, at first, the ESPACER layer was removed by a dip-treatment in de-ionized water. After the development of the ZEP-520A7 layer, dip treatment was applied with rinse solution. At the same time, PMMA layer was etched by the rinse solution [129]. After that, the sample was rinsed with the de-ionized water, which was subsequently removed by a N_2 -blow. Next, a gold film was deposited in a vacuum evaporator with a rate of 0.1 nm/sec. By means of a lift-off process, the gold film was removed, leaving the antenna patterns. Finally, SiO_x film was deposited on the sample

to cover the antenna pattern. Figure 5.2 shows a SEM image of the fabricated gold nano pattern. The nano pattern with the width of 52 nm and the length of 68 nm was obtained.

Table 5.1: Main specifications of the electron beam lithography equipment (ELIONIX Co.; ELS-3700) used in this work.

Electron Gun Type	Max acceleration voltage	Minimum beam radius	Minimum line width
LaB ₆	30 kV	6 nm	~50 nm

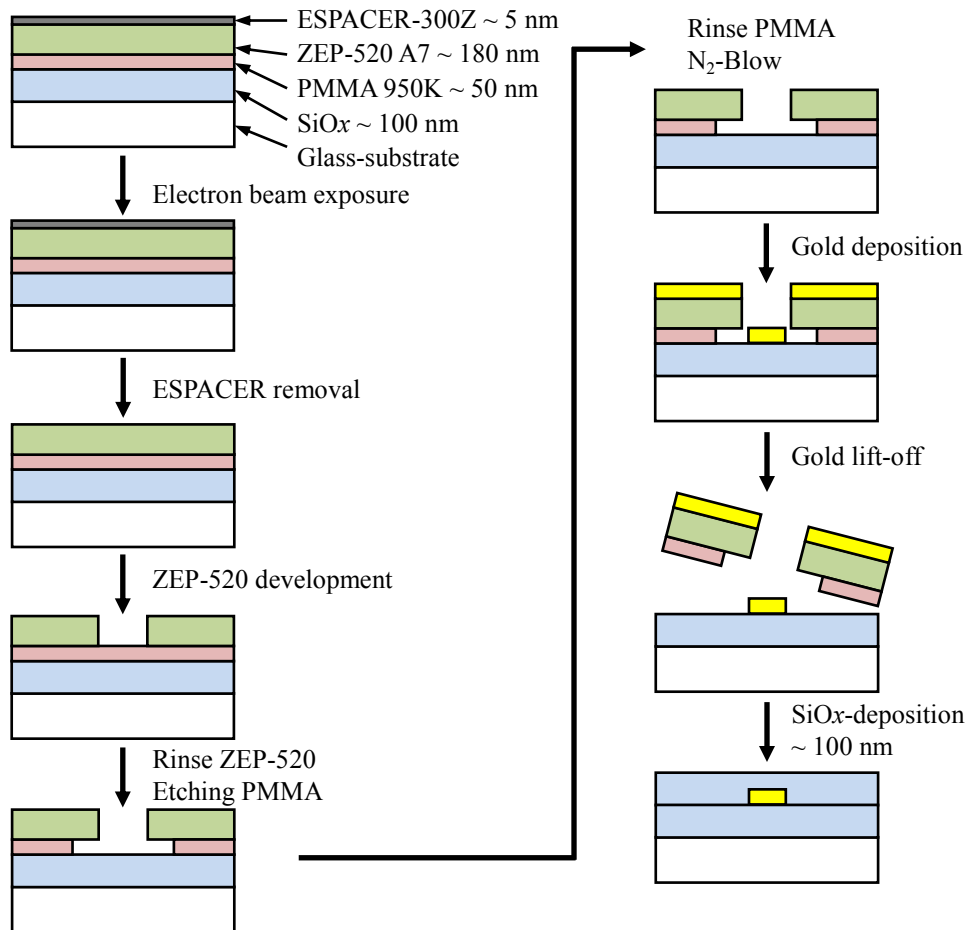


Fig. 5.1: The flow chart of the sample fabrication process by the electron beam lithography with bi-layer resist process [128, 129], and subsequent gold lift-off process.



Fig. 5.2: An example of the SEM image of the gold nano pattern.

5.2. Driving method of antenna

The antenna design obtained in Chapter 4 assumed that the incident power would be injected only into the feed element. In order to realize the assumed situation, the polarization dependence of the nanorod response was used in this work [123]. Figure 5.3 shows the top view of the antenna layout. The feed element was tilted by 45 degrees towards the antenna axis, and driven by the incident field polarized parallel to the antenna axis (X). In principle, owing to this diagonal alignment, the feed converts a part of the incident field into the one polarized along the major axis (Y) of the passive elements. As a result, the converted field drives the passive elements. Since the major axes of the passive elements are parallel with each other, all passive elements interact well with each other. Thus, the antenna is driven only through the feed element. In the measurement, only the Y -polarized radiation was detected.

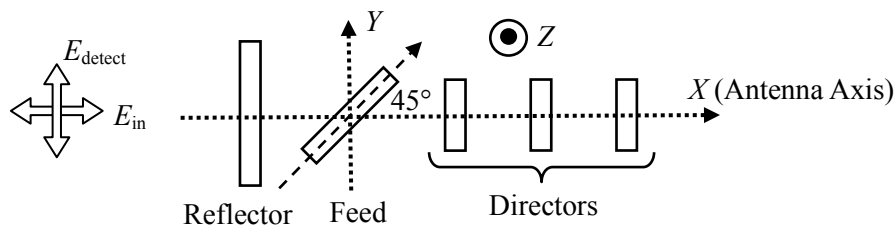


Fig. 5.3: Top view of a 5-element nano optical Yagi-Uda antenna.

When the feed element was arranged to be tilted, the edge of the feed became close to the neighboring element as shown in Fig. 5.3. The effect of it on the directivity of the antenna emission was examined by a finite difference time domain (FDTD) method using commercial software (Fullwave, Rsoft. Co.). Figure 5.4(a) shows the calculation model of a feed-reflector antenna. The feed was modeled by a rectangular with the width and thickness of 50 nm, capped by a half circle with the radius of 25 nm. The total length of the feed is 106 nm. The shape of the reflector was the same as that of the feed, except that the length was set to be 125 nm, following the prediction given in the

previous chapter. Since, the feed was tilted by 45 degrees, the distance between the reflector and the edge of the feed was only ~ 55.2 nm. In the calculation, the antenna was driven by the light polarized parallel to the antenna axis (X), while the field parallel to the Y -axis was detected in the X - Z plane. The permittivity of gold was expressed by the sum of the Drude model and the Lorentz model, and the surrounding medium was assumed to be uniform to simplify the calculation.

The open dots (\circ) in Fig. 5.4(b) show the radiation pattern of the antenna without the reflector(feed-only) in the X - Z plane. An isotropic radiation was obtained as expected. The solid dots (\bullet) in Fig. 5.4(b) show the radiation pattern of the feed-reflector antenna. As predicted by the coupled dipole model in Section 4.2.2, the reflector gave the forward emission, and suppressed the backward radiation. This result indicates that the proximity effect is negligible in the present design of the antenna.

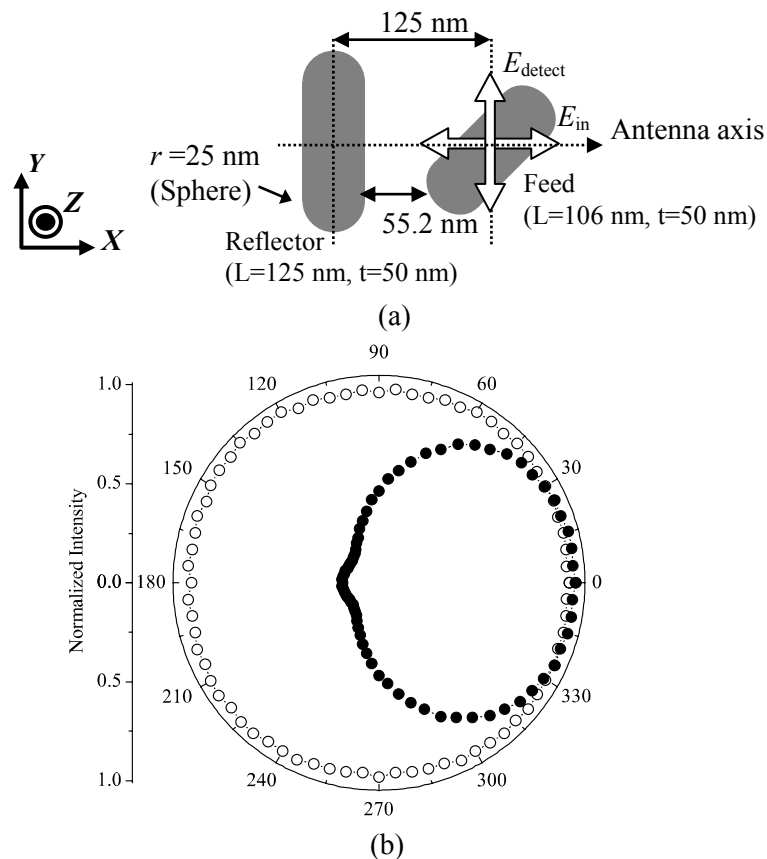


Fig. 5.4: Radiation pattern of the feed-reflector antenna, calculated by an FDTD method. (a): Schematic view of the feed-reflector antenna: polarization direction of the incident field E_{in} and the detection field E_{detect} are orthogonal with each other. (b): Open dots and solid dots show the radiation patterns of only the tilted-feed and the feed-reflector antenna in the X - Z plane, respectively.

5.3. Measurement set-up

5.3.1. Evaluation of resonant wavelength

The resonant wavelength of the localized surface plasmon resonance of the fabricated nano patterns was evaluated by measuring the transmission spectra. Figure 5.5 shows the measurement set-up used in this work. The light source was a halogen lamp (PHILIPS, 50 W). The FWHM of the focus spot size at the sample position was measured to be about 30 μm with a knife-edge method. The polarizers controlled the polarization of the incident and the transmitted light.

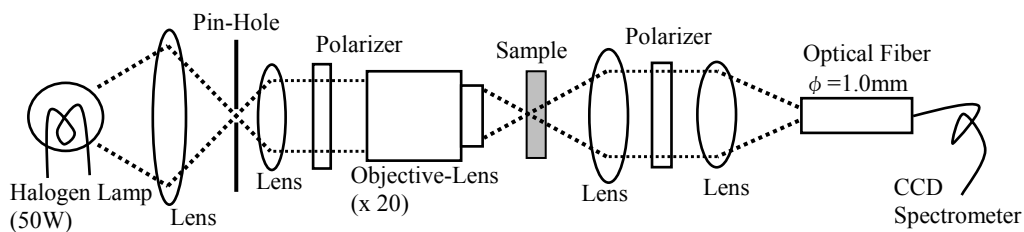
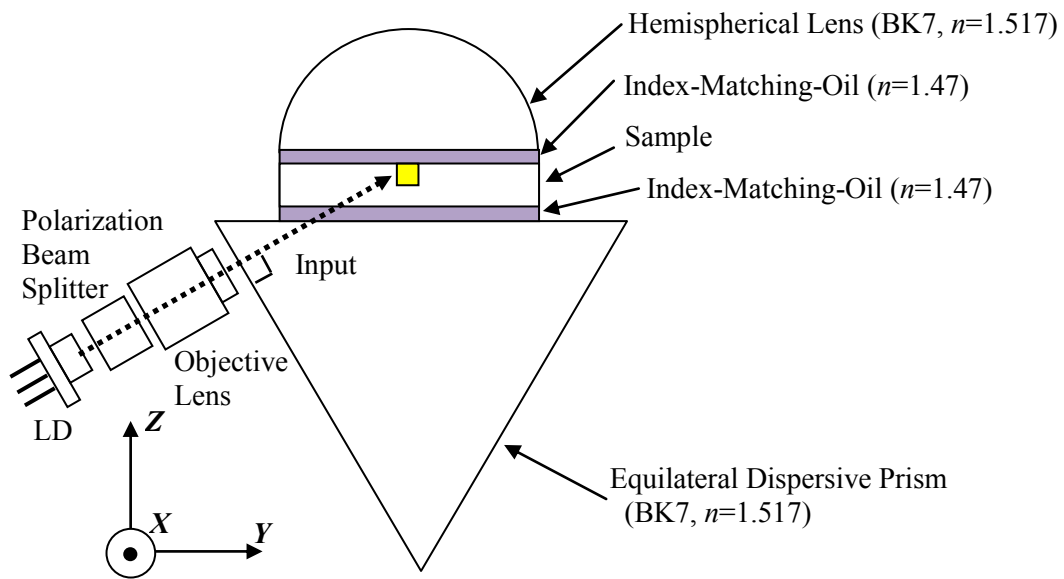


Fig. 5.5: Schematic diagram of the transmission spectroscopy set-up.

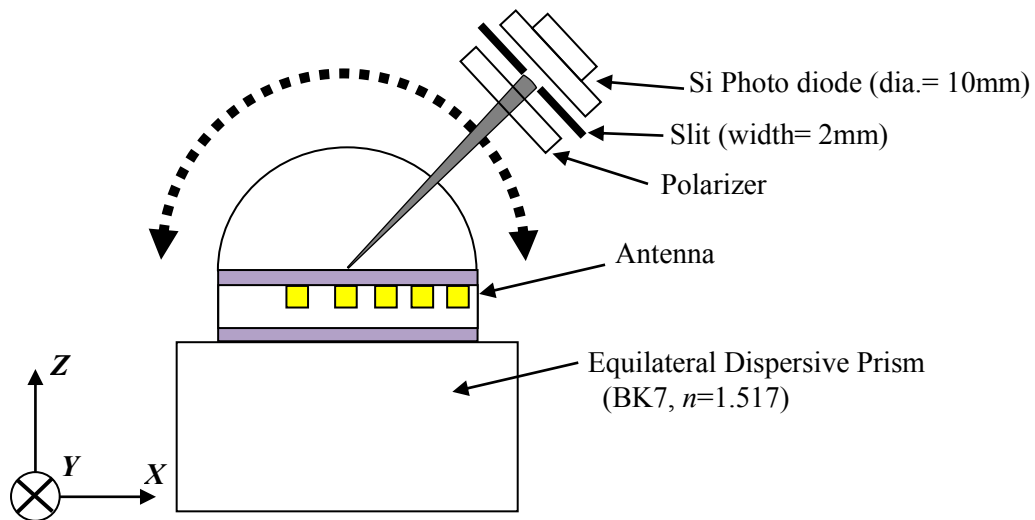
5.3.2. Measurement of radiation pattern

Figure 5.6 shows the set-up for measuring the radiation pattern of the optical antennas. The sample was set on an equilateral dispersive prism (BK7, $n=1.517$), and covered by a hemispherical lens (radius=5 mm, BK7, $n=1.517$). An index-matching oil (Cargille Labs, Type FF, $n=1.479$) was used at the interfaces. The antennas were driven by a laser diode (10 mW) at 662 nm through a polarizer. The focus size was 15 μm by 36 μm , measured with a knife-edge method without the prism. The power radiated from the antennas was detected in the X - Z plane, orthogonal to the substrate including the antenna axis, by a silicon photodiode through a polarizer. A slit with the width of 2 mm was set in front of the silicon photodiode. Since the distance between the antenna and the slit was 40 mm, the angular resolution was 2.86 degrees.

Figure 5.7 shows the photos of the measurement set-up. To avoid the blocking of the radiation from the antenna, the fixture of the sample holding was specially designed as shown in Fig. 5.7(c). Thus this measurement set-up was able to measure the radiation pattern of the antenna from 0 to 180 degrees.



(a)



(b)

Fig. 5.6: Set-up for the measurement of the radiation pattern from the optical antennas: (a) Side-view, (b) Front-view. The detector was scanned rotationally around the antenna, in the X - Z plane.

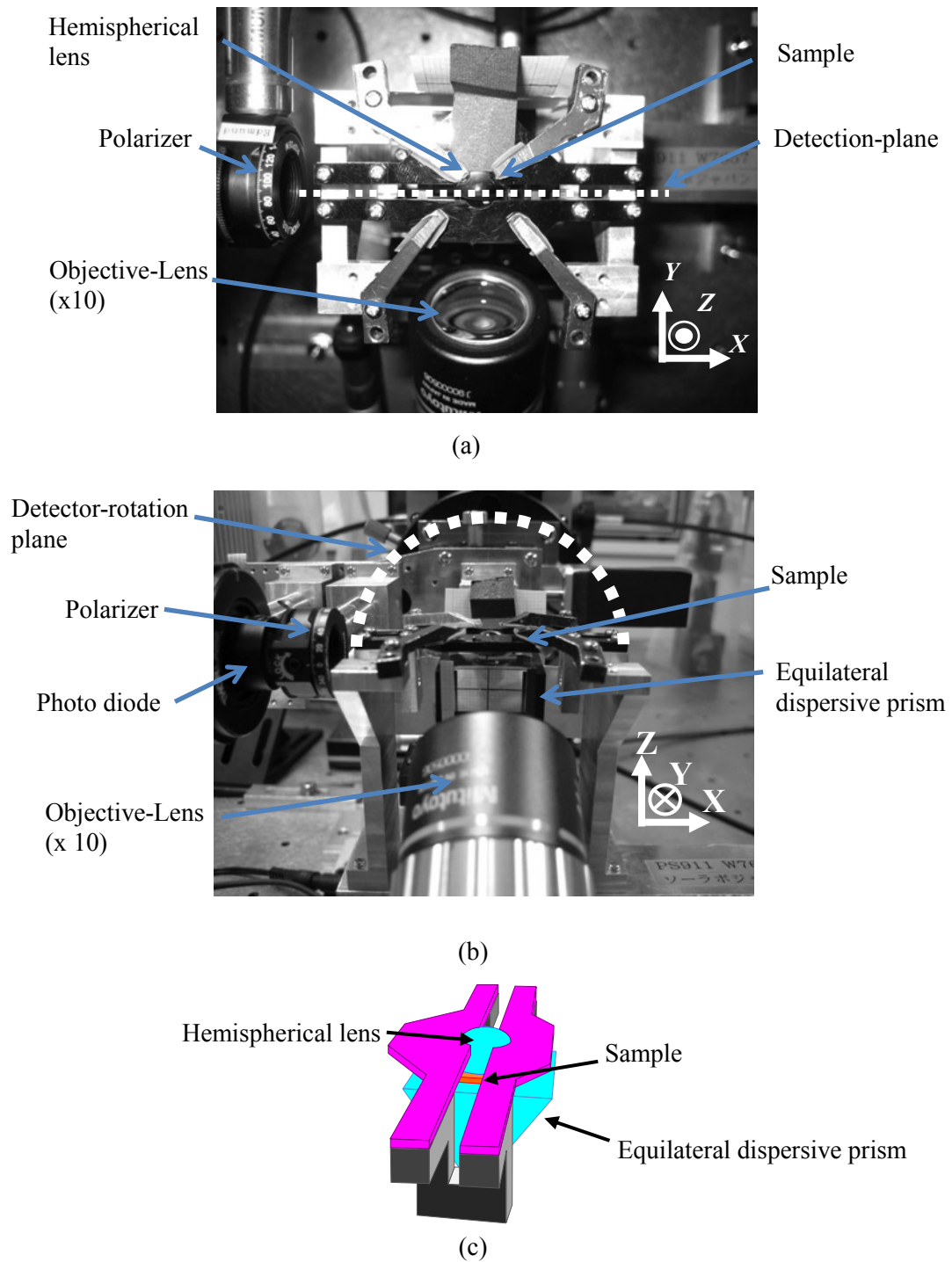


Fig. 5.7: Photos of the radiation pattern measurement set-up; (a) top view, (b) front view of the sample holder, and (c) the schematic view of the fixture of the sample holding. The detector was moved along the white-dots in the X - Z plane. Since the detection plane, which was parallel to the antenna axis, had no blocking, the detector was able to measure the radiation pattern of the antennas from 0 to 180 degrees. A polarizer was set in front of the photo diode to choose the polarization direction of the detection field.

5.4. Demonstration of optical Yagi-Uda antenna

5.4.1. Antenna design & layout

Figure 5.8 shows the design of the antennas fabricated in this work. The working wavelength of the antennas in the medium (SiO_x , $n \sim 1.44$) was designed to be $\lambda_{\text{med}} \sim 459.7 \text{ nm}$ ($=662/1.44$). The function of the antenna element was controlled by adjusting the aspect ratio (= major-axis/minor-axis) of the element. In order to confirm that the reflector and the director have the desired function, 2-element antennas composed of a feed and a reflector/director with the element distance of 125 nm ($\sim 0.27\lambda_{\text{med}}$, $X=1.70$) were fabricated. In the case of the 5-element antenna, the feed-reflector distance was set to be 125 nm ($\sim 0.27\lambda_{\text{med}}$) and the director spacing was set to be 150 nm ($\sim 0.33\lambda_{\text{med}}$, $X=2.07$).

In order to enhance the detected power, antennas were linearly arrayed. Figure 5.9 shows the relation between the arrayed antenna and the spot size of the incident light. The pitch perpendicular to the antenna axis was 550 nm designed to drive the antenna in almost the same phase. Since about 20 antennas were driven, the emission power would be 400 times as much as that from a single antenna by the interference effect.

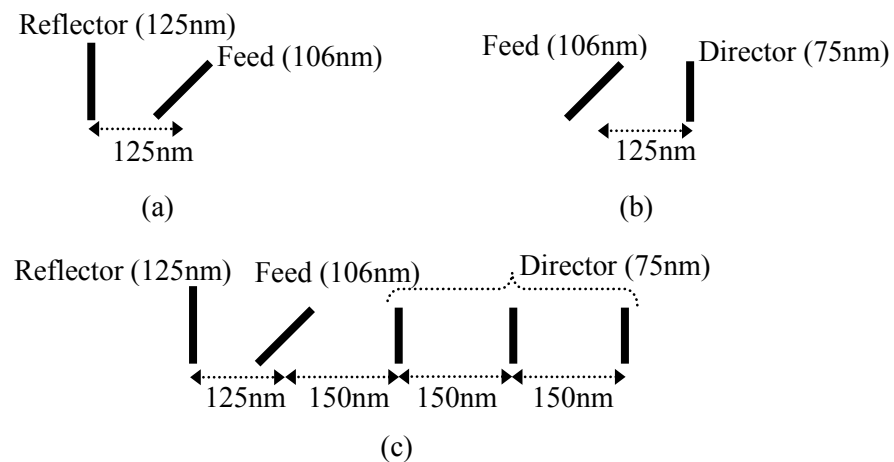


Fig. 5.8: Design of the antennas in this work. Parenthetic numbers are the designed length of the element. (a), Feed-Reflector antenna. (b), Feed-Director antenna. (c), 5-element antenna.

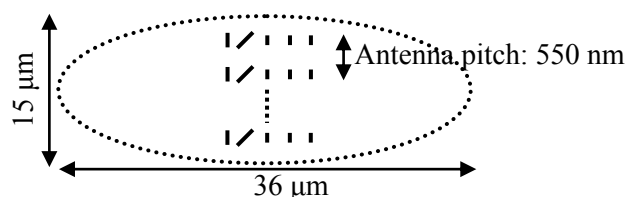


Fig. 5.9: Relation between the arrayed antenna and the spot size of the incident light.

5.4.2. Resonant wavelength of each element

Figure 5.10 shows the nano patterns used to measure the resonant wavelength of the antenna element. These patterns and the Yagi-Uda antennas were fabricated on the same substrate at the same time to reduce the effect of the difference in the fabrication condition. The overall sample layout is given in Appendix III. The distance between the nano patterns was fixed to be 800 nm, which corresponded to the minimum density necessary for a reliable measurement in the set-up shown in Fig. 5.5, while the effect of the interaction between the particles on the resonance was suppressed as discussed in Chapter 3.

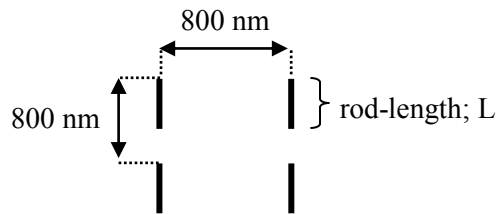


Fig. 5.10: Nano patterns for estimating the resonant wavelength of the element used in the antennas. The patterns were fabricated with an interval of 800 nm in a 50 μm square.

(a) Resonant wavelength of each element

Figure 5.11 shows the SEM-image of each antenna element. The measured element lengths were about 58 nm, 75 nm, and 108 nm for the director, feed, and reflector, respectively. The difference from the design, shown in Fig. 5.8, came from the difficulty of fabrication. Figure 5.12 shows the transmission spectra in the case of the incident field (a) polarized parallel or (b) polarized perpendicular to the longer axis of the element. The resonant wavelengths for the longer axis were found to be 655 nm, 770 nm, and 610 nm for the feed, reflector, and director, respectively. On the other hand, the resonant wavelengths corresponding to the shorter axis of the nanorod were all ~ 600 nm.

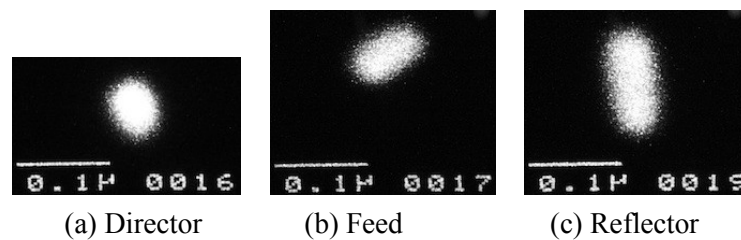


Fig. 5.11: SEM-image of each element.

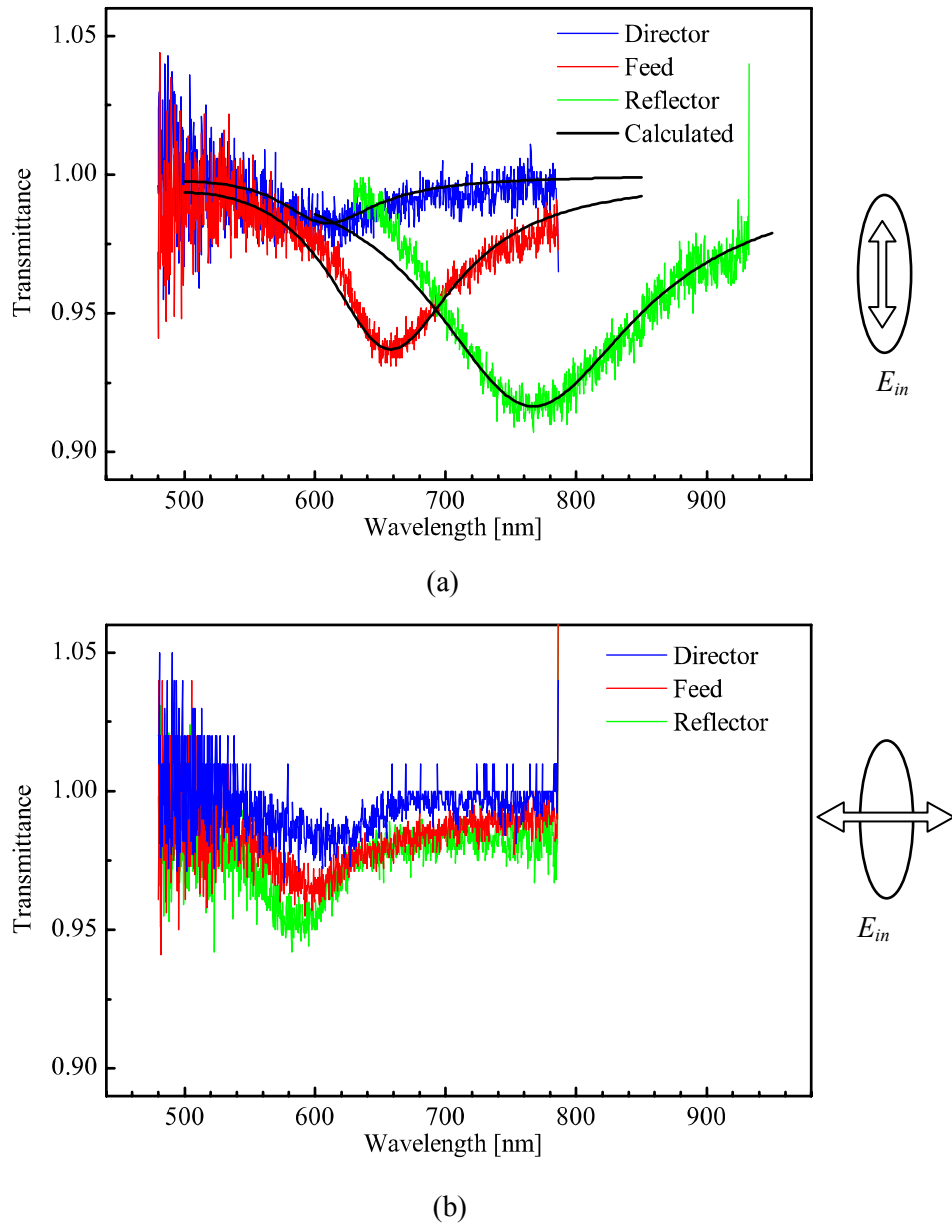


Fig. 5.12: Transmission spectra of each element used in the antennas. (a) Incident field was polarized parallel to the longer axis of the element. The black solid lines are the result of the dipole model fitting based on the Eq. (5.1). (b) Incident field was polarized parallel to the shorter axis of the element.

(b) Estimation of the dipole parameters

In order to compare the experimental result with the prediction based on the coupled dipole model, parameters of each antenna element were estimated.

According to the Eq. (2.36), the polarizability α of the nanoparticle can be expressed in terms of the volume V , the depolarization factor N , and the dielectric constant ϵ_r of the particle material relative to the surrounding medium ($\epsilon_r = \epsilon_p / \epsilon_{med}$) as follows.

$$\alpha = \frac{V}{\frac{1}{\epsilon_r - 1} + N - i \frac{4\pi^2 V}{3\lambda^3}} \quad (5.1)$$

The imaginary part of α describes the extinction by the nanoparticle [37]. Therefore, the parameters of the fabricated element can be evaluated by fitting the imaginary part of Eq. (5.1) with the measured transmission spectra (extinction spectra) of the element. The black solid lines in Fig. 5.12 (a) show the results of the fitting. In that case, the surrounding medium was assumed to be SiOx ($\epsilon_{med} \sim 2.1$), and ϵ_p was given by the literature [38]. The obtained fitting parameters are listed in Table 5.2. The validity of this analytical approach is ensured by the fact that the fitting value of the volume was almost the same as the designed value.

On the other hand, the material loss γ of each element was estimated by substituting the volume V into Eq. (2.38) at the wavelength of 662 nm (vacuum). The evaluated material losses were less than 0.5 as shown in Table 5.2. Since an antenna could show the directional emission when the material losses were less than $\gamma = 1.0$ as predicted in Section 4.2.5, the fabricated antennas should be capable of showing the desired directivity. Additionally, the element detuning δ at 662 nm was estimated by substituting the obtained N and V into Eq. (2.39).

Table 5.2: The parameters of the antenna element estimated by fitting the transmission spectra shown in Fig. 5.12 (a) with the imaginary part of the polarizability given by Eq. (5.1). The loss parameter γ and the element detuning δ were estimated at the wavelength of 662 nm (vacuum), embedded in SiOx ($\epsilon_{med} \sim 2.1$).

	Resonant wavelength [nm]	Depolarization Factor N	Volume of nanoparticle V [m ³] (Designed value)	Loss parameter γ	Element detuning δ
Reflector	770	0.09	2.5×10^{-22} (3.12×10^{-22})	0.285	1.09
Feed	655	0.135	1.88×10^{-22} (2.65×10^{-22})	0.380	-0.32
Director	610	0.173	1.63×10^{-22} (1.88×10^{-22})	0.438	-2.09

5.4.3. Directionality

5.4.3.1. Feed element

The validity of driving method of the antenna, namely the tilting of the feed element, described in Section 5.2 was confirmed by investigating the radiation pattern of the feed element having neither reflector nor director.

Figure 5.13 shows a SEM image of the feed and the radiation pattern. The polarization of the incident field E_{in} was tilted by 45° from the major axis of the feed, and the polarization of the detected field E_{detect} was perpendicular to that of E_{in} . The measured results (solid circles) were normalized by the maximum intensity. The radiation pattern is nearly symmetric around the normal to the surface, indicating that the tilted feed generates the dipolar radiation with the polarization orthogonal to the incident field. The result also indicates that the set-up is appropriate for the measurement of directivity of the antenna emission.

On the other hand, the intensity diminishes at the angles below 20° and above 160° . This result indicates the presence of a mismatch in the indices of refraction above and below the feed. The open circles represent the radiation pattern of a single dipole placed at an interface between the mediums, whose refractive index above the dipole ($0^\circ\sim 180^\circ$) is lower than that below the dipole, calculated by the method of reciprocity [130]. The measured radiation pattern is similar to the prediction for the refractive index ratio of 1.05, which corresponds to the refractive index ratio of the substrate ($n = 1.51$) to the SiO_x layer ($n = 1.44$). The comparison suggests that the SiO_x layer between the antenna and the glass substrate is not affecting the radiation. To clarify the reason, it is necessary to investigate the radiation pattern from dipoles embedded in such a multi-layer structure.

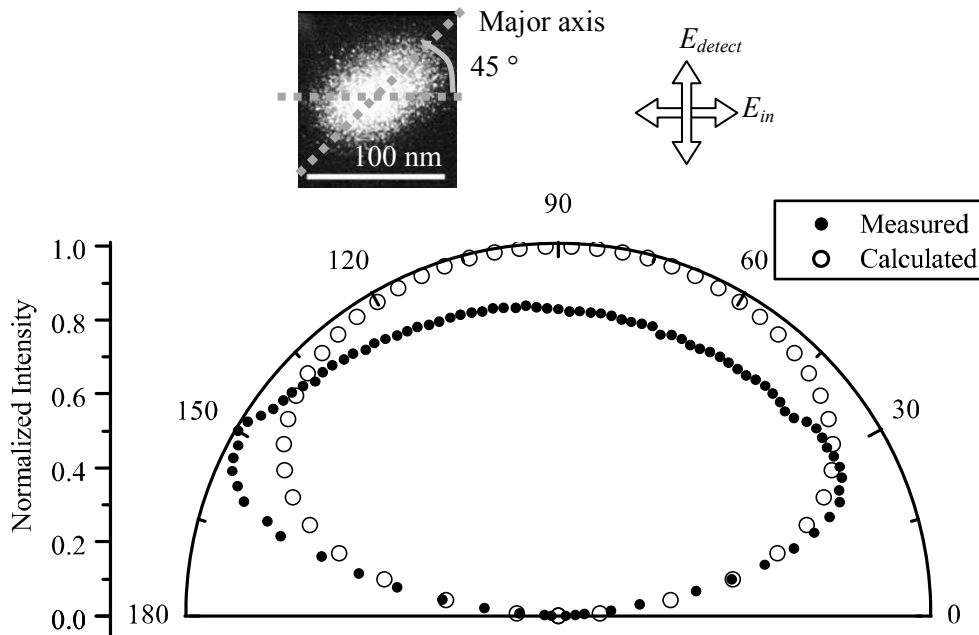


Fig. 5.13: Radiation pattern of the arrayed feed element. The inset shows the SEM image of the feed. The solid and open circles are the measured results and the prediction, respectively.

5.4.3.2. 2-element antenna

(a) Feed with a reflector

Figure 5.14 shows a SEM image and the radiation pattern of the feed-reflector antenna. The measured results are plotted by the solid dots. The prediction based on the coupled dipole model is plotted by the open circles. The radiation patterns were normalized by the maximum value. In the prediction, the dipole parameters listed in Table 5.2 were used, but the refractive index difference between the layers above and below the antenna was not taken into account. The experimental results and the prediction agree well with each other except in the angle region close to the interface. The radiation in the backward direction is suppressed quite well, indicating that the reflector works as expected. The diminishing intensity in the measured emission pattern around 0° and 180° can be explained in terms of the difference in the refractive index between the SiO_x film and the substrate as mentioned in Section 5.4.3.1.

In particular, the angle and the depth of the dip observed around 135° in the measured radiation pattern agree well to the prediction. In principle, the difference in phase and intensity of the emission between the feed and the reflector decides the angle and the depth of the dip. Therefore, it is concluded that the reflector has a desired function as predicted in Section 4.2.2.

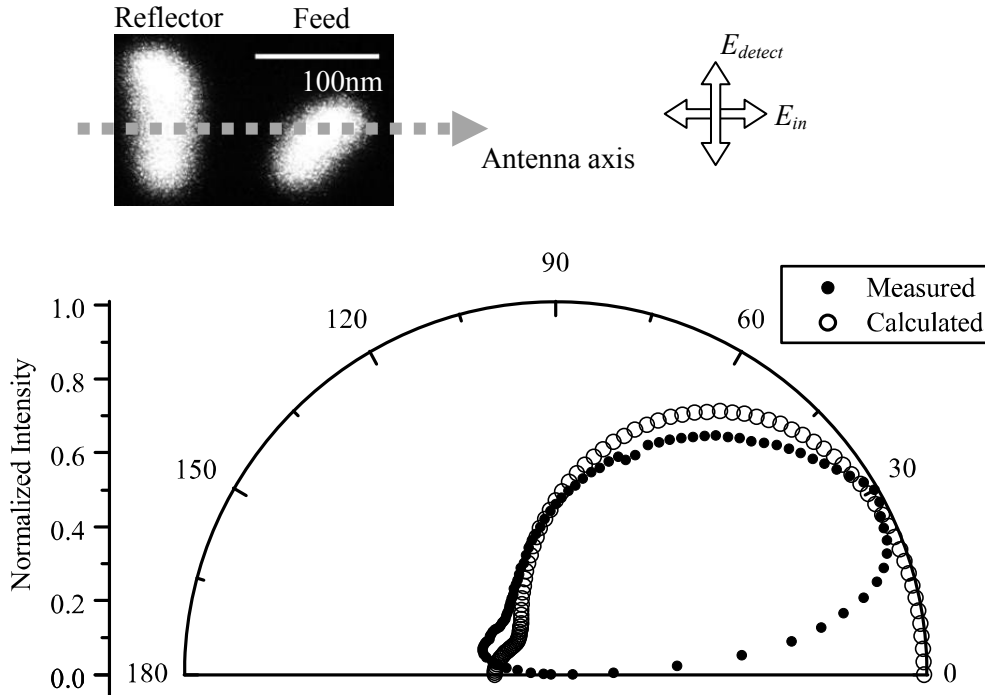


Fig. 5.14: Radiation pattern of the 2-element antenna consisting of a feed and a reflector. The inset shows the SEM image of the antenna. The solid and open circles represent the measured radiation pattern and the prediction based on the coupled dipole model, respectively.

(b) Feed with a director

Figure 5.15 shows a SEM image and the radiation pattern of the feed-director antenna. As mentioned in Section 5.4.1, the distance between the feed and the director was chosen to be the same as the feed-reflector distance in the antenna shown in Fig. 5.14, to compare the difference in the function between the director and the reflector. The measured patterns are plotted by the solid dots. The radiation patterns were normalized by the maximum intensity.

The radiation angle width of the forward emission became narrower than that of the feed-reflector antenna shown in Fig. 5.14, indicating that the director is functioning properly. The diminishing intensity around 0° and 180° in the measured pattern is likely to stem from the same origin as Fig. 5.14, namely the index mismatch.

The open circles in Fig. 5.15 are the the prediction based on the coupled dipole model using the dipole parameters shown in Table 5.2, without taking into account the effect of index mismatch.

Although the measured pattern is somewhat different from the prediction, an important feature that the dip occurred around 100° can be seen in both the patterns,

showing that the director is working as expected. Possible reasons for the discrepancy will be discussed in Section 5.4.4(b).

It is confirmed by the comparison of Fig. 5.14 with Fig. 5.15 that the element detuning can control the function of plasmon-based antennas in optical regime.

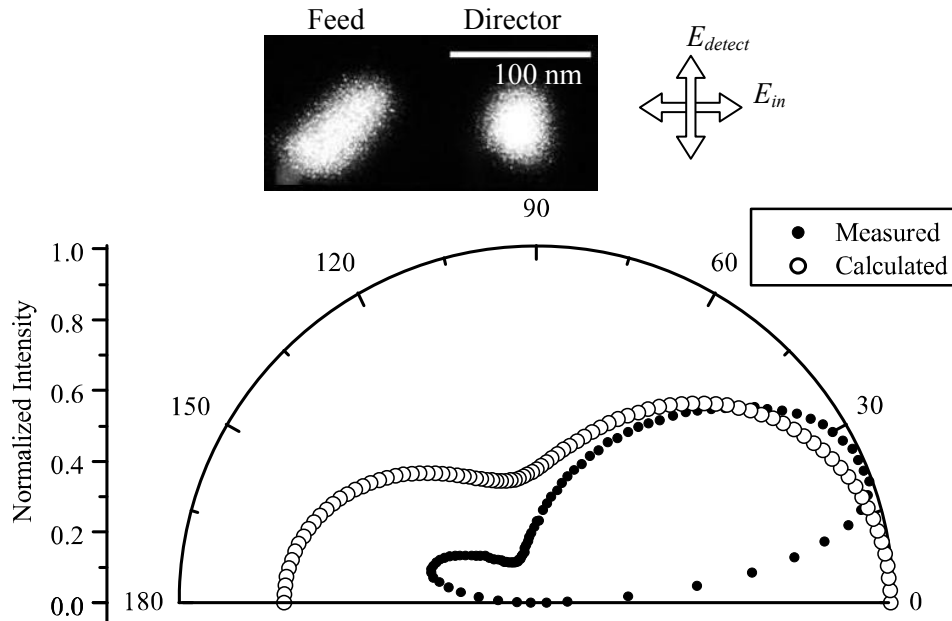


Fig. 5.15: Radiation pattern of the 2-element antenna consisting of a feed and a director. The inset shows the SEM image of the antenna. The solid and open circles represent the measured radiation pattern and the prediction based on the coupled dipole model, respectively.

5.4.3.3. 5-element antenna

Figure 5.16 shows a SEM image and the emission pattern of the 5-element optical Yagi-Uda antenna consisting of a feed, a reflector, and three directors. The experimental results are normalized by the maximum value and plotted by the solid dots. The forward emission is sharper than in the case of the feed-reflector antenna shown in Fig. 5.14, while the backward emission is more suppressed than in the case of the feed-director antenna shown in Fig. 5.15. These are the expected features of the 5-element Yagi-Uda antenna. The result definitely demonstrates the realization of a Yagi-Uda antenna in a visible region. The open circles show the prediction based on the coupled dipole model. The observed emission pattern is representing well the prediction except for the angles close to 0° and 180° where the mismatch of the refractive index between the SiO_x layer and the substrate diminishes the radiation as mentioned in Section 5.4.3.1. In particular,

the intensity dips appear around 60° and 120° in both the experiment and the prediction, indicating that the control of the radiation pattern is realized by the operating principles of the Yagi-Uda antenna described in Chapter 4.

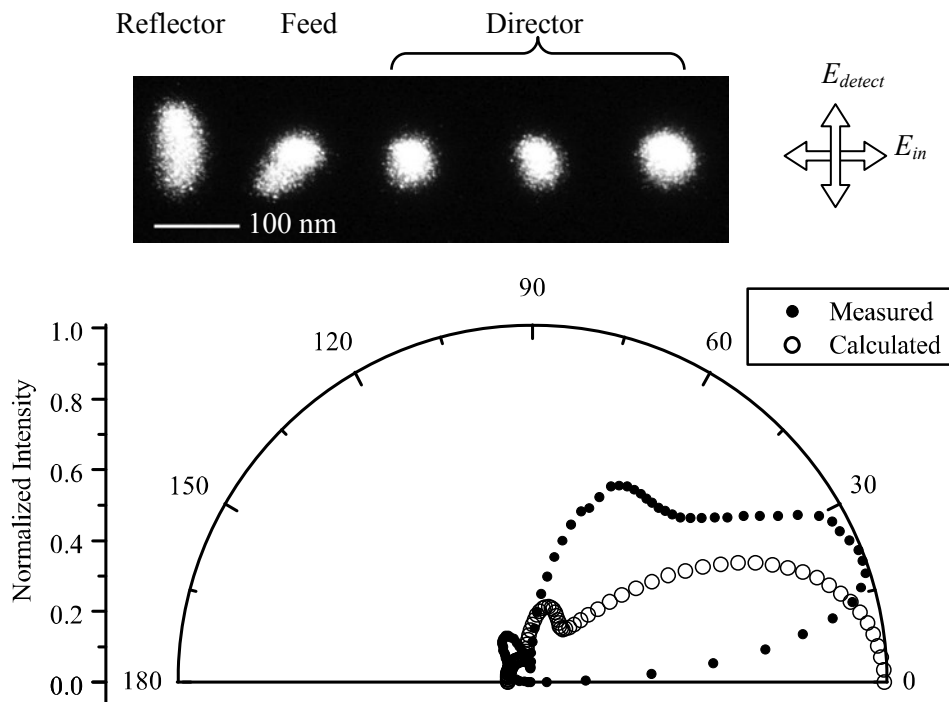


Fig. 5.16: Emission pattern from the 5-element antenna consisting of a feed, a reflector, and three directors. The inset shows the SEM image of the antenna. The solid (\bullet) and open circles (\circ) represent the measured radiation pattern and the prediction based on the coupled dipole model, respectively.

5.4.4. Discussions

(a) Effect of index mismatch on the radiation from the feed

In section 5.4.3.1, the radiation pattern of the feed, which diminishes at the angles around 0° and 180° , was explained as the result of the index mismatch between the medium above and below the antenna by the comparison of the measured radiation pattern with a prediction based on the reciprocity theorem [130]. In the theory, the emitter is assumed to be an infinitesimal dipole that oscillates parallel to the electric field of consideration. In the experiment, however, the feed had a finite size and the driving and detecting polarizations were orthogonal with each other and both were rotated by 45° from the major axis of the feed. In order to investigate the effect of index mismatch in the experimental situation, the FDTD simulation was performed with a model shown in Fig. 5.17(a). The size and the shape of the feed was the same as those shown in Fig.5.4. The polarization of the incident field E_{in} was tilted by 45° from the major axis of the feed and the polarization direction of the detection field E_{detect} was perpendicular to that of the incident field.

Figure 5.17(b) shows the experimental result and the calculated radiation pattern from the feed element placed at the dielectric interface in the case that the refractive index of the upper medium (0° to 180°) was lower than that of the lower medium.

First, it was confirmed that the reciprocity-based theoretical prediction (solid line) agrees very well with the FDTD simulation (Δ). Then, by comparing the experimental result with the FDTD simulation for the three cases of the index ratio, it was again confirmed that the experimental radiation pattern is explained by the index mismatch with the ratio of 1.05.

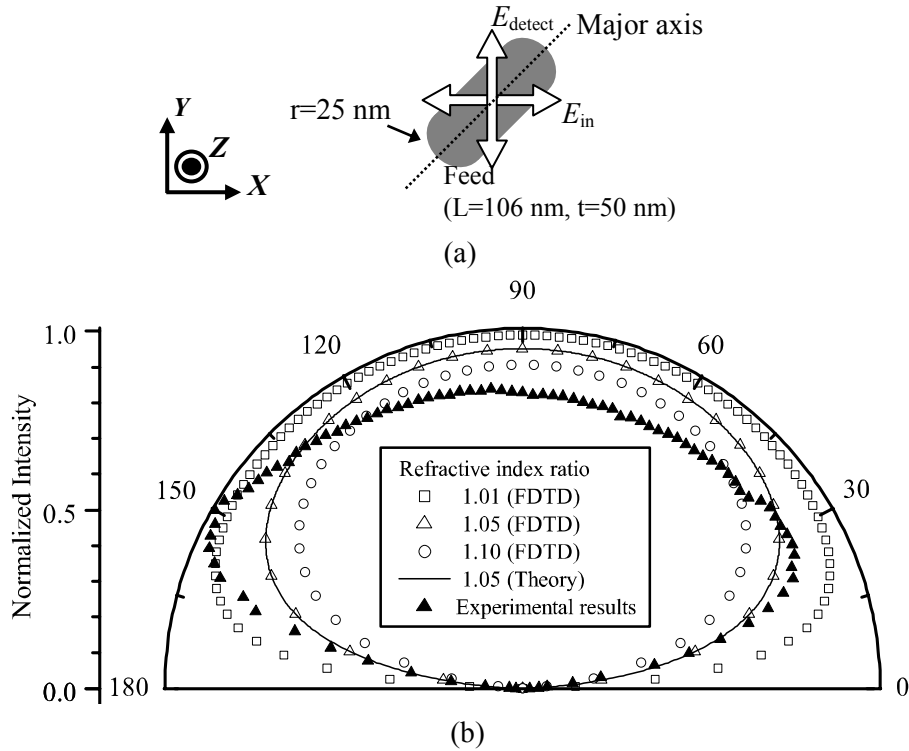


Fig. 5.17: Dependence of the radiation pattern on the refractive index difference above and below the feed. The range between 0° and 180° corresponds to the lower index side. The solid dots show the measured result shown in Fig. 5.13, open dots show the estimation by the FDTD method, and the solid line shows the prediction by the reciprocity-based theory.

(b) Effect of driving the director

As described in Section 5.2, the operating principle of the Yagi-Uda antennas that only the feed element is driven was realized experimentally in this work by using the polarization rotation for the incident light only in the tilted feed element and by detecting the antenna emission in the perpendicular polarization. The validity of the operating method is justified if the excitation of the passive element, which is not tilted, is sufficiently weak and/or the polarization rotation does not occur in the passive element. These conditions may be satisfied well in the reflector that has a well-defined rod shape with high aspect ratio (= major axis/minor axis).

In contrast, since the shape of the directors appeared to be almost circular, it was a matter of concern that the requirements could not be satisfied. Indeed, the resonance wavelengths for the two orthogonal incident polarizations were nearly the same in the director as shown in Fig. 5.12 (blue solid lines). The effect of the director driving on the antenna radiation pattern was therefore investigated by the two kinds of the experiment

as described below.

The first one was the evaluation of the polarization rotation in the directors, using the nano patterns that were used to evaluate the resonant wavelength of the director in Fig. 5.12. Since the director spacing was 800 nm as shown in Fig. 5.18, the total number of directors in the focus spot area (15 μm by 36 μm) was about 370. Figure 5.18 shows the radiation pattern from the directors observed in the X - Z plane. The open and solid dots show the cases of the incident polarization parallel and perpendicular to the detection polarization, respectively. The sharp peaks observed at 54° and 116° were caused by the interference effect. The radiation intensity emitted to the direction of 90° in the orthogonal driving (\blacksquare) was about five times weaker than that in the parallel driving (\circ), suggesting that the polarization rotation in the directors was sufficiently small.

Additionally, the transmission spectra shown in Fig. 5.12 (a) indicate that the response of the resonantly driven feed was stronger than the response of the directors.

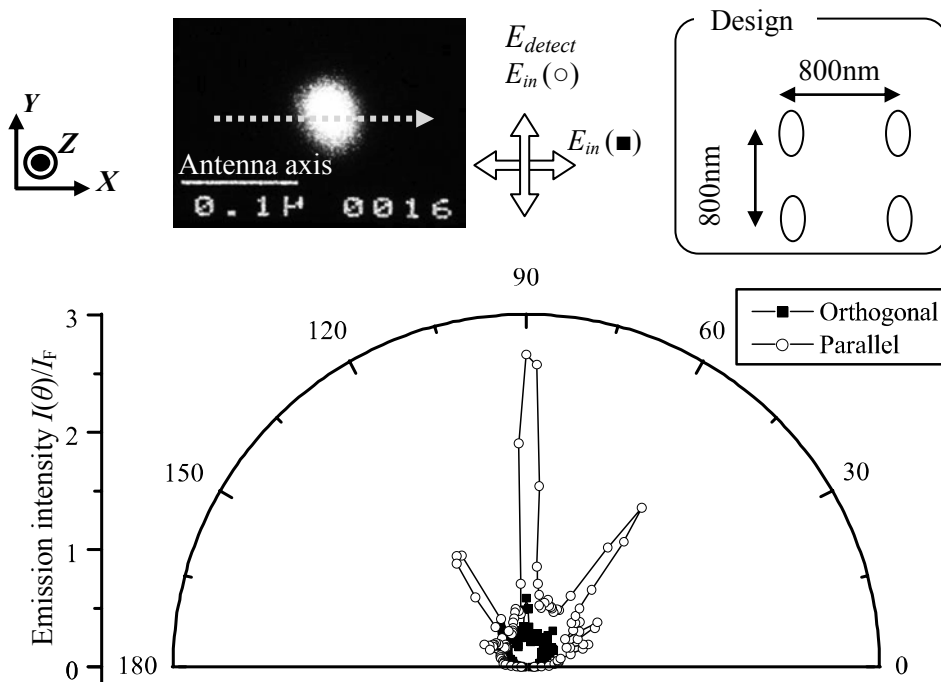


Fig. 5.18: Radiation pattern of directors in the X - Z plane. The open-dots(\circ)/solid-dots(\blacksquare) show the cases of incident polarization parallel/perpendicular to the detection polarization.

The second experiment was performed to ensure that the directional emission of light in the feed-director antenna shown in Fig. 5.15 was not caused by the rotation of the

incident field at the directors. Figure 5.19 shows a SEM image and the radiation pattern of the feed-director antenna in the X - Z plane. The open dots correspond to an incident field parallel to the detected polarization (simultaneous driving of feed and director), and the solid dots show that the incident field was polarized orthogonal to the detected field (the results shown in Fig. 5.15). Obviously, the simultaneous driving (\circ) does not result in the directional emission.

The results shown above confirm that the effect of driving directors is negligible in the observed radiation patterns of the Yagi-Uda antennas. The results shown in Fig. 5.19 also exclude the possibility that the discrepancy between the prediction and the experimental result for the feed-director antennas shown in Fig. 5.15 is caused by the driving of the directors. The reason for the discrepancy is unclear. One of the possibilities is an error of the evaluation of the director parameter from the shallow spectral dip as shown in Fig. 5.12.

Another possibility is the proximity effect, because the tilt of the feed makes the edge of the feed closer to the director than the center-to-center distance as described in Section 5.2. Under these circumstances, stronger interaction than the prediction between elements might have occurred, resulting in a higher directivity of the emission than the prediction based on the dipole model.

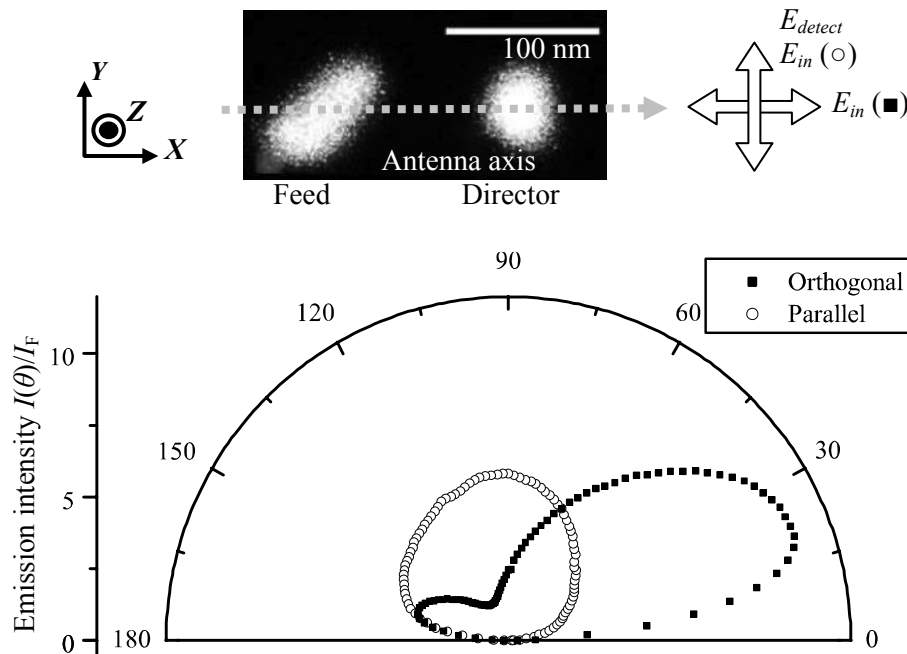


Fig. 5.19: The SEM image of a feed-director antenna, and the radiation pattern of the feed-director antennas in the X - Z plane. The open and solid dots show the cases of the incident polarization being parallel and orthogonal to the detection polarization, respectively.

(c) Estimation of efficiency

The radiation efficiency of the antenna was evaluated as follows. Since the input power to the feed element depends a great deal on the alignment in the measurement set-up, it is not appropriate to estimate the radiation efficiency from the directivity measurement of the antennas. On the other hand, as shown in Table 5.2, the transmission spectra could give the estimation of the material loss γ given by the relative value to the radiation loss. Therefore, the radiation efficiency of each element is given as $1/(1+\gamma)$. The evaluated values are listed in Table 5.3, in which γ is given by Table 5.2. In the case of the reflector, 22.2% of the input power was lost as the material losses, and 77.8% of the input power was emitted. In the case of the feed, 27.5% of the input power was lost as the material losses, and 72.5% of the input power was emitted. In the case of the directors, 30.5% of the input power was lost as the material losses, and 69.5% of the input power was emitted.

Assuming that the interference effects in the antenna are canceled when integrating over all radiation angles, it is possible to estimate that the radiation efficiency of the antenna should be similar to the efficiency of the antenna elements. Therefore, the radiation efficiency of the antenna was estimated to be at least 70 %, which was the efficiency of the director.

Table 5.3: Ratio of the radiation and the material loss estimated at 662 nm (vacuum). The antennas were assumed to be embedded in $\text{SiO}_x(n \sim 1.44)$. The value of γ is given by Table 5.2.

	Loss parameter γ	Material Loss [%] $\gamma/(1+\gamma)$	Radiation [%] $1/(1+\gamma)$
Reflector	0.285	22.2	77.8
Feed	0.380	27.5	72.5
Director	0.438	30.5	69.5

The results shown so far suggest that the practical material loss in the gold nanopatterns is not very large, and that the radiative interaction between antenna elements is strong. Hence, there is a possibility that the forward radiation was further enhanced by increasing the number of directors, as shown below. The calculation model is the same as that shown in Fig. 4.15, except for varying the number of directors. The design parameters of each element are given by the experimental results shown in Table 5.2. In addition, following the experimental arrangement, the feed-reflector distance was $X_r=1.7$ and the director spacing X_d was $X_d=2.0$ for all the cases. Figure 5.20 shows the

dependence of the antenna emission on the number of directors. Figure 5.21 shows the dependence of the half power beam width (HPBW), and the forward $I(0)/I_F$ and the backward $I(\pi)/I_F$ radiation intensities on the number of directors. The backward emission was suppressed the most in the case of two directors. On the other hand, the forward emission was enhanced with the increase of the number of directors. This result suggests that even though the material losses are not negligible in optical regime, increasing the number of directors enhances the directivity of the optical Yagi-Uda antenna composed of gold nanorods, as in the case of RF regime.

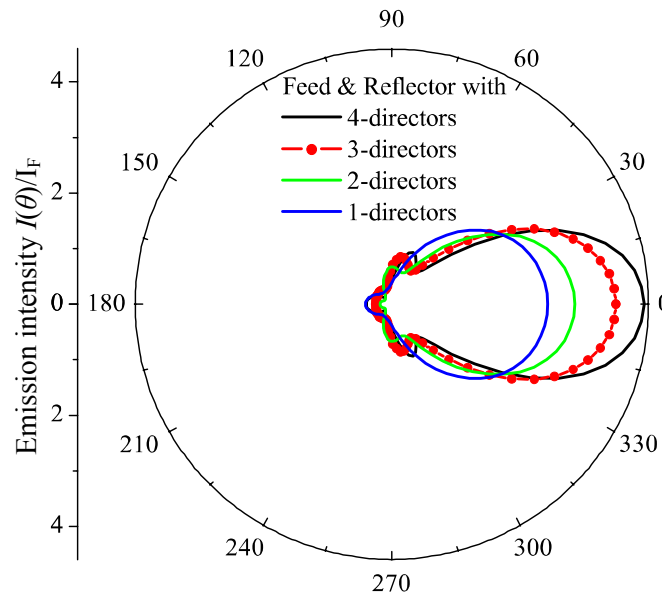


Fig. 5.20: The prediction of the radiation pattern for various numbers of the directors, including the material losses. The material parameters of each element are given by Table 5.2.

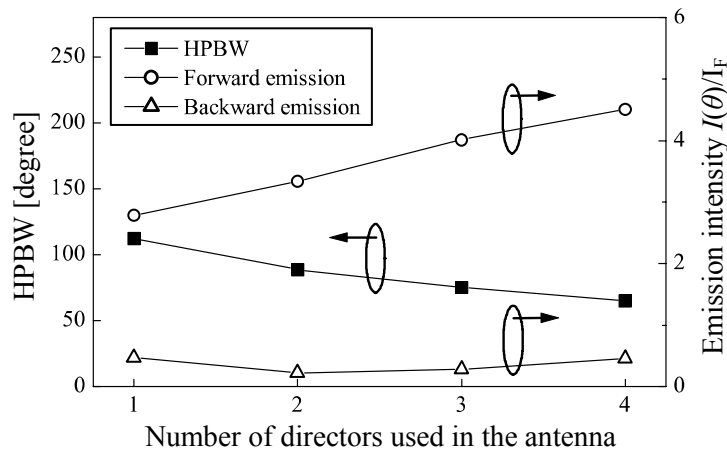


Fig. 5.21: Dependence of the antenna emission on the number of directors obtained by Fig. 5.20. Open circles show the forward emission, open triangles show the backward emission, and solid squares show the HPBW of the forward emission, respectively.

5.5. Working wavelength dependence

One of the advantages of Yagi-Uda antennas is that the antenna functions are insensitive to the working wavelength in comparison with, for example, grating couplers. Indeed, Yagi-Uda antennas are categorized as a broadband antenna in RF range, and hence they are used for the multi-channel broadcasting. Therefore, it is important to investigate the wavelength dependence of the optical Yagi-Uda antenna. In the experiments described in Section 5.4, the antennas were arrayed as shown in Fig. 5.9 to enhance the detection power. Since the radiation from the arrayed antenna is affected by the interference effect occurred between each antenna, the incident wavelength needs to be matched with the fixed distance between the antennas. In order to exclude the interference effect, a single 5-element Yagi-uda antenna was used to investigate the working wavelength dependence of the radiation pattern [131].

5.5.1. Antenna design & layout

Figure 5.22 shows the design of a 5-element antenna which was similar to that shown in Fig. 5.8(c), except that the antenna pitch was chosen as $50\ \mu\text{m}$ as shown in Fig. 5.23 to excite only one antenna by the incident light of spot size $15\ \mu\text{m} \times 36\ \mu\text{m}$.

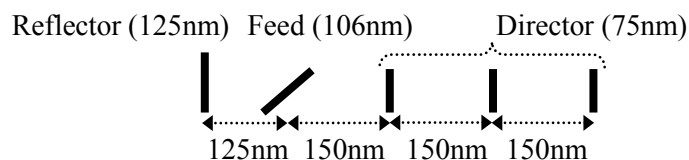


Fig. 5.22: Design of the 5-element nano optical Yagi-Uda antenna.

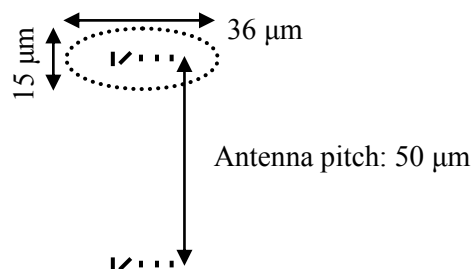


Fig. 5.23: Relation between the single antenna and the spot size of the incident light.

5.5.2. Resonant wavelength of each element

Figure 5.24 shows the design of nanopattern to estimate the resonant wavelength of the antenna element. Optical antennas and nanopatterns were fabricated on the same substrate simultaneously. The sample layout is shown in Appendix III Fig. C. Figure 5.25 shows the SEM images of the fabricated nanopatterns. The measured length of each element was (a) 75 nm, (b) 105 nm, and (c) 121 nm. Figure 5.26 shows the transmission spectra of the elements. The resonant wavelength corresponding to the longer axis of the element was estimated to be 600 nm, 700 nm, and 770 nm for the element length of 75 nm, 105 nm, and 121 nm, respectively.

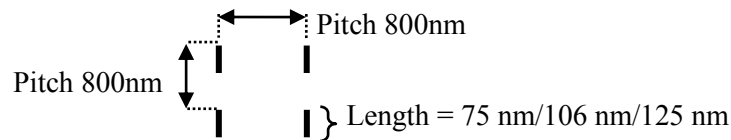


Fig. 5.24: Design of nanopattern to estimate the resonant wavelength of antenna element.

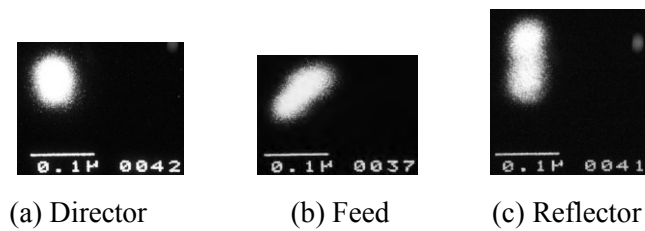


Fig. 5.25: SEM images of each element. Measured length (L) and width (W) were (a) $L=75$ nm and $W=63$ nm, (b) $L=105$ nm and $W=51$ nm, (c) $L=121$ nm and $W=53$ nm.

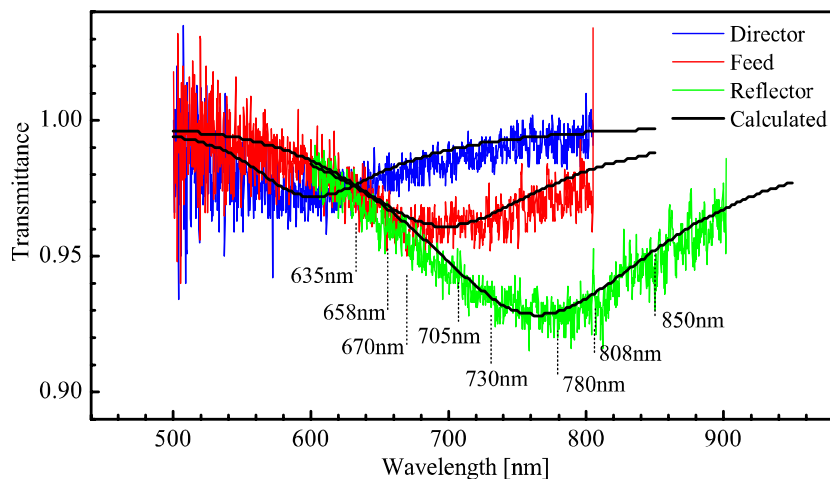


Fig. 5.26: Transmission spectra of the element. Incident field was polarized parallel to the longer axis of element. The black solid lines show the results of the dipole fitting. Dotted lines with annotations show the wavelengths of laser diodes used in this work.

In order to compare the measured radiation pattern with the prediction based on the coupled dipole model, dipole parameters of each element were estimated by fitting the transmission spectrum with the dipole model in the same procedure that used in Section 5.4.2. The solid lines in Fig. 5.26 show the results when it is assumed that the nano patterns are embedded in SiO_x ($n \sim 1.44$). The evaluated parameters are shown in Table 5.4.

Table 5.5 shows the material loss and the detuning of each element for different input wavelength estimated by substituting the parameters described in Table 5.4 into Eq. (2.38) and Eq. (2.39). The wavelengths are those of the laser diodes used in this work. Note that as for the geometrical element spacing fixed in the experiment, the element spacing scaled by the operating wavelength varied as shown in Table 5.5.

As a result of changing the input wavelength, the property of each element varied. Based on the detuning values shown in Table 5.5, Table 5.6 summarises the relation between the input wavelengths and the functions of the each element. The element functions are determined on the basis of the relation between the function and the element detuning described in Section 4.1.2.

Table 5.4: The dipole parameters of the elements evaluated by fitting the transmission spectra shown in Fig. 5.26 with the imaginary part of Eq. (5.1). Parenthetic values are the volume of the element estimated from the measured geometrical size from the SEM images shown in Fig. 5.25.

	Resonant wavelength [nm]	Depolarization Factor N	Volume of nanorod V [m ³]
Director	600	0.19	3.0×10^{-22} (2.36×10^{-22})
Feed	700	0.118	2.9×10^{-22} (2.68×10^{-22})
Reflector	770	0.093	3.2×10^{-22} (3.21×10^{-22})

Table 5.5: The loss parameter γ of each element for different input wavelength given by substituting the fitting parameters shown in Table 5.4 into Eq. (2.38). Parenthetic values are the detuning δ of each element given by Eq. (2.39). The surrounding medium was assumed to be SiOx ($n \sim 1.44$). The element spacing was described in terms of the wavelength λ in medium.

Input wavelength	635 nm	658 nm	670 nm	705 nm	730 nm	780 nm	808 nm	850 nm
Spacing of Director $X_D (r_D)$	$X_D=2.14$ (0.340 λ)	2.06 (0.328 λ)	2.02 (0.322 λ)	1.92 (0.306 λ)	1.86 (0.296 λ)	1.74 (0.277 λ)	1.68 (0.267 λ)	1.60 (0.254 λ)
Spacing of Reflector $X_R (r_R)$	$X_R=1.78$ (0.283 λ)	1.72 (0.274 λ)	1.68 (0.268 λ)	1.60 (0.255 λ)	1.55 (0.247 λ)	1.45 (0.231 λ)	1.40 (0.223 λ)	1.33 (0.212 λ)
Director $L=75\text{nm}$ $\gamma_D (\delta_D)$	$\gamma_D=0.268$ (-0.996)	0.241 (-1.469)	0.231 (-1.72)	0.212 (-2.49)	0.205 (-3.08)	0.201 (-4.37)	0.202 (-5.16)	0.207 (-6.45)
Feed $L=105\text{nm}$ $\gamma_F (\delta_F)$	$\gamma_F=0.278$ (0.587)	0.249 (0.28)	0.239 (0.119)	0.220 (-0.365)	0.213 (-0.729)	0.208 (-1.518)	0.209 (-2.00)	0.214 (-2.80)
Reflector $L=121\text{nm}$ $\gamma_R (\delta_R)$	$\gamma_R=0.252$ (1.041)	0.226 (0.82)	0.217 (0.706)	0.199 (0.366)	0.193 (0.113)	0.189 (-0.432)	0.189 (-0.766)	0.194 (-1.312)

Table 5.6: Relation between the function of the element and the input wavelength. Parenthetic annotations describe the characteristics of the element decided by the detuning values shown in Table 5.5 with the relation between the antenna function and the detuning described in Section 4.1.2.

Input wavelength [nm]	635	658	670	705	730	780	808	850
Measured Element Length (Resonant wavelength)	75nm (600nm)	Director (Capacitive)						
	105nm (700nm)	Feed or Reflector (Inductive)			Feed or Director (Capacitive)			
	121nm (770nm)	Reflector (Inductive)				Director (Capacitive)		

5.5.3. Directionality

Figure 5.27 shows a SEM image of the fabricated 5-element optical Yagi-Uda antenna in this work. The solid dots plotted in Fig. 5.28 show the measured radiation patterns in the X - Z plane of the antenna for various input wavelengths. The measurements were performed with the set-up shown in Fig. 5.6. The open dots show the predicted radiation patterns based on the coupled dipole model with the parameters shown in Table 5.4 and Table 5.5. The predictions suggest that although the corresponding element spacing varies as shown in Table 5.5, the antenna can show the desired directivity at the wavelength of 658nm, 670 nm, 705 nm, and 730 nm. The radiation intensity diminution observed at around 0° and 180° in all results was caused by the refractive index difference above and below the antenna as described in Section 5.4.4(a).

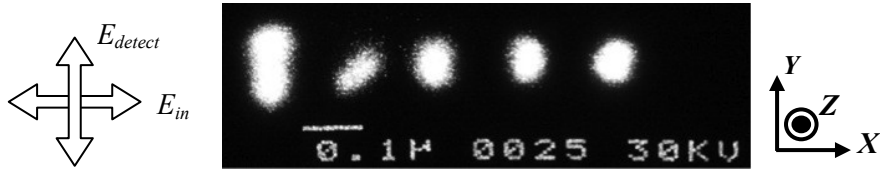


Fig. 5.27: SEM image of a 5-element nano-optical Yagi-Uda antenna.

At the wavelength of 658 nm, 670nm, 705 nm, and 730 nm, the forward emission was strong and the backward radiation was well suppressed, which was in agreement with the predictions. In particular, similarly to the results shown in Section 5.4, the dipole model reproduced the depth, the direction, and the number of dip structures observed in the experiment. In the sense that the radiation went mostly to the main lobe ($\theta = 0^\circ$), a good directionality was realized in the range 660 nm ~ 730 nm. That range was about 10% (70 nm) of the resonant wavelength of the feed (700 nm). Therefore, it is possible to conclude that the optical Yagi-Uda antenna is broadband, as in the case of RF regime.

As for the input wavelength of 635 nm, in contrast, the observed pattern could not be said to be directional. However, the observed pattern was qualitatively consistent with the prediction in a point that the dip occurred at around 50° , 100° , and 140° , although the observed radiation pattern seemed somewhat different from that of the prediction.

The antennas also did not show good directivity at the wavelength of 780 nm, 808 nm, and 850 nm. The observed radiation patterns at these wavelengths are considered as follows. According to Table 5.6, when the input wavelength is longer than the resonant

wavelength of the reflector (770 nm), the reflector works as director. Hence the feed is seen as being sandwiched by the directors. It is therefore intuitively obvious that the side lobes (radiation to the direction of 90 degrees and 270 degrees) are suppressed and that the direction of the antenna emission is determined by the competition between the reflector (working as a director) and the three directors. Figure 5.26 suggests that since the response of the directors becomes weaker than that of the reflectors at such long wavelengths, the backward emission becomes stronger than the forward emission. That is clear in the theoretical prediction shown in Fig. 5.28.

In addition, the dipole model could not reproduce the observed radiation patterns particularly for 808 nm and 850 nm. The reason for the discrepancy is likely to be due to the input wavelength far from the operating range of the wavelength of the directors. Since the emission spectrum of each nanoparticle is described by the Lorentz model, in which the linewidth of the spectrum is finite, the parameters evaluated by the dipole model are assumed to be different from the proper parameters when the input wavelength is far from the resonance. In fact, as shown in Table 5.5, at the input wavelength of 780 nm, the detuning of the director and the feed element from each resonance wavelength were 182% ($=4.37/(2(1+0.201))$) and 63% ($=1.518/(2(1+0.208))$), respectively of the FWHMs of the resonance.

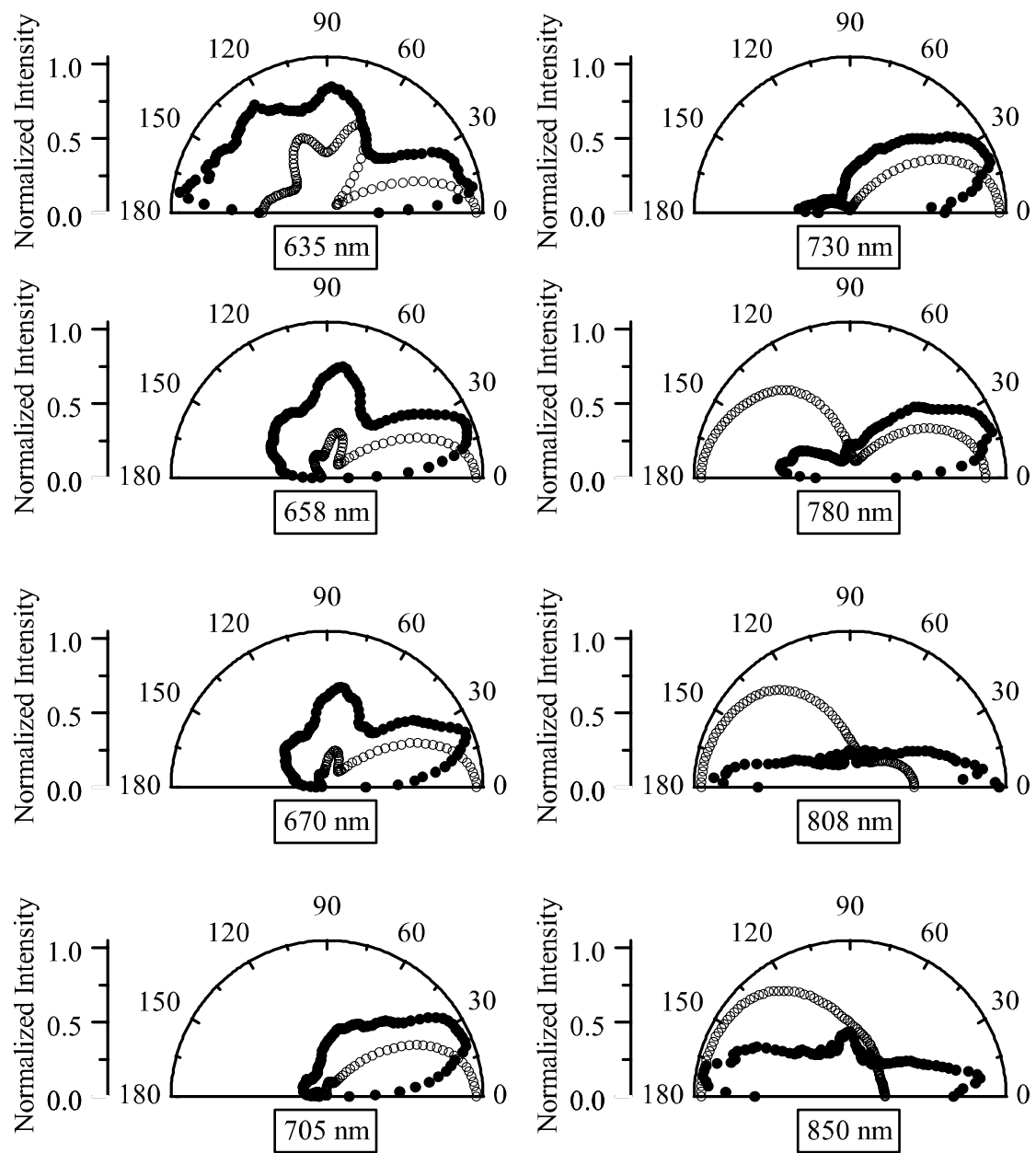


Fig. 5.28: Radiation pattern of the single 5-element nano-optical Yagi-Uda antenna for different input wavelengths. The solid dots show the observed radiation pattern. The open dots show the prediction based on the coupled dipole model, using the fitting parameters shown in Table 5.4 and Table 5.5.

5.6. Summary

In this chapter, experimental validation of the directional control of light with nano-optical Yagi-Uda antennas has been described. On the basis of the antenna design described in Chapter 4, the antennas were fabricated by the electron beam lithography together with a bi-layer resist process and the gold lift-off process. In order to reproduce the design assumption that the incident field should be injected only into the feed element, the feed element was driven by the polarization dependence of the nanorod response on the external driving field. In practice, the feed was tilted by 45 degrees toward the antenna axis, and driven by the light polarized parallel to the antenna axis. In order to evaluate the antenna parameters, the transmission spectra of the antenna elements were observed and fitted with the dipole model. On the other hand, the antenna radiation patterns were observed with a measurement system specially constructed for this work. The findings obtained through the experiments are as follows.

a) 1-element (Feed) antenna

The radiation pattern from the arrayed feed was nearly symmetric around the normal to the substrate. In addition, the radiation intensity was found to diminish at the angles close to the surface of the substrate. The phenomenon was considered by the reciprocity-based theory and the FDTD method. As a result, it was concluded that the difference in the refractive indices between the upper layer and the lower layer of the feed element caused the intensity diminution.

b) 2-element (Feed + Director, Feed + Reflector) antenna

A 2-element antenna consisting of a feed element and either a director or a reflector was investigated to validate the idea that the function of the antenna element can be controlled by adjusting the element detuning.

In the case of the feed-reflector antenna, backward radiation was suppressed very well. Additionally, the prediction based on the coupled dipole model reproduced the observed results very well. However, in the case of the feed-director antenna, the observed antenna radiation pattern was somewhat different from the prediction. Among possible reasons for the discrepancy, the possibility of the effect of simultaneous driving of both the feed and the director elements is assuredly excluded. As a result, the errors in the evaluation of dipole parameters of the director and the proximity effect due to the tilting of the feed are suggested to be the reason for the discrepancy.

Since the completely different patterns between the feed-reflector and the feed-director antennas were observed, which are in agreement well with the theory, it is concluded that the function of the element is controlled well by the element detuning.

c) 5-element (Feed x 1, Reflector x 1, Director x 3) antenna

The radiation pattern from the 5-element antenna array was investigated. The antenna had a reflector, a feed, and three directors. The observed pattern showed that the forward emission was sharper, and that both the backward radiation and the side lobes were suppressed more than those of the 2-element antenna as predicted by the coupled dipole model. The coupled-dipole model prediction reproduced well the observed pattern. Additionally, through the consideration of the dipole parameters evaluated from the transmission spectrum of each element, the radiation efficiency of the antenna was estimated to be as high as 70% with 30% material losses inside the elements. Based on the experimental values of the dipole parameters, it is predicted by the coupled dipole model that increasing the number of directors may enhance the directivity of an optical Yagi-Uda antenna as in the case of RF region.

d) Dependence of the antenna radiation on the input wavelength

The dependence of the antenna radiation pattern on the input wavelength was investigated both experimentally and theoretically by using a single 5-element antenna. It is shown that the directional radiation is obtained in the wavelength range of 10% of the design wavelength. It is suggested that the simple dipole model will not be applicable to the nano rod element when the input wavelength is far from the resonance wavelength.

6. Conclusion

In this work, the directional control of light by a nano-optical Yagi-Uda antenna consisting of gold nanoparticles was investigated theoretically and experimentally. On the basis of the coupled dipole model, taking into account the material losses, the antenna was designed and fabricated. The observed radiation pattern demonstrated the accomplishment of realizing an optical Yagi-Uda antenna. Until this work, most of the reports on optical antennas had focused on the single dipole antenna. In contrast, this work demonstrated the directional control of light by arranging the dipole elements. The results indicate that the antenna concepts and designs which are highly developed in RF regime are applicable to the optical regime, provided that the plasmonic characteristics of metals are appropriately taken into account. The followings are the summary of the important findings of this work.

a) Material losses and antenna efficiency

The ohmic loss is the most significant issue in plasmonics, namely the metal-based optical technology. It is particularly critical in localized surface plasmon (LSP) based devices whose light field is tightly confined in the metal nanostructures. In this work, it is clarified that the volume of the element is a key factor in lowering the effect of the material losses, expressed by a parameter γ_{mat} (= material loss/radiation loss), and a simple estimation method is established based on the ellipsoidal model of the particle. By relating the γ_{mat} to the length of nanoparticles with a fixed aspect ratio 2.76 (= major-/minor-axis) at its resonant wavelength of 705 nm (vacuum), $\gamma_{mat} = 0.28$ is found to be achievable for the case of major-axis length 138 nm, inside glass ($n=1.516$). The coupled dipole model predicts that the optical Yagi-Uda antenna can show a desired directivity provided that the material losses in metals are the same or lower than the radiation loss.

In this work, the dipole parameters of the fabricated antenna elements, including γ_{mat} , were evaluated by the transmission spectrum of nanoparticles fitted by a dipole model. The experimental results show qualitative similarity to the prediction of dipole model in which γ_{mat} increases with the decrease of the volume of the nanoparticle. Even the smallest volume, γ_{mat} of the fabricated director (major-axis length = 58 nm) is 0.438, which satisfies the requirement for the directional emission predicted by the coupled dipole model.

The straightforward derivation of the antenna emission efficiency is difficult to

estimate by measuring the radiation power, since the intensity of incident light (excitation efficiency) strongly depends on the details of the set-up. Here, in this work, the efficiency is roughly estimated by the evaluated antenna parameters. As a result, it is shown that a one-third of the input power is lost as the material losses, and that the remaining two-thirds are radiated.

b) Directivity of radiation

It is necessary for the directional emission of Yagi-Uda antenna to drive feed only. In this work, the polarization dependence of the nanorod was utilized. In fact, only the feed was tilted to 45° from the antenna axis, and the incident field was polarized parallel to the antenna axis. By this method, it was effectively realized to drive feed only.

The directivity was measured by a homemade set-up. The feed element was confirmed to show nearly symmetric radiation around the normal to the surface, which validates the use of the measurement set-up as well as the driving method of the antenna by the tilted feed. The 2-element antenna consisting of a feed and a director, and that of a feed and a reflector showed completely different directivity with each other. That is consistent with the prediction as well as suggests that the element's detuning effectively controls the element function as in RF regime. The results also suggest that even such a simple structure can alter the directionality of emission, which will be useful for application. The 5-element optical Yagi-Uda antenna exhibits the desired directivity as in RF regime; the narrow forward emission is strong while the backward emission is well suppressed.

In the measurement, diminishing emission in the vicinity of the substrate surface was also observed. By applying the reciprocity-based theory, the results were explained by the refractive index mismatch of $\sim 5\%$ between the medium above and below the antenna. The result suggests that the control of the refractive index surrounding the antenna is critically important for the use of the antenna in in-plane geometry.

c) Bandwidth

The dependence of directivity of a single 5-element optical Yagi-Uda antenna on the incident wavelength was investigated. As a result, a good directionality was obtained in the wavelength range 660 nm \sim 730 nm. This range is about 10% of the resonant wavelength of the feed (700 nm). Therefore, this antenna can be considered as a broadband antenna, as in the case of RF regime.

The antennas in RF regime are widely used for the various wireless communications. Similarly, optical Yagi-Uda antenna or other directional antennas are promising to be applied to wireless optical interconnection between various devices and between nano-chips including single nano emitter/detector in a device [132-134]. In this regard, vertical Yagi-Uda antenna structure will be useful since it is free from the index-mismatch problem [135]. Though a multi-element vertical Yagi-Uda structure is not easy to be fabricated, this work demonstrated that an addition of only a reflector/director to the feed could give a good directivity. Another possible usage of the Yagi-Uda structure may be the efficient coupler for planar dielectric or plasmonic optical waveguide [136, 137]. A unique promising application of directional control of light by the optical antennas is the enhancement of the performance of various sensors, which are strongly expected in chemistry, biology, and medicine. The high directionality of the antenna structures can also be expected to make the metamaterials even more functional [138]. In such a way, this work contributes to the enlargement of the application range of optical antennas, and eventually the importance and usefulness of nano optics.

References

1. L. Novotny and B. Hecht. Principles of Nano-Optics: Second Edition (Cambridge University Press, 2012).
2. 岡本隆之, 梶川浩太郎. プラズモニクス-基礎と応用. 講談社サイエンティフィック (2010).
3. S. A. Maier. Plasmonics: Fundamentals and Applications. Springer (2007).
4. Max Born and Emi Wolf (著), 草川徹, 横田英嗣(訳): 光学の原理 I, 東海大学出版会 (1974).
5. E. Abbe. Beiträge zur Theorie des Mikroskops und der mikroskopischen Wahrnehmung. Arch. Mikroskop. Anat., vol. 9, p. 413-420 (1873).
6. L. Rayleigh. On the theory of optical images, with special reference to the microscope. Philos. Mag., vol. 42, p. 167-195 (1896).
7. M. Minsky. Memoir on inventing the confocal scanning microscope. Scanning Vol. 10, Iss. 4, p. 128-138 (1988).
8. 光学系の仕組みと応用. オプトロニクス社編集部編, オプトロニクス社 (2003).
9. E. H. Synge. A suggested method for extending microscopic resolution into the ultra-microscopic region. Phil. Mag., vol. 6, p. 356-362 (1928).
10. L. Novotny. The history of near-field optics. Progress in Optics, Vol. 50, ed. E. Wolf. Amsterdam: Elsevier, p. 137-180 (2007).
11. J. Wessel. Surface-enhanced optical microscopy. J. Opt. Soc. Am. B, vol. 2, p. 1538-1541 (1985).
12. U. Ch. Fischer and D. W. Pohl. Observation of Single-Particle Plasmons by Near-Field Optical Microscopy. Phys. Rev. Lett. vol. 62, p.458 (1989).
13. L. Malmqvist and H. M. Hertz. Two-color trapped-particle optical microscopy. Opt. Lett. vol. 19, Issue 12, p. 853-855 (1994).
14. Y. Inouye and S. Kawata. Near-field scanning optical microscope with a metallic probe tip. Opt. Lett. vol. 19, Issue 3, p. 159-161 (1994).
15. S. Kawata, Y. Inouye and T. Sugiura. Near-Field Scanning Optical Microscope with a Laser Trapped Probe. Jpn. J. Appl. Phys. vol. 33, L1725-1727 (1994).
16. D. W. Pohl, W. Denk, and M. Lanz. Optical stethoscopy: Image recording with resolution $\lambda/20$. Appl. Phys. Lett. vol. 44, p.651 (1984).
17. A. Lewis, M. Isaacson, A. Harootunian, A. Muray. Development of a 500 Å spatial resolution light microscope. Ultramicroscopy. Vol. 13, p. 227-231 (1984).
18. G. Binnig, H. Rohrer, Ch. Gerber, and E. Weibel. Tunneling through a controllable vacuum gap. Appl. Phys. Lett. vol. 40, p.178 (1982).
19. R. H. Ritchie. Plasma Losses by Fast Electrons in Thin Films. Phys. Rev. vol. 106, p. 874 (1957).
20. C. J. Powell and J. B. Swan. Effect of Oxidation on the Characteristic Loss Spectra of Aluminum and Magnesium. Phys. Rev. vol. 118, p.640 (1960).
21. A. Otto. Excitation of nonradiative surface plasma waves in silver by the method of frustrated total reflection. Z. Phys. 216, p. 398-410 (1968).
22. E. Kretschmann and H. R  ther. Radiative decay of nonradiative surface plasmon excited by light. Z. Naturf., vol. 23A, p. 2135-2136 (1968).
23. J. Takahara, S. Yamagishi, H. Taki, A. Morimoto, and T. Kobayashi. Guiding of a one-dimensional optical beam with nanometer diameter. Opt. Lett., Vol. 22, No. 7, p. 475-477 (1997).
24. J. Homola, Sinclair S. Yee, G. Gauglitz. Surface plasmon resonance sensors: review.

- Sensors and Actuators B: Chemical, Vol. 54, Iss. 1–2, p. 3-15 (1999).
25. C. Nylander, B. Liedberg, T. Lind. Gas detection by means of surface plasmon resonance. *Sensors and Actuators*, Vol. 3, p. 79-88 (1982/1983).
 26. B. Liedberg, C. Nylander, I. Lunström. Surface plasmon resonance for gas detection and biosensing. *Sensors and Actuators*, Vol. 4, p. 299-304 (1983).
 27. R. Slavík, J. Homola, J. Čtyroký. Single-mode optical fiber surface plasmon resonance sensor. *Sensors and Actuators B: Chemical*, Vol. 54, Iss. 1–2, p. 74-79 (1999).
 28. J. Homola, R. Slavík, and J. Čtyroký. Interaction between fiber modes and surface plasmon waves: spectral properties. *Opt. Lett.* vol. 22, Iss. 18, p. 1403-1405 (1997).
 29. M. Mrksich, G. B. Sigal, and G. M. Whitesides. Surface Plasmon Resonance Permits *in Situ* Measurement of Protein Adsorption on Self-Assembled Monolayers of Alkanethiolates on Gold. *Langmuir*, vol. 11, p.4383-4385 (1995).
 30. G. B. Sigal, C. Bamdad, A. Barberis, J. Strominger, and G. M. Whitesides. A Self-Assembled Monolayer for the Binding and Study of Histidine-Tagged Proteins by Surface Plasmon Resonance. *Anal. Chem.* vol. 68, p.490-497 (1996).
 31. C. R. Yonzon, E. Jeoung, S. Zou, G. C. Schatz, M. Mrksich, and R. P. Van Duyne. A Comparative Analysis of Localized and Propagating Surface Plasmon Resonance Sensors: The Binding of Concanavalin A to a Monosaccharide Functionalized Self-Assembled Monolayer. *J. AM. CHEM. SOC.*, vol. 126, p.12669-12676 (2004).
 32. Alexandre G. Brolo. Plasmonics for future biosensors. *Nat. Photon.*, Vol. 6, p.709-713 (2012).
 33. M. Bauch, K. Toma, M. Toma, Q. Zhang, and J. Dostalek. Plasmon-Enhanced Fluorescence Biosensors: a Review. *Plasmonics* 9, p.781–799 (2014).
 34. C. R. Yonzon, C. L. Haynes, X. Zhang, J. T. Walsh, Jr., and R. P. Van Duyne. A Glucose Biosensor Based on Surface-Enhanced Raman Scattering: Improved Partition Layer, Temporal Stability, Reversibility, and Resistance to Serum Protein Interference. *Anal. Chem.*, Vol. 76, p.78-85 (2004).
 35. A. D. Taylor, J. Ladd, Q. Yu, S. Chen, J. Homola, and S. Jiang. Quantitative and simultaneous detection of four foodborne bacterial pathogens with a multi-channel SPR sensor. *Biosensors and Bioelectronics*, Vol. 22, Iss. 5, p. 752-758 (2006).
 36. Gustav Mie. Contributions to the optics of turbid media, particularly of colloidal metal solutions. *Ann Phys.*, Vol.25, No. 3, 377-445 (1908).
 37. Craig F. Bohren and Donald R. Huffman. *Absorption and Scattering of Light by Small Particles* (WILEY-VCH Verlag GmbH & Co. KGaA, Weinheim, 2004).
 38. P. B. Johnson and R. W. Christy. Optical Constants of the Noble Metals. *Phys. Rev. B*, Vol. 6, No. 12, p. 4370-4379 (1972).
 39. D. J. Barber and I. C. Freestone. An investigation of the origin of the colour of the Lycurgus cup by analytical transmission electron microscopy. *Archaeometry* Vol. 32, Iss. 1, p.33-45 (1990).
 40. I. Freestone, N. Meeks, M. Sax, and C. Higgitt. The Lycurgus Cup – A Roman Nanotechnology. *Gold Bulletin*, 40, Iss. 4, p.270-277 (2007).
 41. A. Ruivo, C. Gomes, A. Lima, M. L. Botelho, R. Melo, A. Belchior, A. P. Matos. Gold nanoparticles in ancient and contemporary ruby glass. *Journal of Cultural Heritage* vol. 9, e134-e137 (2008).
 42. M. Fleischmann, P. J. Hendra, A. J. McQuillan. Raman spectra of pyridine adsorbed at a silver electrode. *Chem. Phys. Lett.*, vol. 26, Iss. 2, p. 163-166 (1974).
 43. A. Otto, I. Mrozek, H. Grabhorn, and W. Akemann. Surface-enhanced Raman scattering. *J. Phys.: Condens. Matter*, vol. 4, p.1143-1212 (1992).
 44. C. V. Raman and K. S. Krishnan. A new type of secondary radiation. *Nature*, vol. 121, p. 501-502 (1928).
 45. S. Nie and S. R. Emory. Probing Single Molecules and Single Nanoparticles by

- Surface-Enhanced Raman Scattering. *Science* vol. 275, p.1102-1106 (1997).
46. H. Xu, E. J. Bjerneld, M. Käll, and L. Börjesson. Spectroscopy of Single Hemoglobin Molecules by Surface Enhanced Raman Scattering. *Phys. Rev. Lett.*, vol. 83, No. 21, p. 4357-4360 (1999).
 47. J. Aizpurua, G. W. Bryant, L. J. Richter, and F. J. García de Abajo. Optical properties of coupled metallic nanorods for field-enhanced spectroscopy. *Phys. Rev. B*. vol. 71, 235420 (2005).
 48. R. Bachelot, P. Gleyzes, and A. C. Boccara. Near field optical microscopy by local perturbation of a diffraction spot. *Microsc. Microanal. Microstruct.* vol. 5, p. 389-397 (1994).
 49. R. Bachelot, P. Gleyzes, and A. C. Boccara. Near-field optical microscope based on local perturbation of a diffraction spot. *Opt. Lett.* vol. 20, No. 18, p.1924-1926 (1995).
 50. M. S. Anderson. Locally enhanced Raman spectroscopy with an atomic force microscope. *Appl. Phys. Lett.* vol. 76, no. 21, p.3130-3132 (2000).
 51. T. Ichimura, N. Hayazawa, M. Hashimoto, Y. Inouye, and S. Kawata. Tip-Enhanced Coherent Anti-Stokes Raman Scattering for Vibrational Nanoimaging. *Phys. Rev. Lett.* vol. 92, no. 22, 220801 (2004).
 52. B. Pettinger, B. Ren, G. Picardi, R. Schuster, and G. Ertl. Nanoscale Probing of Adsorbed Species by Tip-Enhanced Raman Spectroscopy. *Phys. Rev. Lett.* vol. 92, no. 9, 096101 (2004).
 53. C. D. Geddes, and J. R. Lakowicz. Metal-Enhanced Fluorescence. *Journal of Fluorescence*, Vol. 12, No. 2, p. 121-129 (2002).
 54. K. Aslan, I. Gryczynski, J. Malicka, E. Matveeva, J. R Lakowicz, and C. D. Geddes. Metal-enhanced fluorescence: an emerging tool in biotechnology. *Curr. Opin. Biotechnol.*, 16, p. 55–62 (2005).
 55. Y. Zhang, K. Aslan, M. J. R. Prevote, and C. D. Geddes. Metal-enhanced *e-type* fluorescence. *Appl. Phys. Lett.*, Vol. 92, 013905 (2008).
 56. K. Aslan, J. R Lakowicz, and C. D Geddes. Plasmon light scattering in biology and medicine: new sensing approaches, visions and perspectives. *Curr. Opin. Chem. Biol.*, Vol. 9, Iss. 5, p. 538–544 (2005).
 57. M. D. Malinsky, K. L. Kelly, G. C. Schatz, and R. P. V. Duyne. Chain Length Dependence and Sensing Capabilities of the Localized Surface Plasmon Resonance of Silver Nanoparticles Chemically Modified with Alkanethiol Self-Assembled Monolayers. *J. Am. Chem. Soc.*, 123, p. 1471-1482 (2001).
 58. P. Bharadwaj, P. Anger, and L. Novotny. Nanoplasmonic enhancement of single-molecule fluorescence. *Nanotechnology* Vol. 18, 044017 (2007).
 59. J. Malicka, I. Gryczynski, J. R. Lakowicz. DNA hybridization assays using metal-enhanced fluorescence. *Biochem. Biophys. Res. Commun.* Vol. 306, Iss. 1, p. 213-218 (2003).
 60. A. K. Sharma, R. Jha, and B. D. Gupta. Fiber-Optic Sensors Based on Surface Plasmon Resonance: A Comprehensive Review. *IEEE SENSORS JOURNAL*, Vol. 7, No. 8, p.1118-1129 (2007).
 61. S. K. Srivastava, R. K. Verma, and B. D. Gupta. Theoretical modeling of a localized surface plasmon resonance based intensity modulated fiber optic refractive index sensor. *Appl. Opt.*, Vol. 48, No. 19, p.3796-3802 (2009).
 62. K. Mitsui, Y. Handa, and K. Kajikawa. Optical fiber affinity biosensor based on localized surface plasmon resonance. *Appl. Phys. Lett.*, Vol. 85, p. 4231-4233 (2004).
 63. S. Pillai, K. R. Catchpole, T. Trupke, and M. A. Green. Surface plasmon enhanced silicon solar cells. *J. Appl. Phys.* Vol. 101, 093105 (2007).
 64. K.R. Catchpole, and A. Polman. Plasmonic solar cells. *Opt. Express*, Vol. 16, No. 26, p. 21793-21800 (2008).

65. H. A. Atwater and A. Polman. Plasmonics for improved photovoltaic devices. *Nature Materials*, Vol. 9, p. 205–213 (2010).
66. P. Spinelli and A. Polman. Light Trapping in Thin Crystalline Si Solar Cells Using Surface Mie Scatterers. *IEEE J. Photovolt.*, Vol. 4, No. 2, p. 554-559 (2014).
67. B. Lamprecht, G. Schider, R. T. Lechner, H. Ditlbacher, J. R. Krenn, A. Leitner, and F. R. Aussenegg. Metal Nanoparticle Gratings: Influence of Dipolar Particle Interaction on the Plasmon Resonance. *Phys. Rev. Lett.*, Vol. 84, No. 20, p. 4721-4724 (2000).
68. Q.-H. Wei, K.-H. Su, S. Durant, and X. Zhang. Plasmon Resonance of Finite One-Dimensional Au Nanoparticle Chains. *Nano Lett.* Vol. 4, No. 6, p. 1067-1071 (2004).
69. N. Félidj, G. Laurent, J. Aubard, G. Lévi, A. Hohenau, J. R. Krenn, and F. R. Aussenegg. Grating-induced plasmon mode in gold nanoparticle arrays. *J. Chem. Phys.*, Vol. 123, 221103 (2005).
70. V. G. Kravets, F. Schedin, and A. N. Grigorenko. Extremely Narrow Plasmon Resonances Based on Diffraction Coupling of Localized Plasmons in Arrays of Metallic Nanoparticles. *Phys. Rev. Lett.*, Vol. 101, 087403 (2008).
71. E. M. Hicks, S. Zou, G. C. Schatz, K. G. Spears, R. P. Van Duyne, L. Gunnarsson, T. Rindzevicius, B. Kasemo, and M. Käll. Controlling Plasmon Line Shapes through Diffractive Coupling in Linear Arrays of Cylindrical Nanoparticles Fabricated by Electron Beam Lithography. *Nano Lett.*, Vol. 5, No. 6, p. 1065-1070 (2005).
72. S. K. Ghosh and T. Pal. Interparticle Coupling Effect on the Surface Plasmon Resonance of Gold Nanoparticles: From Theory to Applications. *Chem. Rev.*, Vol. 107, p. 4797–4862 (2007).
73. S. A. Maier, P. G. Kik, and H. A. Atwater. Observation of coupled plasmon-polariton modes in Au nanoparticle chain waveguides of different lengths: Estimation of waveguide loss. *Appl. Phys. Lett.*, Vol. 81, No. 9, p. 1714-1716 (2002).
74. S. A. Maier, P. G. Kik, and H. A. Atwater. Optical pulse propagation in metal nanoparticle chain waveguides. *Phys. Rev. B*, Vol. 67, 205402 (2003).
75. S. A. Maier, P. G. Kik, H. A. Atwater, S. Meltzer, E. Harel, B. E. Koel, and A. A. G. Requicha. Local detection of electromagnetic energy transport below the diffraction limit in metal nanoparticle plasmon waveguides. *Nature Materials*, Vol. 2, p. 229-232 (2003).
76. K. B. Crozier, E. Togan, E. Simsek, and T. Yang. Experimental measurement of the dispersion relations of the surface plasmon modes of metal nanoparticle chains. *Opt. Express*, Vol. 15, No. 26, p. 17482-17493 (2007).
77. A. F. Koenderink and A. Polman. Complex response and polariton-like dispersion splitting in periodic metal nanoparticle chains. *Phys. Rev. B*, Vol. 74, 033402 (2006).
78. V. A. Markel and A. K. Sarychev. Propagation of Surface Plasmons in Ordered and Disordered Chains of Metal Nanospheres. *Phys. Rev. B*, Vol. 75, 085426 (2007).
79. H. Cao. Review on latest developments in random lasers with coherent feedback. *J. Phys. A: Math. Gen.* Vol. 38, p. 10497–10535 (2005).
80. C. Mateo-Segura, C. Simovski, G. Goussetis, and S. Tretyakov. Subwavelength resolution for horizontal and vertical polarization by coupled arrays of oblate nanoellipsoids. *Opt. Lett.*, Vol. 34, Iss. 15, p. 2333-2335 (2009).
81. P. Alitalo, C. Simovski, A. Viitanen, and S. Tretyakov. Near-field enhancement and subwavelength imaging in the optical region using a pair of two-dimensional arrays of metal nanospheres. *Phys. Rev. B*, Vol. 74, p. 235425 (2006).
82. S. Steshenko, F. Capolino, P. Alitalo, and S. Tretyakov. Effective model and investigation of the near-field enhancement and subwavelength imaging properties of multilayer arrays of plasmonic nanospheres. *Phys. Rev. E*, Vol. 84, 016607 (2011).
83. R. Quidant, C. Girard, Jean-Claude Weeber, and A. Dereux. Tailoring the transmittance of integrated optical waveguides with short metallic nanoparticle chains. *Phys. Rev. B*, Vol. 69, 085407 (2004).

84. W. H. Weber and G. W. Ford. Propagation of optical excitations by dipolar interactions in metal nanoparticle chains. *Phys. Rev. B* Vol. 70, 125429 (2004).
85. R. Waele, A. F. Koenderink, and A. Polman. Tunable Nanoscale Localization of Energy on Plasmon Particle Arrays. *Nano. Lett.*, Vol. 7, No. 7, p. 2004-2008 (2007).
86. J. B. Pendry. Negative Refraction Makes a Perfect Lens. *Phys. Rev. Lett.*, Vol. 85, No. 18, p. 3966-3969 (2000).
87. R. A. Shelby, D. R. Smith, S. Schultz. Experimental Verification of a Negative Index of Refraction. *Science* Vol. 292, p. 77-79 (2001).
88. S. Linden, C. Enkrich, M. Wegener, J. Zhou, T. Koschny, C. M. Soukoulis. Magnetic Response of Metamaterials at 100 Terahertz. *Science* Vol. 306, p. 1351-1353 (2004).
89. D. R. Smith, J. B. Pendry, M. C. K. Wiltshire. Metamaterials and Negative Refractive Index. *Science* Vol. 305, p. 788-792 (2004).
90. N. Fang, H. Lee, C. Sun, X. Zhang. Sub-Diffraction-Limited Optical Imaging with a Silver Superlens. *Science* Vol. 308, p. 534-537 (2005).
91. V. M. Shalaev, W. Cai, U. K. Chettiar, H. K. Yuan, A. K. Sarychev, V. P. Drachev, and A. V. Kildishev. Negative index of refraction in optical metamaterials. *Opt. Lett.*, Vol. 30, No. 24, p.3356-3358 (2005).
92. D. W. Pohl. "Near Field Optics Seen as an Antenna Problem", in *Near-Field Optics: Principles and Applications*, X. Zhu and M. Ohtsu (eds.), p. 9-21, World Scientific, Singapore (2000).
93. J. Wessel. Surface-enhanced optical microscopy. *J. Opt. Soc. Am. B*, Vol. 2, Iss. 9, p. 1538-1541 (1985).
94. P. Bharadwaj, B. Deutsch, and L. Novotny. Optical Antennas. *Adv. Opt. Photon.* Vol. 1, Iss. 3, p. 438-483 (2009).
95. P. Mülschlegel, H.-J. Eisler, O. J. F. Martin, B. Hecht, and D. W. Pohl. Resonant Optical Antennas. *Science* Vol. 308, p. 1607-1609 (2005).
96. L. Novotny. Effective Wavelength Scaling for Optical Antennas. *Phys. Rev. Lett.* Vol. 98, 266802 (2007).
97. R. D. Grober, R. J. Schoelkopf, and D. E. Prober. Optical antenna: Towards a unity efficiency near-field optical probe. *Appl. Phys. Lett.* Vol. 70, No. 11, p. 1354- 1356 (1997).
98. K. B. Crozier, A. Sundaramurthy, G. S. Kino, and C. F. Quate. Optical antennas: Resonators for local field enhancement. *J. Appl. Phys.*, Vol. 94, No. 7, p. 4632-4642 (2003).
99. D. P. Fromm, A. Sundaramurthy, P. J. Schuck, G. Kino, and W. E. Moerner. Gap-Dependent Optical Coupling of Single "Bowtie" Nanoantennas Resonant in the Visible. *Nano. Lett.*, Vol. 4, No. 5, p. 957-961 (2004).
100. P. J. Schuck, D. P. Fromm, A. Sundaramurthy, G. S. Kino, and W. E. Moerner. Improving the Mismatch between Light and Nanoscale Objects with Gold Bowtie Nanoantennas. *Phys. Rev. Lett.*, Vol. 94, 017402 (2005).
101. J. N. Farahani, D. W. Pohl, H.-J. Eisler, and B. Hecht. Single Quantum Dot Coupled to a Scanning Optical Antenna: A Tunable Superemitter. *Phys. Rev. Lett.*, Vol. 95, 017402 (2005).
102. T. Ishi, J. Fujikata, K. Makita, T. Baba, and K. Ohashi. Si Nano-Photodiode with a Surface Plasmon Antenna. *Jpn. J. Appl. Phys.*, Vol. 44, No. 12, L 364–L 366 (2005).
103. H. Gersen, M. F. García-Parajó, L. Novotny, J. A. Veerman, L. Kuipers, and N. F. van Hulst. Influencing the Angular Emission of a Single Molecule. *Phys. Rev. Lett.*, Vol. 85, No. 25, p. 5312-5315 (2000).
104. S. Kühn, U. Håkanson, L. Rogobete, and V. Sandoghdar. Enhancement of Single-Molecule Fluorescence Using a Gold Nanoparticle as an Optical Nanoantenna. *Phys. Rev. Lett.*, Vol. 97, 017402 (2006).

105. L. Rogobete, F. Kaminski, M. Agio, and V. Sandoghdar. Design of plasmonic nanoantennae for enhancing spontaneous emission. *Opt. Lett.* Vol. 32, No. 12, 1623-1625 (2007).
106. R. M. Bakker, H. K. Yuan, Z. Liu, V. P. Drachev, A. V. Kildishev, V. M. Shalaev, R. H. Pedersen, S. Gresillon, A. Boltasseva. Enhanced localized fluorescence in plasmonic nanoantennae. *Appl. Phys. Lett.*, Vol. 92, 043101(2008).
107. A Mohammadi, V Sandoghdar, and M Agio. Gold nanorods and nanospheroids for enhancing spontaneous emission. *New J. Phys.* 10, 105015 (2008).
108. A. Devilez, B. Stout, and N. Bonod. Compact Metallo-Dielectric Optical Antenna for Ultra Directional and Enhanced Radiative Emission. *ACS Nano*, Vol.4, No.6, 3390-3396 (2010).
109. H. G. Frey, F. Keilmann, A. Kriele, and R. Guckenberger. Enhancing the resolution of scanning near-field optical microscopy by a metal tip grown on an aperture probe. *Appl. Phys. Lett.*, Vol. 81, No. 26, 5030-5032 (2002).
110. P. Anger, P. Bharadwaj, and L. Novotny. Enhancement and Quenching of Single-Molecule Fluorescence. *Phys. Rev. Lett.*, Vol. 96, 113002(2006).
111. O. L. Muskens, V. Giannini, J. A. Sánchez-Gil, and J. Gómez Rivas. Strong Enhancement of the Radiative Decay Rate of Emitters by Single Plasmonic Nanoantennas. *Nano Lett.*, Vol. 7, No. 9, 2871-2875 (2007).
112. R. M Bakker, V. P Drachev, Z. Liu, H. K. Yuan, R. H Pedersen, A. Boltasseva, J. Chen, J. Irudayaraj, A. V Kildishev, and V. M Shalaev. Nanoantenna array-induced fluorescence enhancement and reduced lifetimes. *New J. Phys.* 10, 125022 (2008).
113. N. Engheta. Circuits with Light at Nanoscales: Optical Nanocircuits Inspired by Metamaterials. *Science*, vol. 317, no. 5845, p. 1698-1702 (2007).
114. A. Politi, M. J. Cryan, J. G. Rarity, S. Yu, and J. L. O'Brien. Silica-on-Silicon Waveguide Quantum Circuits. *Science*, vol. 320, p. 646-649 (2008).
115. T. Gerrits, N. Thomas-Peter, J. C. Gates, A. E. Lita, B. J. Metcalf, B. Calkins, N. A. Tomlin, A. E. Fox, A. L. Linares, J. B. Spring, N. K. Langford, R. P. Mirin, P. G. R. Smith, I. A. Walmsley, and S. W. Nam. On-chip, photon-number-resolving, telecommunication-band detectors for scalable photonic information processing. *Phys. Rev. A* vol. 84, 060301(R) (2011).
116. N. Engheta, A. Salandrino, and A. Alù. Circuit Elements at Optical Frequencies: Nanoinductors, Nanocapacitors, and Nanoresistors. *Phys. Rev. Lett.*, vol. 95, 095504 (2005).
117. A. F. Koenderink, A. Alù, A. Polman. Nanophotonics: Shrinking light-based technology. *Science*, vol. 348, no. 6234, p. 516-521 (2015).
118. T. H. Taminiau, R. J. Moerland, F. B. Segerink, L. Kuipers, and N. F. van Hulst. $\lambda/4$ Resonance of an Optical Monopole Antenna Probed by Single Molecule Fluorescence. *Nano. Lett.*, Vol. 7, No. 1, p. 28-33 (2007).
119. T. H. Taminiau, F. D. Stefani, F. B. Segerink, and N. F. Van Hulst. Optical antennas direct single-molecule emission. *Nature Photon.* Vol. 2, p. 234-237 (2008).
120. C. A. Balanis. ANTENNA THEORY ANALYSIS AND DESIGN 3rd edition, p.577 (A John Wiley & Sons, Inc., Hoboken, N.J. 2005).
121. Peter P. Vezic, Yagi Antenna Design. NBS TECHNICAL NOTE 688 (1976).
122. Holger F. Hofmann, Terukazu Kosako, and Yutaka Kadoya. Design parameters for a nano-optical Yagi-Uda antenna. *New J. Phys.* 10, p. 217 (2007).
123. Terukazu Kosako, Yutaka Kadoya and Holger F. Hofmann. Directional control of light by a nano-optical Yagi-Uda antenna. *Nature Photon.*, Vol. 4, p. 312-315 (2010).
124. J. Li, A. Salandrino, and N. Engheta. Shaping light beams in the nanometer scale: A Yagi-Uda nanoantenna in the optical domain. *Phys. Rev. B*, vol. 76, 245403 (2007).
125. J. Li, A. Salandrino, and N. Engheta. Optical spectrometer at the nanoscale using optical

- Yagi-Uda nanoantennas. *Phys. Rev. B*, vol. 79, 195104 (2009).
126. 新井宏之, “新アンテナ工学”, 総合電子出版社 (1996).
 127. J. A. Osborn. Demagnetizing Factors of the General Ellipsoid. *Phys. Rev.*, Vol. 67, No. 11, p. 351-357 (1945).
 128. I. Maximov, E.-L. Sarwe, M. Beck, K. Deppert, M. Graczyk, M.H. Magnusson, L. Montelius. Fabrication of Si-based nanoimprint stamps with sub-20 nm features. *Microelectronic Engineering* 61–62 (2002) 449–454.
 129. L. An, Y. Zheng, K. Li, P. Luo, and Y. Wu. Nanometer metal line fabrication using a ZEP520/50 K PMMA bilayer resist by e-beam lithography. *J. Vac. Sci. Technol. B* vol. 23 1603 (2005).
 130. D. B. Rutledge, M. S. Muha. Imaging Antenna Arrays. *IEEE Trans. Antennas Propagat.* , vol. AP-30, No. 4, p.535-540 (1982).
 131. Akira Yoshida, Terukazu Kosako, Yutaka Kadoya, and Holger F. Hofmann. Radiation pattern of a single optical Yagi-Uda antenna. The Japan Society of Applied Physics, The 71th Fall meeting, 17p-NJ-1 (in Japanese) (2010).
 132. A. G. Curto, G. Volpe, T. H. Taminiau, M. P. Kreuzer, R. Quidant, and N. F. van Hulst. Unidirectional Emission of a Quantum Dot Coupled to a Nanoantenna. *Science* vol. 329, p. 930 (2010).
 133. Kaori Yanazawa, Yusuke Tobisu, Satoshi Maeda, Holger F. Hofmann, and Yutaka Kadoya. Radiation and receiving gain of nano-optical Yagi-Uda antenna embedded in slab dielectric waveguide. CLEO QF2A8, San Jose, USA (2013).
 134. D. Dregely, K. Lindfors, M. Lippitz, N. Engheta, M. Totzeck, and H. Giessen. Imaging and steering an optical wireless nanoantenna link. *Nat. Commun.* 5:4354 doi: 10.1038 / ncomms 5354 (2014).
 135. L. Tong, T. Pakizeh, L. Feuz, and A. Dmitriev. Highly directional bottom-up 3D nanoantenna for visible light. *Sci. Rep.* 3, 2311; DOI:10.1038/srep02311 (2013).
 136. D. Dregely, R. Taubert, J. Dorfmueller, R. Vogelgesang, K. Kern, and H. Giessen. 3D optical Yagi-Uda nanoantenna array. *Nat. Commun.* 2:267 doi: 10.1038/ncomms1268 (2011).
 137. F. B. Arango, A. Kwadrin, and A. F. Koenderink. Plasmonic Antennas Hybridized with Dielectric Waveguides. *ACS Nano*, vol. 6, No. 11, p. 10156–10167 (2012).
 138. N. Yu, P. Genevet, M. A. Kats, F. Aieta, Jean-Philippe Tetienne, F. Capasso, Z. Gaburro. Light Propagation with Phase Discontinuities: Generalized Laws of Reflection and Refraction. *SCIENCE* Vol. 334, p. 333 (2011).

Appendix I Mathematica program codes

Mathematica (Wolfram Research, Inc.) was used for the calculation of the coupled dipole model in this work. The program codes were as follows.

- * Estimation of the detuning and the material losses of antenna element by fitting the transmission spectra of each element with dipole model (Table 5.2)
- * 2-element coupled dipole model (Fig. 4.5, Fig. 4.8, Fig. 5.14, Fig. 5.15)
- * 5-element coupled dipole model (Reflector x 1, Director x 3, Feed x1, Fig. 5.16, Fig. 5.28)
- * Emission of dipole placed at the refractive index interface (Fig. 5.13).
- * Estimating the effect of the interparticle distance on the resonant frequency/wavelength and the line width of the emission spectra (Fig. 3.1).

***Estimation of the material-losses and the detuning value from the transmission spectra of each element used in the antennas. Input field was polarized parallel to the longer axis of the element. (Table 5.2)**

(*Fitting Equation for the dielectric constant of the gold [38] was expressed as the following equation $\epsilon[w]$. Here the unit of “ w ” is eV. *)

$$\begin{aligned} \epsilon[w] := & 2.85 - \frac{(8.8)^2}{w(w + i0.066)} + \frac{0.45(4.35)^2}{(6.4)^2 - w^2 - i0.33} + \frac{0.45(4.35)^2}{(6.2)^2 - w^2 - iw0.55} \\ & + \frac{0.25(4.35)^2}{(5.8)^2 - w^2 - iw0.55} + \frac{0.15(4.35)^2}{(5.6)^2 - w^2 - iw0.55} + \frac{0.15(4.35)^2}{(5.4)^2 - w^2 - iw0.5} \\ & + \frac{0.15(4.35)^2}{(5.2)^2 - w^2 - iw0.55} + \frac{0.15(4.35)^2}{(5.0)^2 - w^2 - iw0.5} + \frac{0.16(4.35)^2}{(4.8)^2 - w^2 - iw0.5} \\ & + \frac{0.16(4.35)^2}{(4.6)^2 - w^2 - iw0.45} + \frac{0.18(4.35)^2}{(4.4)^2 - w^2 - iw0.45} + \frac{0.16(4.35)^2}{(4.2)^2 - w^2 - iw0.35} \\ & + \frac{0.15(4.35)^2}{(4.0)^2 - w^2 - iw0.35} + \frac{0.135(4.35)^2}{(3.8)^2 - w^2 - iw0.3} + \frac{0.135(4.35)^2}{(3.6)^2 - w^2 - iw0.3} \\ & + \frac{0.135(4.35)^2}{(3.4)^2 - w^2 - iw0.34} + \frac{0.135(4.35)^2}{(3.2)^2 - w^2 - iw0.34} + \frac{0.14(4.35)^2}{(3.0)^2 - w^2 - iw0.34} \\ & + \frac{0.135(4.275)^2}{(2.8)^2 - w^2 - iw0.33} + \frac{0.135(4.275)^2}{(2.6)^2 - w^2 - iw0.36} \end{aligned}$$

(* definition of material losses given by Eq. (2.38) *)

$$\text{loss}[V_ , \lambda_ , n_] := \frac{3 \left(\frac{\lambda \times 10^{-9}}{n} \right)^3}{4 \pi^2 V} \frac{\text{Im} \left[\frac{\varepsilon[1239.8/\lambda]}{n^2} \right]}{\text{Abs} \left[\frac{\varepsilon[1239.8/\lambda]}{n^2} - 1 \right]^2}$$

(* definition of detuning given by Eq. (2.39) *)

$$\text{detune}[V_ , n_ , N_ , \lambda_] := - \frac{3 \left(\frac{\lambda \times 10^{-9}}{n} \right)^3}{4 \pi^2 V} \left(N + \frac{\text{Re} \left[\frac{\varepsilon[1239.8/\lambda]}{n^2} - 1 \right]}{\text{Abs} \left[\frac{\varepsilon[1239.8/\lambda]}{n^2} - 1 \right]^2} \right)$$

(* polarizability α given by Eq. (5.1) *)

$$\alpha[n_ , V_ , N_ , \lambda_] := \frac{\left(\frac{\varepsilon[1239.8/\lambda]}{n^2} - 1 \right) V}{1 + N \left(\frac{\varepsilon[1239.8/\lambda]}{n^2} - 1 \right) - i \left(\frac{\varepsilon[1239.8/\lambda]}{n^2} - 1 \right) \frac{4 \pi^2 V}{3 \left(\frac{\lambda \times 10^{-9}}{n} \right)^3}}$$

(* absorption coefficient for polarizability α [37] *)

$$\text{cabsorp}[n_ , V_ , N_ , \lambda_] := \frac{2 \pi}{\lambda \times 10^{-9}} \text{Im}[\alpha[n, V, N, \lambda]]$$

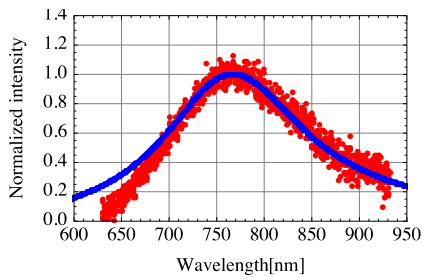
(* estimation for reflector *)

```
Import [ "l=125nm_p.txt", "Table" ];
```

```
data1 = %;
```

```
data2 = Table [ { { \lambda, \frac{\text{Im}[\alpha[1.44, 2.5 \times 10^{-22}, 0.09, \lambda]]}{\text{Im}[\alpha[1.44, 2.5 \times 10^{-22}, 0.09, 770]]} }, { \lambda, 500, 1100, 1 } } ];
```

```
ListPlot [ { data1, data2 }, PlotStyle -> { Red, Blue }, FrameLabel -> { "Wavelength[nm]", "Normalized intensity" } ]
```



```
{loss[2.5*10-22, 662, 1.44], detune[2.5*10-22, 1.44, 0.09, 662]}
```

```
{0.284854, 1.08951}
```

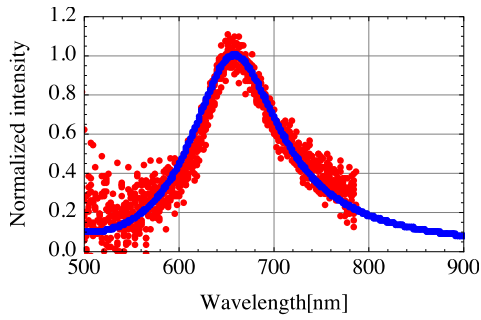
(* estimation for feed*)

```
Import [ "l=106nm_p.txt", "Table" ];
```

```
data1 = %;
```

```
data2 = Table [ { { \lambda, \frac{\text{Im}[\alpha[1.44, 50*50*75*10^{-27}, 0.135, \lambda]]}{\text{Im}[\alpha[1.44, 50*50*75*10^{-27}, 0.135, 655]]} }, { \lambda, 500, 1100, 1 } } ];
```

```
ListPlot [ { data1, data2 }, PlotStyle -> { Red, Blue } ]
```



```
{loss[50*50*75*10-27, 662, 1.44], detune[50*50*75*10-27, 1.44, 0.135, 662]}
{0.379805, -0.319304}
```

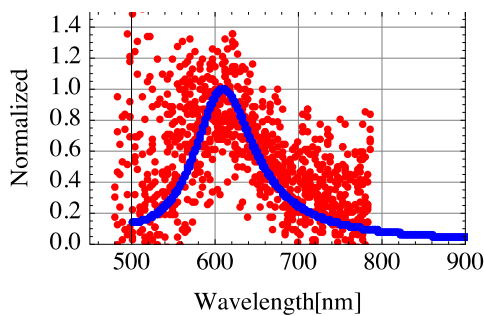
(* estimation for director *)

```
Import [ "l=75nm_p.txt", "Table" ];
```

```
data1 = %;
```

```
data2 = Table [ { λ,  $\frac{\text{Im}[\alpha[1.44, 50*50*65*10^{-27}, 0.173, \lambda]]}{\text{Im}[\alpha[1.44, 50*50*65*10^{-27}, 0.173, 610]]}$  }, { λ, 500, 1100, 1} ];
```

```
ListPlot [ {data1, data2}, PlotStyle-> {Red, Blue} ]
```



```
{loss[50*50*65*10-27, 662, 1.44], detune[50*50*65*10-27, 1.44, 0.173, 662]}
{0.438237, -2.09497}
```

*2-element coupled dipole model (Fig. 4.5, Fig. 4.8, Fig. 5.14, Fig. 5.15)

xr (*reflector(or director)-feed distance*),

wr (*detuning of reflector(or director)*), mr (*material loss of reflector(or director)*),

wf (*detuning of feed*), mf (*material loss of feed*)

$$\text{dipole}[x_] := -\frac{3}{2} \frac{1}{x^3} (i + x - ix^2) e^{ix}$$

$$\text{Solve} \left[\left\{ \text{ar} - \frac{1}{1.0 + \text{mr} - \text{wr} i} \left(\frac{1}{1 + \text{mf} - \text{wf} i} \text{dipole}[\text{Abs}[\text{xr}]] \right) == 0 \right\}, \{\text{ar}\} \right];$$

```
ar /. %;
```

```
ar[xr_, wr_, mr_, wf_, mf_] = %[[1]];
```

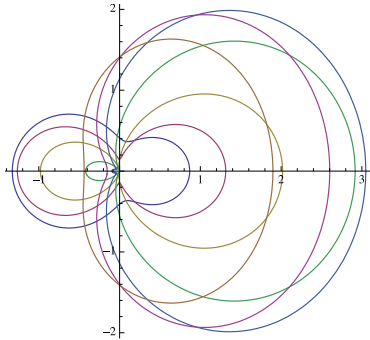

$$f[\theta, xr, wr, mr, wf, mf] := \left(\text{Abs} \left[1 + \frac{\text{ar}[xr,wr,mr,wf,mf]}{\text{Abs}\left[\frac{1}{1+mf-wf i}\right]} \text{Exp}[-i xr \text{Cos}[\theta]] \right] \right)^2 ;$$

Needs["Graphics 'Graphics'"];

(*calculation for Fig. 4.5*)

xr = -1.5

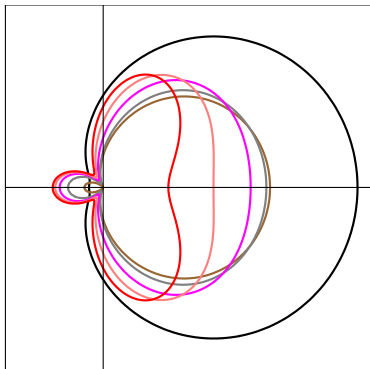
PolarPlot[f[θ, xr, -2.0, 0, 0,0], f[θ, xr, -1.0, 0, 0,0], f[θ, xr, -0.5, 0, 0,0], f[θ, xr, 0, 0, 0,0],
f[θ, xr, 0.5, 0, 0,0], f[θ, xr, 1.0, 0, 0,0], f[θ, xr, 2.0, 0, 0,0], {θ, -Pi, Pi}]



(*calculation for Fig. 4.8*)

wr := 0

PolarPlot[f[θ, -1.0, wr, 0, 0,0], f[θ, -1.4, wr, 0, 0,0], f[θ, -1.8, wf, 0, 0,0], f[θ, -2.2, wf, 0, 0,0],
f[θ, -2.6, wr, 0, 0,0], f[θ, -3.0, wr, 0, 0,0], {θ, -Pi, Pi}]



(*calculation for Fig. 5.14*)

xr := -1.708 (*position of reflector from feed, $n=1.44$, $r=125\text{nm}$, $\lambda_{in}=662\text{nm}$ *)

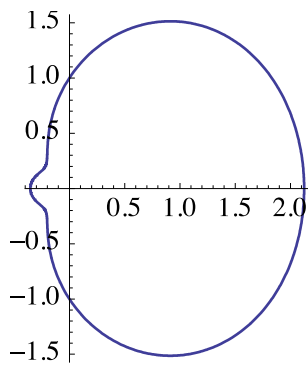
wr := 1.0895 (*detuning of reflector*)

mr := 0.285 (*material loss of reflector*)

wf := -0.3193 (*detuning of feed*)

mf := 0.3798 (*material loss of feed*)

PolarPlot[f[θ, xr, wr, mr, wf, mf], {θ, -Pi, Pi}]



(*calculation for Fig. 5.15*)

$xr := 1.708$ (*position of director from feed, $n=1.44$, $r=125\text{nm}$, $\lambda_{in}=662\text{nm}$ *)

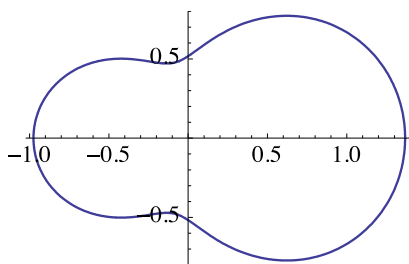
$wr := -2.095$ (*detuning of director*)

$mr := 0.438$ (*material loss of director*)

$wf := -0.3193$ (*detuning of feed*)

$mf := 0.3798$ (*material loss of feed*)

`PolarPlot[f[θ, xr, wr, mr, wf, mf], {θ, -Pi, Pi}]`



***5-element coupled dipole model (Reflector x 1, Director x 3, Feed x 1, Fig. 5.16, Fig. 5.28)**

(* Emission pattern of 5-element Yagi-Uda antenna, consisting of 1 x Feed, 1 x Reflector, 3 x directors. The parameters are material losses, detuning, and geometry of each element. The calculation for obtaining Fig. 5.16 is shown*)

$xr := -1.7084$ (*reflector-feed distance= $125[\text{nm}] \times 2\pi/(662[\text{nm}]/1.44)$ *)

$xa := 2.0501$ (*director-feed distance= $150[\text{nm}] \times 2\pi/(662[\text{nm}]/1.44)$ *)

$wr := 1.0895$ (*detuning of reflector*)

$mr := 0.285$ (*material loss of reflector*)

$wd := -2.095$ (*detuning of director*)

$md := 0.438$ (*material loss of director*)

$wf := -0.3193$ (*detuning of feed*)

$mf := 0.3798$ (*material loss of feed*)

$$\text{dipole}[x_] := -\frac{3}{2} \frac{1}{x^3} (i + x - ix^2) e^{ix}$$

$$\text{Solve} \left[\left\{ \begin{aligned} & \text{ar} - \frac{1}{1.0 + \text{mr} - \text{wr} i} \left(\frac{1}{1 + \text{mf} - \text{wf} i} \text{dipole}[\text{Abs}[\text{xr}]] + \text{dipole}[\text{xa} + \text{Abs}[\text{xr}]] \right) \text{a1} \\ & + \text{dipole}[2\text{xa} + \text{Abs}[\text{xr}]] \text{a2} + \text{dipole}[3\text{xa} + \text{Abs}[\text{xr}]] \text{a3} \right) == 0, \\ & \text{a1} - \frac{1}{1.0 + \text{md} - \text{wd} i} \left(\text{dipole}[\text{xa} + \text{Abs}[\text{xr}]] \text{ar} + \frac{1}{1 + \text{mf} - \text{wf} i} \text{dipole}[\text{xa}] \right. \\ & \left. + \text{dipole}[\text{xa}] \text{a2} + \text{dipole}[2\text{xa}] \text{a3} \right) == 0, \\ & \text{a2} - \frac{1}{1.0 + \text{md} - \text{wd} i} \left(\text{dipole}[2 \text{xa} + \text{Abs}[\text{xr}]] \text{ar} + \frac{1}{1 + \text{mf} - \text{wf} i} \text{dipole}[2 \text{xa}] \right. \\ & \left. + \text{dipole}[\text{xa}] \text{a1} + \text{dipole}[\text{xa}] \text{a3} \right) == 0, \\ & \text{a3} - \frac{1}{1.0 + \text{md} - \text{wd} i} \left(\text{dipole}[3 \text{xa} + \text{Abs}[\text{xr}]] \text{ar} + \frac{1}{1 + \text{mf} - \text{wf} i} \text{dipole}[3 \text{xa}] \right. \\ & \left. + \text{dipole}[2 \text{xa}] \text{a1} + \text{dipole}[\text{xa}] \text{a2} \right) == 0, \end{aligned} \right\}, \{\text{ar}, \text{a1}, \text{a2}, \text{a3}\}];$$

{ar, a1, a2, a3} /. %;

%[[1]];

ar = %[[1]];

a1 = %%%[[2]];

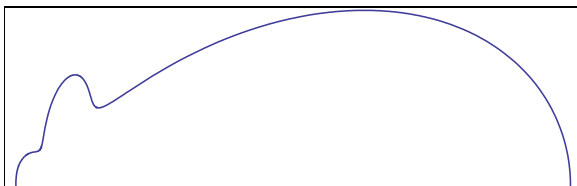
a2 = %%%%[[3]];

a3 = %%%%%[[4]];

$$f[\theta_] := \left(\text{Abs} \left[1 + \frac{\text{ar}}{\text{Abs} \left[\frac{1}{1 + \text{mf} - \text{wf} i} \right]} \text{Exp}[-i \text{xr} \text{Cos}[\theta]] + \frac{\text{a1}}{\text{Abs} \left[\frac{1}{1 + \text{mf} - \text{wf} i} \right]} \text{Exp}[-i \text{xa} \text{Cos}[\theta]] \right. \right. \\ \left. \left. + \frac{\text{a2}}{\text{Abs} \left[\frac{1}{1 + \text{mf} - \text{wf} i} \right]} \text{Exp}[-i 2 \text{xa} \text{Cos}[\theta]] + \frac{\text{a3}}{\text{Abs} \left[\frac{1}{1 + \text{mf} - \text{wf} i} \right]} \text{Exp}[-i 3 \text{xa} \text{Cos}[\theta]] + \right] \right)^2$$

Needs["Graphics 'Graphics'"];

PolarPlot[f[θ], {θ, 0, Pi}]



***Dipole model at the index interface [130] (Fig. 5.13, Fig. 5.17)**

Incident field; TE-plane, Output field; H-plane, n_1 ; refractive index of medium, n_2 ; refractive index of air, and $n = n_1/n_2$.

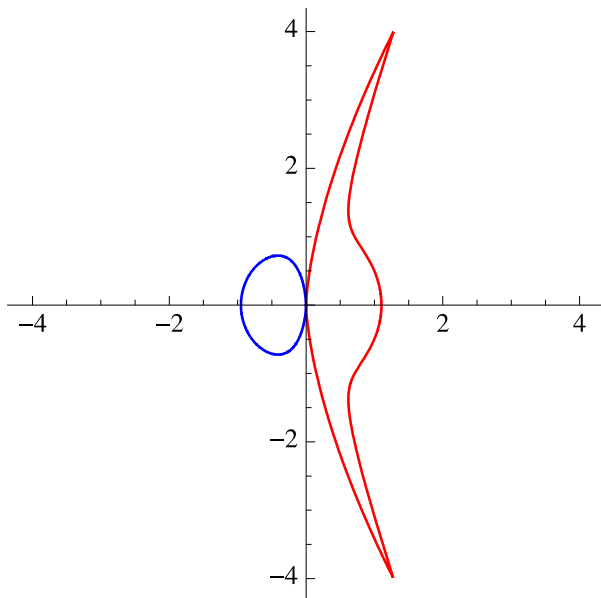
(* H-plane, emission to the air *)

$$fah[\theta_-, n_-] := 4 \left(\frac{\cos[\theta]}{\cos[\theta] + \sqrt{n^2 - (\sin[\theta])^2}} \right)^2$$

(* H-plane, emission to the dielectric *)

$$fdh[\theta_-, n_-] := 4n \left(\frac{\cos[\theta]}{\text{Abs} \left[\cos[\theta] + \sqrt{\left(\frac{1}{n}\right)^2 - (\sin[\theta])^2} \right]} \right)^2$$

`PolarPlot [{fdh [θ, 1.05], -fah[θ, 1.05]}, {θ, -π/2, π/2}, PlotStyle → {Red, Blue}]`



***Calculation results of FDTD for dipole emission at the index interface (Fig. 5.17)**

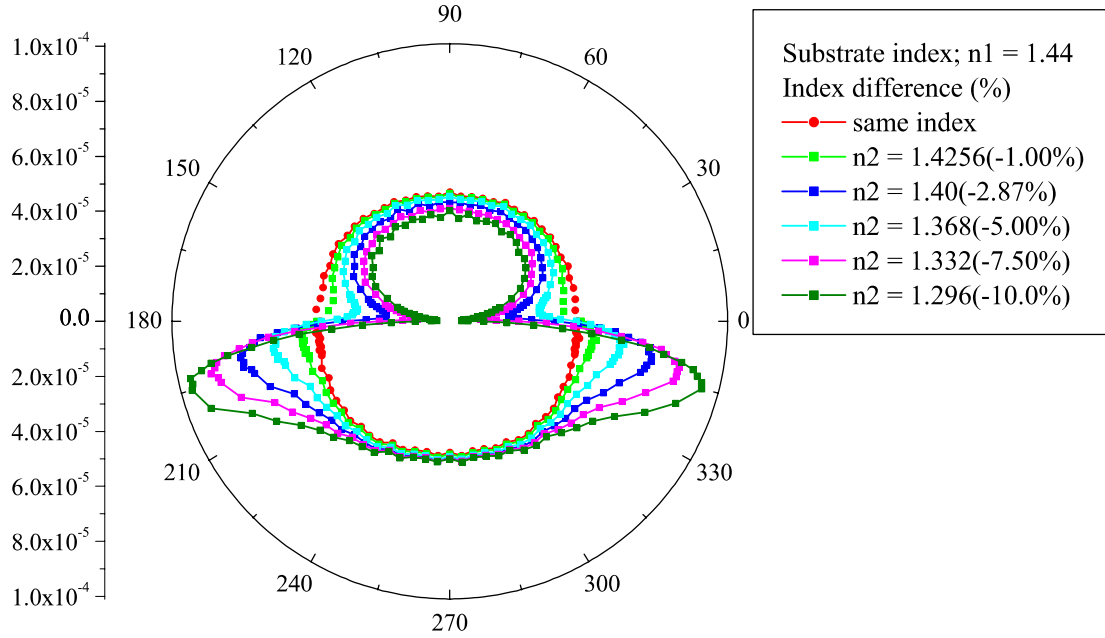


Fig. A: Prediction based on the FDTD method in the case that only one Feed element was set at the interface of the different index medium. The range between 0° and 180° was assumed as the lower index medium, and the range between 180° and 360° was assumed as the higher index medium.

***Effect of the interparticle interaction on the resonant frequency and the line width. (Fig. 3.1)**

The amount of material losses were assumed as $\gamma_{\text{mat}} = 1.0$, and input field was $E_{\text{in}} = 1.0$. The electric field amplitude of center elements was a_c , all elements interacted with each other.

$$\text{dipole}[x_] := -\frac{3}{2} \frac{1}{x^3} (i + x - ix^2) e^{ix}$$

$$\text{Solve} \left[\left\{ a1 - \frac{1}{2.0 - w i} (1 + \text{dipole}[xa] a_c + \text{dipole}[2 xa] a2) == 0, \right. \right.$$

$$a_c - \frac{1}{2.0 - w i} (1 + \text{dipole}[xa] a1 + \text{dipole}[xa] a2) == 0, \left. \right.$$

$$a2 - \frac{1}{2.0 - w i} (1 + \text{dipole}[xa] a_c + \text{dipole}[2 xa] a1) == 0, \left. \right\}, \{a_c, a1, a2\}];$$

{a_c, a1, a2} /. %;

```

%[[1]];
ac[ xa_, w_] = %[[1]];
a1[ xa_, w_] = %%[[2]];
a2[ xa_, w_] = %%%[[3]];

f[xa_, w_,  $\theta$ _] := (Abs[ac[xa, w] + a1[xa, w] Exp[ i xa Cos[ $\theta$ ]] + a2[xa, w] Exp[-i xa Cos[ $\theta$ ]]])2

(* estimation of resonant detuning value shift  $w = (\omega - \omega_0)/\Gamma_0$  , and FWHM shift of resonant
spectra  $\Delta\omega/\Gamma_0$ *)
xa=1.0;

FindMaximum [ f [xa, w,  $\frac{\pi}{2}$ ], {w, -6, 6} ] (* calculation for resonant detuning value *)

Plot [ f [xa, w,  $\frac{\pi}{2}$ ] -  $\frac{\%[[1]]}{2}$ , {w, -6, 6} ]

FindRoot [ f [xa, w,  $\frac{\pi}{2}$ ] -  $\frac{\%[[1]]}{2}$ , {w, -2.0} ];
{w} /. %;

FindRoot [ f [xa, w,  $\frac{\pi}{2}$ ] -  $\frac{\%[[1]]}{2}$ , {w, 2.0} ];
{w} /. %;

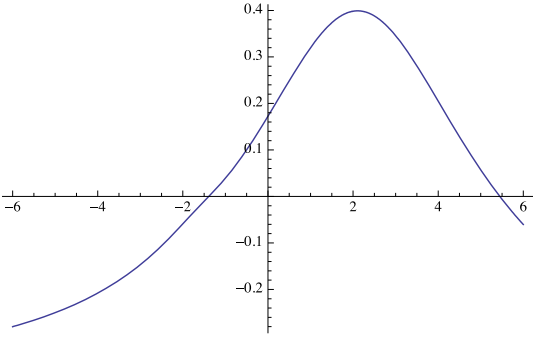
%[[1]] - (%%%[[1]]) (* calculation for FWHM *)

%%%%%%%%%%[[2]];

{w} /. %;

%[[1]]
Out[] = {0.798258, {w-> 2.10689}}
Out[] =

```



```

Out[] = 6.83794 (* FWHM *)
Out[] = 2.10689 (* resonant detuning value shift *)

```

Appendix II Bi-layer resist process and lift-off process

The detailed condition of sample fabrication process described in Fig. 5.1 is as follows.

- ① Pretreatment of glass-substrate
substrate size: 7-8 mm square
Organic solvent cleaning
1st: Acetone ultrasonic x 5min
2nd: Trichloroethylene@~40degrees C x 5min
3rd: Acetone ultrasonic x 5min
4th: Methanol ultrasonic x 5min
5th: Methanol ultrasonic x 5min
- ② 1st-Spin-Coat; PMMA 950K (thickness ~50 nm)
Spin-Coat condition 1st: 500rpm x 5sec, 2nd: 4000rpm x 60sec
Pre-Bake Hot-Plate: 180degrees C x 2min
10min Cool down
- ③ 2nd-Spin-Coat; ZEP-520 A7 (thickness ~180 nm)
Spin-Coat condition 1st: 500rpm x 5sec, 2nd: 7000rpm x 60sec
Pre-Bake; Hot-Plate: 180degrees C x 2min
10min Cool down
- ④ 3rd-Spin-Coat; Conductive layer (ESPACER 300Z, thickness ~5 nm)
Spin-Coat condition 1st: 500rpm x 5sec, 2nd: 2000rpm x 30sec
Pre-Bake; Hot-Plate: 100degrees C x 2min
10min Cold down
- ⑤ Electron Beam Lithography
Acceleration Voltage; 30kV
Beam current: 40pA
Lithography-Mode; Line-lithography
Dose amount: 250-390 $\mu\text{C}/\text{cm}^2$
- ⑥ Remove conductive layer
Ultrapure water x 1min
- ⑦ Development
ZED-N50 (n- Amylacetate)
R.T. x 40~45sec(strong agitation)
- ⑨ 1st-Rinse (Also etching the PMMA-layer)
ZMD-B (MIBK: 89%, 2-Propanol: 11%); R.T. x 90sec
- ⑩ 2nd-Rinse (Remove ZMD-B, Stop etching of PMMA-layer)
Ultrapure water; R.T. x 1min
- ⑪ Water removal
1st: N₂ -blow
- ⑫ Resistance heating evaporation of Gold
Thickness: 50 nm, evaporation rate: 0.1 nm/sec
- ⑬ Gold Lift-Off process
ZDMAC (n, n-Dimethylacetamide)
1st: 46-47degrees C x 3min-6min(boil)
2nd: 46-47degrees C x 15sec-60sec Ultrasonic; gold lift-off
3rd: 46-47degrees C x 3min-6min(boil); removal of residual resist
4th: Ultrapure water flow x 60sec; removal of organic solvent

Appendix III Sample layout

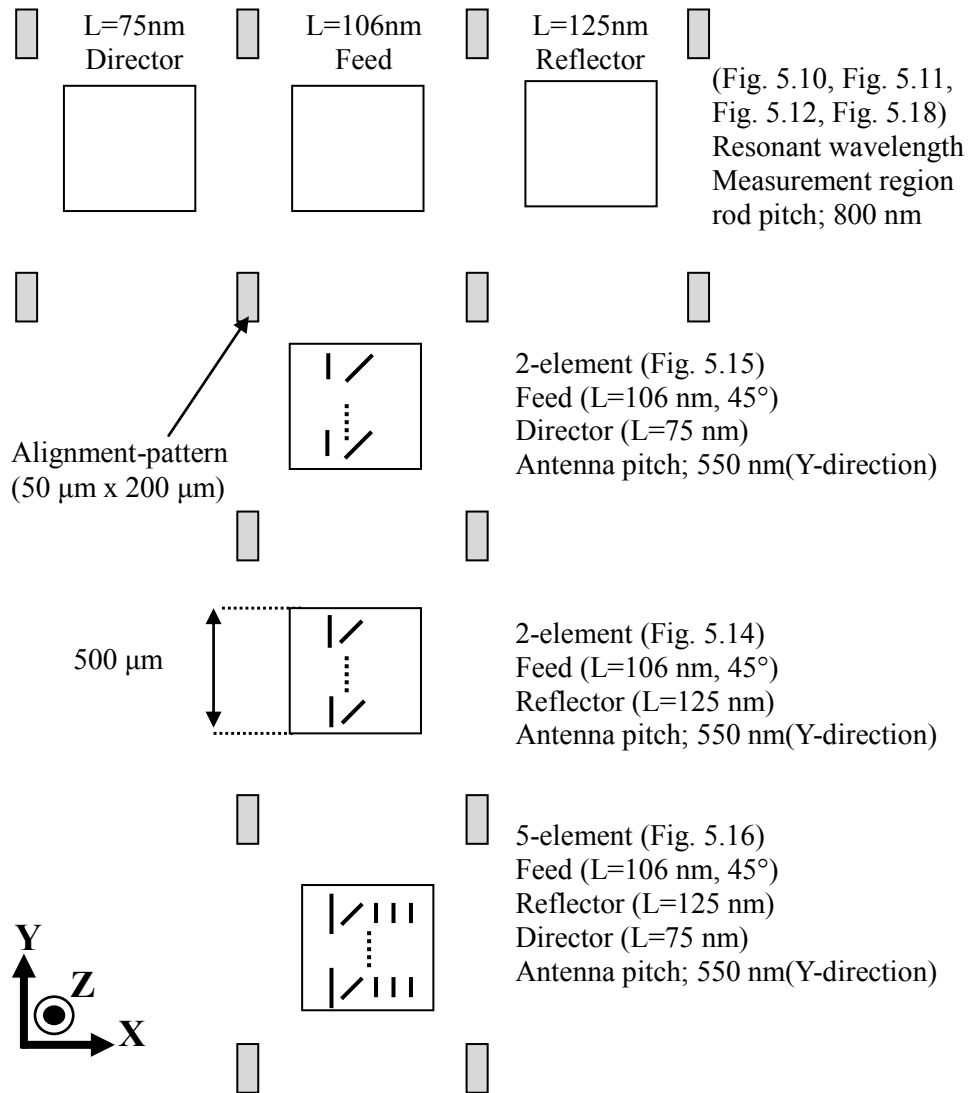


Fig. A: Sample layout of Fig.5.8, Fig.5.9, and Fig. 5.10 (sample No.090501C), fabricated on the same substrate. Six different samples were fabricated on the same substrate. They consisted of resonant wavelength detection sample for Feed, Director, and Reflector, 2-element antenna consisting of Feed and Reflector or Feed and Director, and 5-element antenna shown in Fig. 5.8 and Fig. 5.10. In case of blocking the emission from the antenna, nothing was placed in the X -direction, and the antenna was arrayed only to the Y -direction.

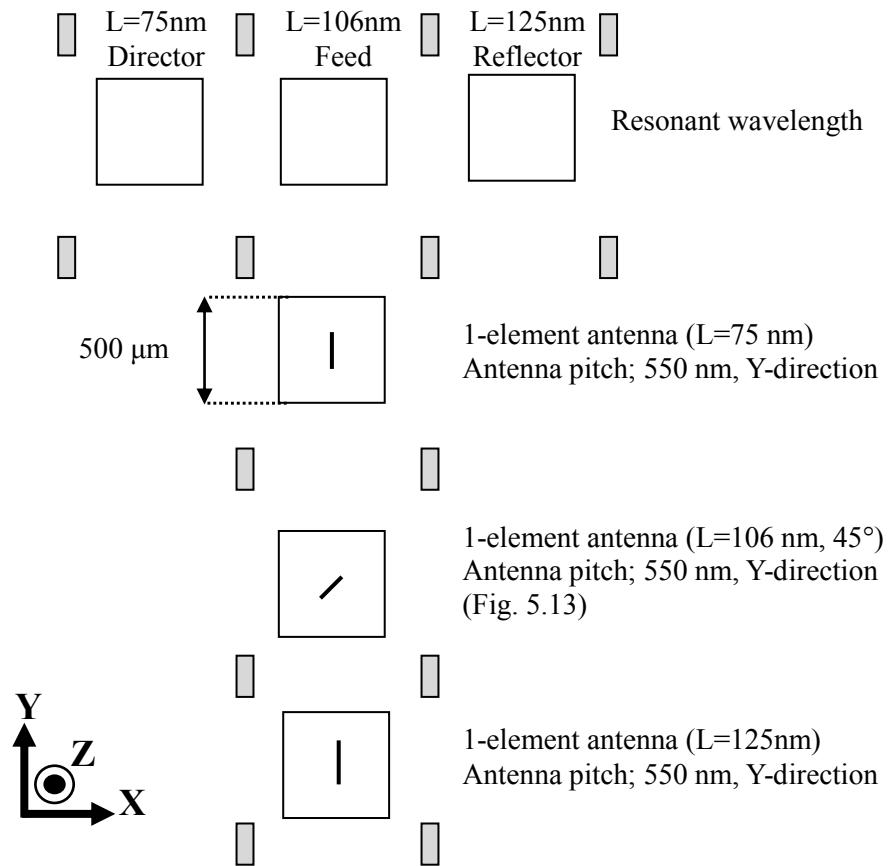


Fig. B: Sample layout of Fig. 5.13 (sample No.090618B), fabricated on the same substrate. Six different samples were fabricated. They consisted of resonant wavelength detection sample for feed, director, and reflector, and 1-element antenna consists of feed, director, and reflector. In the experiment, only the feed antenna was measured.

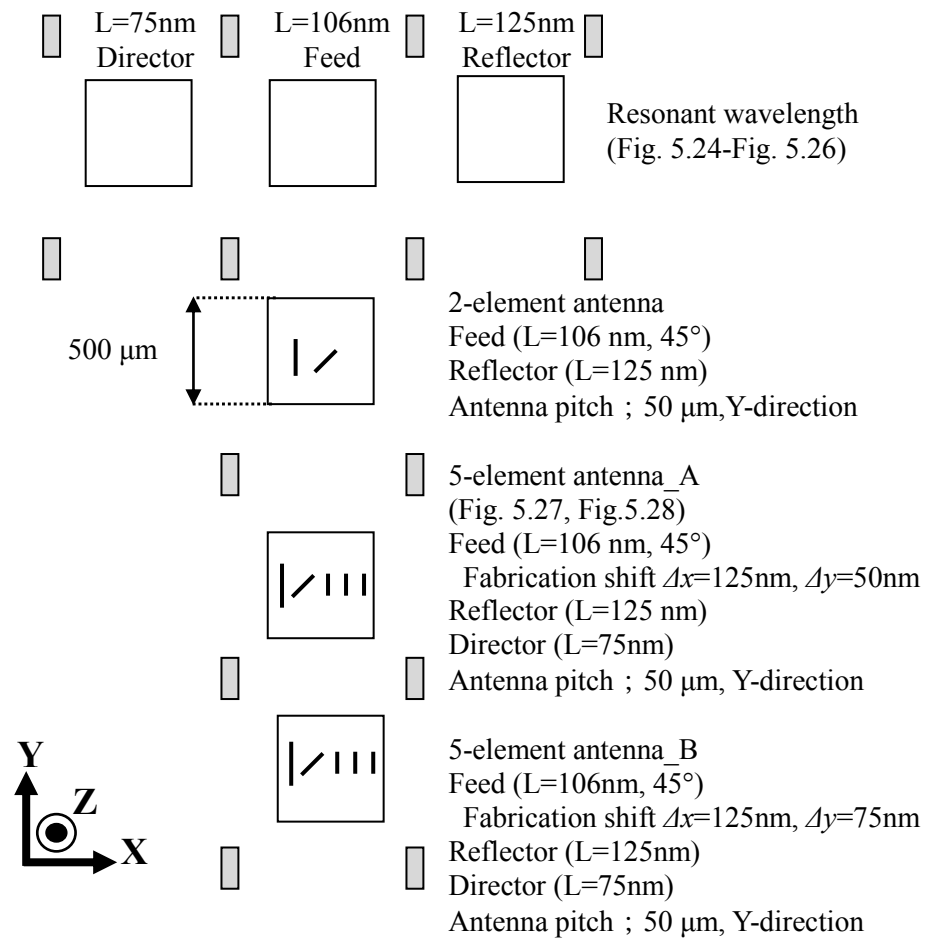


Fig. C: Sample layout of Fig. 5.22, Fig. 5.23, and Fig. 5.24 (sample No.091030C). Six different samples were fabricated on the same substrate. They consisted of resonant wavelength detection sample for feed, director, and reflector. In the measurement of the 5-element antenna shown in the Fig. 5.27, 5-element antenna_A was used.

公表論文

(Published Papers)

- (1) Design parameters for a nano-optical Yagi-Uda antenna.
Holger F Hofmann, Terukazu Kosako and Yutaka Kadoya.
New Journal of Physics, **9**, 217, 1-12 (2007).
- (2) Directional control of light by a nano-optical Yagi-Uda antenna.
Terukazu Kosako, Yutaka Kadoya and Holger F. Hofmann.
Nature Photonics, **4**, 312-315 (2010).